UNIVERSIDADE FEDERAL DO CEARÁ
CENTRO DE CIÊNCIAS
DEPARTAMENTO DE FÍSICA
PROGRAMA DE PÓS-GRADUAÇÃO EM FÍSICA

MAYRA ALEXANDRA PADRÓN GÓMEZ

EXPLORING THE STRUCTURAL AND OPTICAL PROPERTIES OF LOW DIMENSIONAL HALIDE PEROVSKITE-LIKE COMPOUNDS AT EXTREME CONDITIONS

FORTALEZA
2023

MAYRA ALEXANDRA PADRÓN GÓMEZ

EXPLORING THE STRUCTURAL AND OPTICAL PROPERTIES OF LOW DIMENSIONAL HALIDE PEROVSKITE-LIKE COMPOUNDS AT EXTREME CONDITIONS

Tese apresentada ao Programa de Pós-Graduação em Física do Centro de Ciências da Universidade Federal do Ceará, como requisito parcial à obtenção do título de Doutor em Física.

Orientador: Dr. Alejandro Pedro Ayala

FORTALEZA

2023

Dados Internacionais de Catalogação na Publicação
Universidade Federal do Ceará
Sistema de Bibliotecas
Gerada automaticamente pelo módulo Catalog, mediante os dados fornecidos pelo(a) autor(a)

P139e Padrón Gómez, Mayra Alexandra.
Exploring the structural and optical properties of low dimensional halide perovskite-like compounds at extreme conditions / Mayra Alexandra Padrón Gómez. – 2023.
106 f. : il. color.

Tese (doutorado) – Universidade Federal do Ceará, Centro de Ciências, Programa de Pós-Graduação em Física , Fortaleza, 2023.
Orientação: Prof. Dr. Alejandro Pedro Ayala.

1. Low-dimensional perovskite-likes. 2. Extreme conditions. 3. Synchrotron powder x-ray diffraction. 4. Photoluminescence. 5. Raman spectroscopy. I. Título.

CDD 530

MAYRA ALEXANDRA PADRÓN GÓMEZ

EXPLORING THE STRUCTURAL AND OPTICAL PROPERTIES OF LOW DIMENSIONAL HALIDE PEROVSKITE-LIKE COMPOUNDS AT EXTREME CONDITIONS

Tese apresentada ao Programa de Pós-Graduação em Física do Centro de Ciências da Universidade Federal do Ceará, como requisito parcial à obtenção do título de Doutor em Física. Área de concentração: Física da Matéria Condensada.

Aprovada em: 31/07/2023

BANCA EXAMINADORA

_____

Prof. Dr. Alejandro Pedro Ayala
Universidade Federal do Ceará (UFC)

_____

Prof. Dr. Carlos William de Araújo Paschoal
Universidade Federal do Ceará (UFC)

_____

Prof. Dr. Antônio Gomes de Souza Filho
Universidade Federal do Ceará (UFC)

_____

Prof. Dr. Manuel Henrique Lente
Universidade Federal de São Paulo (UNIFESP)

_____

Prof. Dr. Leopoldo Suescun
Universidad de la República Uruguay (UdelaR)

ACKNOWLEDGEMENTS

I am immensely grateful to my supervisor, Alejandro Pedro Ayala, for their guidance, patience, encouragement, expertise, and mentorship throughout this research. Their dedication, constructive feedback, and support have been instrumental in shaping my scientific growth.

To my dear Juan, your solid support, patience, and understanding have been invaluable. Your encouragement and belief in my abilities have inspired me constantly. I am grateful for having you. I love you.

I want to extend my deepest appreciation to my loving family for their unwavering support and encouragement throughout my academic journey.

I would like to express my sincere appreciation to my lovely friends Wendell and Felipe for their grateful support and encouragement. I would also like to extend my deepest gratitude to my research group (LabCrEs) for their collaboration and support.

Lastly, I would like to thank the Universidade Federal do Ceará (UFC) for providing a stimulating academic environment and resources that have contributed to the successful completion of this thesis. This study was financed in part by the Coordenação de Aperfeiçoamento de Pessoal de Nível Superior – Brasil (CAPES) – Finance Code 001.

ABSTRACT

Low-dimensional Metal Halide Perovskite-like (MHPs) compounds have emerged as promising materials for various optoelectronic applications, including photodetectors and solar cells. These compounds feature a metal halide octahedron as the fundamental structural unit, crucial in dictating their optoelectronic and chemical properties. To further investigate and harness their unique potential, researchers have explored extreme conditions, such as low temperatures and high pressures, to induce structural changes and explore their impact on electronic and optical properties uncovering novel physical properties and establishing a comprehensive understanding of the structural-property relationship. One example is the zero-dimensional bromide hexa-Bromo bismuthate $\{[(CH_3)_2NH_2]^+\}_4Br^-.[BiBr_6]^{3-}$, which at low-temperature (T < 100 K) and without involving a structural phase transition, the intriguing octahedra distortion produces a photoluminescence (PL) state changing its optical properties. On the other hand, the two-dimensional $CsPb_2Cl_5$ undergoes two structural phase transitions at high pressures, where the low-pressure phase P_I: *I4/mcm* transforms into phase P_{II}: *I4/m* at P_c^{I-II} = 1.60 GPa, and subsequently changes to phase P_{III}: *C2* at P_c^{II-III} = 5.16 GPa. On the other hand, an occupational disorder was observed in the family of $CsPb_2(Br_{1-x}I_x)_5$, where both Br and I ions occupy the same position at 16l sites. Regarding PL properties, the iodine substitution increases PL intensity and modifies the energy emission, demonstrating a redshift of the PL center. Finally, the low-temperature Raman spectroscopy and PL of the $CsPb_2Br_5$ compound provided valuable insights into the origin of its photoluminescence. The evolution of the photoluminescence spectra at low temperatures reveals an intriguing increase in emission intensity and the emergence of a dual-emission band beyond 60 K. Specifically, the narrow photoluminescence observed at room temperature can be attributed to the radiative recombination of free excitons. In contrast, the broad emission observed at low temperatures is ascribed to the presence of self-trapped excitons (STE). In this context, the results of the structural-property relations in past metal halide perovskite-like pave the way for developing new and improved devices and technologies for different applications.

Keywords: low-dimensional perovskite-likes; extreme conditions; synchrotron powder x-ray diffraction; Raman spectroscopy; photoluminescence.

RESUMO

Compostos de haleto metálico de baixa dimensão semelhantes a perovskita (MHPs) surgiram como materiais promissores para várias aplicações optoeletrônicas, incluindo fotodetectores e células solares. Esses compostos apresentam um octaedro de haleto metálico como unidade estrutural fundamental, crucial para ditar suas propriedades optoeletrônicas e químicas. Para investigar e aproveitar melhor o seu potencial único, os investigadores exploraram condições extremas, como baixas temperaturas e altas pressões, para induzir mudanças estruturais e explorar o seu impacto nas propriedades electrónicas e ópticas, descobrindo novas propriedades físicas e estabelecendo uma compreensão abrangente da relação propriedade-estrutura. Um exemplo é o brometo hexa-Bromo bismutato de dimensão zero $\{[(CH_3)_2NH_2]^+\}_4Br^-.[BiBr_6]^{3-}$, que em baixa temperatura (T <100 K) e sem envolver uma transição de fase estrutural, a intrigante distorção de octaedros produz um estado de fotoluminescência (PL) alterando suas propriedades ópticas. Por outro lado, o composto bidimensional $CsPb_2Cl_5$ sofre duas transições de fase estruturais em altas pressões, onde a fase de baixa pressão P_I: *I4/mcm* se transforma na fase P_{II}: *I4/m* em P_c^{I-II} = 1.60 GPa, e posteriormente muda para fase P_{III}: *C2* em P_c^{II-III} = 5.16 GPa. Por outro lado, foi observado um distúrbio ocupacional na família de $CsPb_2(Br_{1-x}I_x)_5$, onde ambos os íons Br e I ocupam a mesma posição nos sítios 16l. Em relação às propriedades do PL, a substituição de iodo aumenta a intensidade do PL e modifica a emissão de energia, demonstrando um desvio para o vermelho do centro do PL. Finalmente, a espectroscopia Raman de baixa temperatura e PL do composto $CsPb_2Br_5$ forneceram informações valiosas sobre a origem da sua fotoluminescência. A evolução dos espectros de fotoluminescência a baixas temperaturas revela um aumento intrigante na intensidade de emissão e o surgimento de uma banda de dupla emissão além de 60 K. Especificamente, a estreita fotoluminescência observada à temperatura ambiente pode ser atribuída à recombinação radiativa de excitons livres. Em contraste, a ampla emissão observada em baixas temperaturas é atribuída à presença de excitons auto-aprisionados (STE). Neste contexto, os resultados das relações propriedade- estrutura no passado do tipo perovskita de haleto metálico abrem caminho para o desenvolvimento de dispositivos e tecnologias novos e melhorados para diferentes aplicações.

Palavras-chave: perovskitas de baixa dimensionalidade; condições extremas; difração de raios x em pó de sincrotron; espectroscopia Raman; fotoluminescência.

LIST OF FIGURES

LIST OF TABLES

CONTENTS

1 Introduction

Metal halide perovskites (MHPs) have emerged as a captivating and versatile material class that has garnered significant attention across various scientific disciplines, including physics, chemistry, and materials science. These compounds boast an unique crystal structure, which underpins their exceptional properties and diverse applications as solar cells, where the rapid progress in perovskite solar cells has led to impressive power conversion efficiencies and has positioned them as a potential rival to traditional silicon solar cells, (Meng, You e Yang, 2018; Rong *et al.*, 2018), photodetectors, photo-batteries, and Light Emitting Diodes (LEDs) (Liu *et al.*, 2021; Stranks e Snaith, 2015; Zhang, Eperon e Snaith, 2016).

The perovskite crystal structure is characterized by a corner-sharing BX_6 octahedron, where A elements occupy the cuboctahedral cavity in each unit cell. The most prevalent chemical formula for MHPs is ABX_3, wherein X represents halide anions, while A and B encompass various sizes of cations. Specifically, A^+ denotes an organic molecule or inorganic cation, while B^{2+} corresponds to a metal cation (Wu *et al.*, 2022) (see Figure 1). Deviations from the ABX_3 stoichiometry can be attained through total or partial substitution of chemical elements in their respective A, B, or X positions (Jin, 2021). Such substitutions can effectively modify the crystal structure and engender new properties, paving the way for establishing crucial structure-property relationships in these compounds. This topic is of immense interest within the research community, as it catalyzes the development of novel and advanced materials for diverse technological applications (Zhu e Zhu, 2020).

MHPs can be characterized by their archetypal ABX_3 system, featuring accessible cubic, tetragonal, orthorhombic, trigonal, and monoclinic polymorphs (Akkerman e Manna, 2020; Alaei *et al.*, 2021). These materials also undergo structural phase transitions (SPT) as a function of temperature and pressure. Metal halide perovskites are solution-processable, making them easily preparable from precursor solutions containing raw materials AX and BX_2 halide salts, such as chloride (Cl), bromide (Br), and iodide (I), which crystallize into the ABX_3 structure. These compounds can exist in fully inorganic and hybrid organic-inorganic structures (Xiao, Song e Yan, 2019; Zhou *et al.*, 2019). Modifying the corner-sharing octahedral network [BX_6] in the MHPs crystal lattice, could described different dimensionalities such as 2D, 1D, and 0D, each corresponding to distinct arrangements of components. There are two categories of low

dimensionalities *"morphological level,"* corresponding to the arrangement of a few or hundreds of unit cells in 2D, 1D, or 0D (left panel of Figure 2), and *"molecular level,"* corresponding to the arrangement of octahedrons in 2D, 1D, or 0D (right panel of Figure 2).

Figure 1– Unit cell of an ideal cubic perovskite ABX_3 (left) and their extended crystal line structured connected by corner-sharing $[BX_6]^{4-}$ octahedra (right) (Zhou e Huang, 2018).

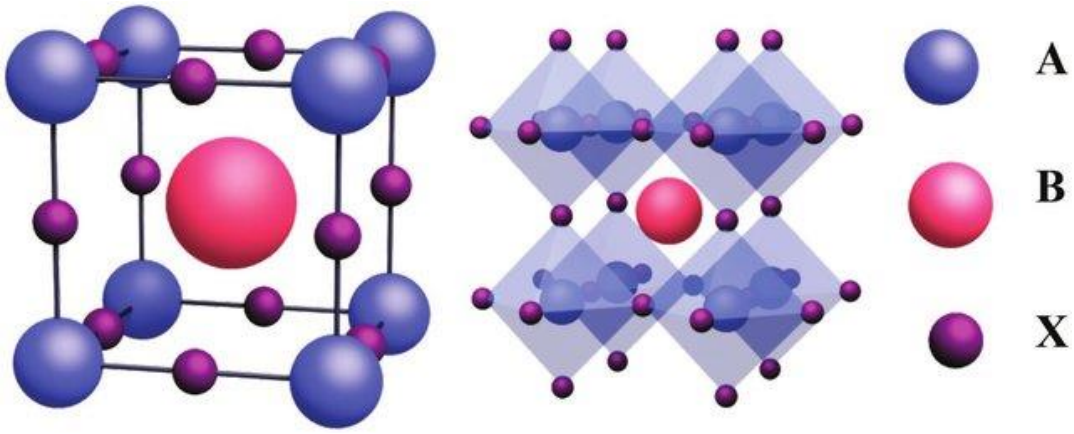

Source: (Zhou *et al., 2018)* without adaptations.

The diversity of metal halide perovskite structures, especially in their low-dimensional forms, has led to intriguing properties and potential applications (Kim *et al.*, 2018; Zhang, Eperon, e Snaith, 2016). Low-dimensional perovskite structures have gained significant attention due to their unique electronic and optoelectronic properties and enhanced stability compared to their three-dimensional counterparts. These materials exhibit quantum confinement effects, which result in tunable bandgaps and improved charge transport properties. Moreover, low-dimensional perovskites are promising for quantum computing and other emerging technologies (Qin e Pan, 2023). The morphological low-dimensional aspects of perovskites are closely associated with their crystal size. These low-dimensional metal halide perovskites (L-MHPs) are considered nanomaterials, exhibiting quantum confinement effects in at least one direction. They can be categorized into three main groups: 2D nanoplatelets (NPLs), 1D nanowires (NWs) and nanorods, and 0D quantum dots (QDs) (Yao *et al.*, 2021). Despite their reduced dimensions, these L-MHPs maintain a crystallographic structure identical to 3D MHPs, with ABX_3 being the prevailing chemical formula (Lin *et al.*, 2018). Their

distinctive properties stem from the quantum confinement effect arising due to the reduced dimensions.

Figure 2– 3D ABX_3 MHPs and their perovskite-related materials with different dimensionalities at both morphological and molecular levels. On both the morphological (left) and molecular (right) levels, it shows a reduction in dimensions from bulk phase to 2D, 1D, and 0D to obtain new materials related to ABX_3 MHPs (Wu et al., 2022).

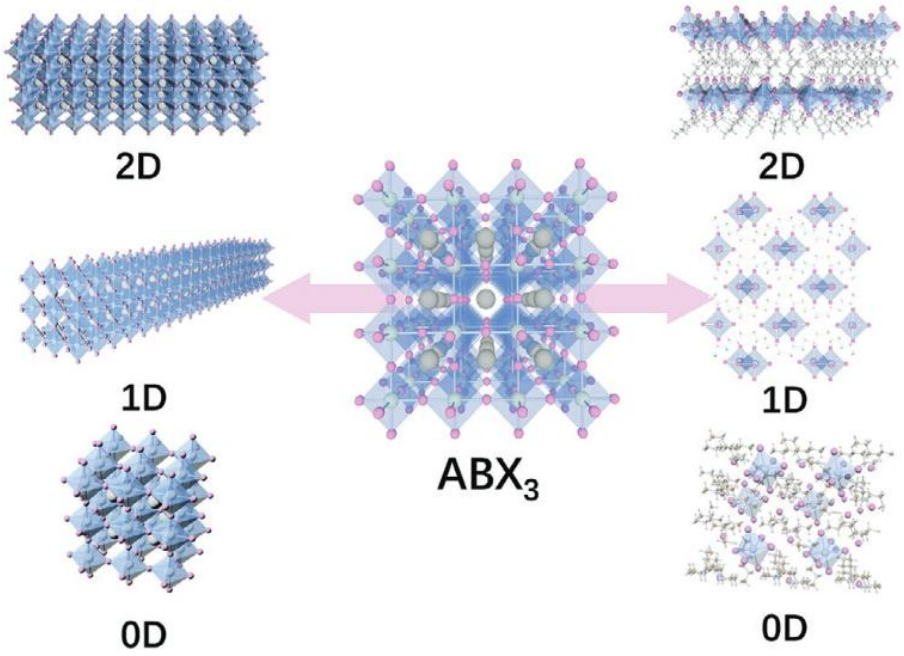

Source: (Wu *et al., 2022)* without adaptations.

Investigating low-dimensional metal halide perovskites is a rapidly evolving field with significant implications for materials science and technology. Researchers are actively exploring various synthetic approaches to precisely control the size and shape of these nanomaterials, aiming to unlock their full potential for next-generation devices. However, challenges persist, particularly concerning stability and reproducibility. Understanding these fundamental aspects sheds light on the physics underlying L-MHPs, and enables the development of tailored strategies to enhance their performance and stability in optoelectronic devices (Nie *et al.*, 2023). While the number of natural perovskite minerals is limited, the realm of synthetic compounds spans across the entire periodic table, leading to modification of the chemical formulas and diverse perovskite types, including metallics, metal-free, and oxides,

highlighting the adaptable nature of the perovskite crystal lattice. Moreover, their advantages, such as low cost, facile low-temperature synthesis, and solution processability, have contributed to their growing popularity (Drushliak e Szafrański, 2022).

Crystal structure (MHPs), HPLs exhibit significant polymorphism, with diverse structural phase transitions highly sensitive to changes in temperature and pressure. These structural phase transitions significantly impact the electronic and optical properties of HPLs (Burger *et al.*, 2021; Octavio de Araujo *et al.*, 2022). Notably, modifications in lattice parameters, phonon frequencies, and electron-phonon coupling strengths observed during the phase transitions can be harnessed to design new functional materials for optoelectronic devices, flexible electronics, and smart windows. However, this dynamic behavior poses challenges in understanding the intricate structure-property relationships, impeding a clear path toward commercialization due to inherent phase instability. Therefore, a deeper understanding of the underlying mechanisms and anion exchange in MHPs is essential to gain a clearer perspective. Exploring and controlling polymorphism and structural phase transitions in perovskites are necessary steps to ensure the reliable performance of these compounds and to design and engineer new materials with desired properties for specific applications (Kim *et al.*, 2022; Tang *et al.*, 2022).

MHPs and HPLs, as previously described, are systems where structural and compositional modifications impact the physical properties present in the samples (Gao et al., 2019; Yan et al., 2023). Further investigation of the underlying mechanism and anion exchange is crucial to elucidate the correlation between crystal structure and physical property. Notably, two mechanisms control the perovskite phase and composition, which are highly relevant to properties, these mechanisms are the octahedral tilting and anion exchange (Shi *et al.*, 2017). Synchrotron-based and conventional X-ray diffraction measurements shed light on the physical aspects of modifying the octahedral displacements related to perovskites and like-perovskite compounds. Differential optical methods reveal the anion exchange processes, and both analyses are developed in situ, providing a quantitative characterization of the tunable properties. These represent the initial steps in the comprehensive characterization of perovskites and like-perovskites. Figure 3 illustrates the structural diversity of perovskites derived from the potential for dynamic octahedra tilt within a corner-sharing network of the ABX_3 form (Ahn *et al.*, 2017; Chan *et al.*, 2022; Steele *et al.*, 2020; Tu *et al.*, 2018).

Octahedral tilting is pivotal in the structural variation and destabilization of the cubic ABX_3 phase in perovskites. As depicted in Figure 3B, the proper octahedral tilting prevents the collapse of the corner-sharing network during temperature variations. As previously discussed, when the tolerance factor shifts away from the ideal range, the energy required for bond bending becomes sufficient to break them, leading to the formation of perovskites, perovskite-like or non-perovskite structures, such as side- or face-sharing octahedra (Grancini e Nazeeruddin, 2018). Restructuring the cubic phase into a lower symmetry subgroup is fundamental in halide perovskites and like-perovskite compounds.

Figure 3C presents an overview of the most common 15 different space groups of tilted perovskites, as predicted by the group-subgroup theory. The Glazer notation is used to classify octahedral distortion throughout the crystal during thermal expansion or decrease (Howard e Stokes, 1998). For instance, the $CaTiO_3$ perovskite exhibits the phase sequence upon heating as $Pnma \rightarrow I4/mcm \rightarrow Pm\bar{3}m$ above 1000 °C (Yashima e Ali, 2009). On the other hand, the anion exchange can be achieved by partially or completely substituting halide ions. The flexible lattice and abundance of vacancies enable switching during or post-synthesis with an abundant source of halide precursors or a mixture of other anion species (see Figure 3A). The halide concentration drives the diffusion of ions into the crystal lattice, and as a result, bandgaps are dominantly dependent on the anion composition and valence. This phenomenon leads to diverse relations between structural, physical, and optical properties. Additionally, anion exchange can modify or shift the photoluminescence (PL) emission across the visible spectrum (Bella *et al.*, 2016; Protesescu *et al.*, 2015). The anion exchange has demonstrated its versatility in modifying the structures and properties of MHPs and HPLs (Schmidt-Mende *et al.*, 2021).

Figure 3– Phase transitions, anion exchange, and the phase-energy landscape in polymorphic ABX_3 perovskites. **A** Archetypal cubic crystal structure ($t = 1$) and anion exchange concept for ABX_3 perovskites. When t deviates from unity, octahedral tilts are introduced to accommodate a pseudo-cubic distorted perovskite structure. **B** Illustration of reversible phase transitions in polymorphic perovskites, transitioning through pseudo cubic structures via octahedral tilting and into a non-perovskite structure via bond breaking. **C** Overview of reported group-subgroup symmetries of tilted halide perovskites $APbX_3$ (A=MA, FA, Cs; X= Cl, Br, I), and $CsSnX_3$ (X=Cl, Br, I) with comparison to the archetypal $CaTiO_3$ perovskite system. The

tilts are identified using Glazer notation, and the dashed lines correspond to first-order transitions. Other subgroups have been reported under atypical environments and are not included for simplicity (Steele et al., 2020).

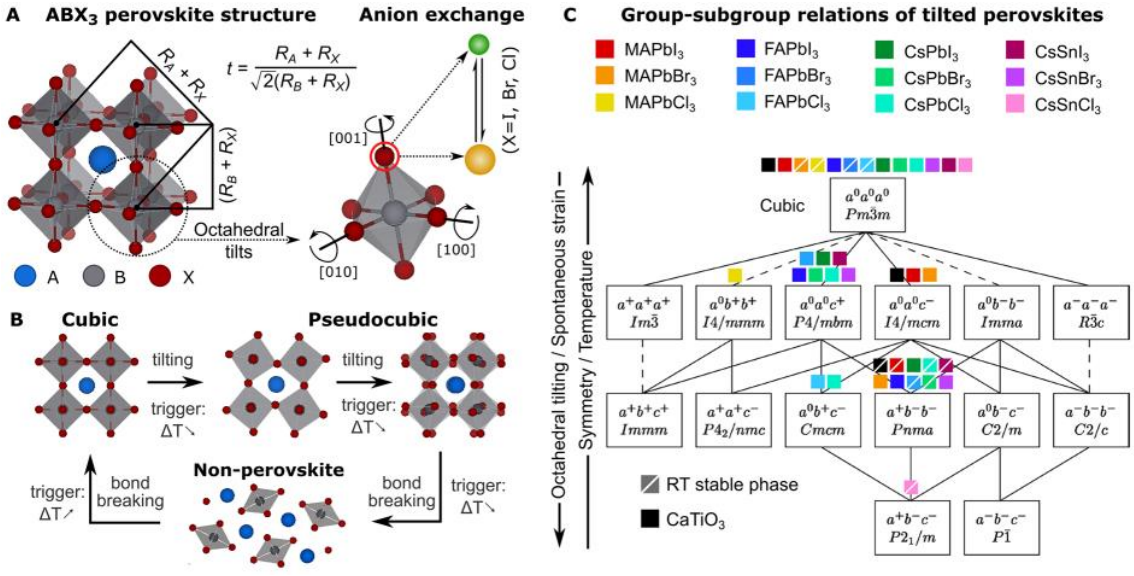

Source: (Steele *et al.*, 2020) without adaptations.

Due to their distinctive characteristics, L-MHPs and L-HPLs compounds could display self-trapped exciton (STE) emissions. The A-site cation plays a crucial role in determining the structural stability and the strength of electron-phonon interactions, ultimately impacting the formation and behavior of self-trapped excitons. Achieving the right balance between the structural tolerance factor and the electron-phonon coupling is crucial for maximizing the STE emission efficiency in these materials (Liu *et al.*, 2023). The broadband emission observed in low-dimensional perovskites and perovskites-like has sparked an intriguing scientific debate surrounding the role of structural defects and phonons in the recombination process. This debate revolves around how these factors directly contribute as emissive centers or indirectly facilitate the formation of self-trapped excitons (STEs) (Lin *et al.*, 2022). However, designing an ideal A-site cation that satisfies the structural tolerance while promoting the desired STE emission, driven by the appropriate electron-phonon coupling effect, presents a significant challenge (Xu *et al.*, 2022).

The interaction between charge carriers and lattice vibrations, known as electron-phonon coupling, plays a crucial role in the optoelectronic properties of perovskites. These

materials exhibit strong excitonic effects, enhancing the coupling between electrons or holes and lattice vibration. In particular, the formation of self-trapped excitons (STEs) arises from the strong electron-lattice or hole-lattice coupling, leading to the confinement of bound electron-hole pairs within the lattice distortion field; it is highly related to distortions in the octahedron unit or octahedral tilting (Grancini e Nazeeruddin, 2018). In the simplified exciton self-trapping mechanism (Figure 4), the strong electron-phonon coupling induces a lattice distortion, creating a potential energy landscape that traps the exciton. This trapping phenomenon results in the localization of the electron and hole, forming a self-trapped exciton state (Yan et al., 2023).

Figure 4 – Scheme showing the mechanism of exciton self-trapping in a 2D perovskite. The vertical arrows represent optical transitions (Grancini e Nazeeruddin, 2018).

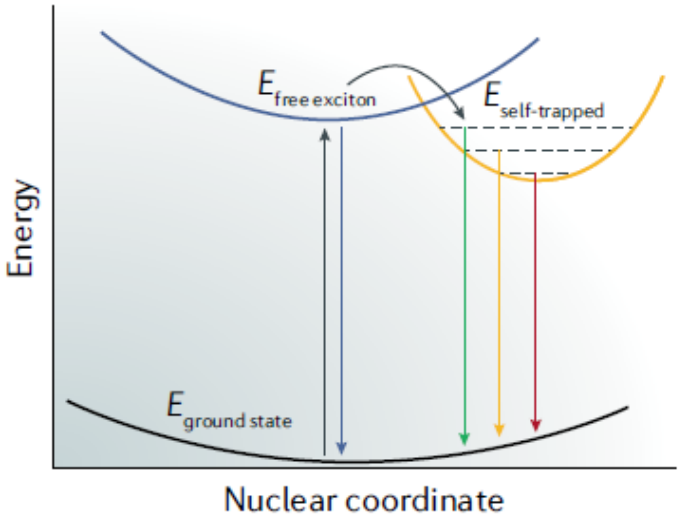

Source: (Grancini et al., 2018) without adaptations.

Photoluminescence is a fundamental phenomenon that greatly influences the optical properties of semiconductors. Among the different types of luminescence, exciton luminescence is particularly significant as it describes the photon-emitting process resulting from the recombination of an exciton. Excitons, formed by an electron and a hole binding, are responsible for the characteristic emission properties observed in semiconductors. In conventional semiconductors, the emission of exciton luminescence is primarily determined by the stationary bandgap and the exciton-binding energy, resulting in narrowband photoluminescence. This narrow emission spectrum has been extensively utilized in various

applications, particularly in optical communication, where the precise generation and detection of photons are crucial (Li *et al.*, 2019).

Significant changes by extreme conditions, such as low-temperature and high pressure on low-dimensional halide perovskite-like materials, enable the formation, modification, or production of phase-change optical devices. Allowing a deep insight into the current investigations on L-HPLs, and the experimental demonstrations open a pathway towards their discovery and understanding. This inspires the potential applications of perovskites-like in different devices, as the paradigm of crystal structure defining properties remains open, and it is the principal objective of this work in different family compounds. In this context, this thesis is structured as follows: Chapter 2 describes the methodology used for sample preparation and characterization techniques. Chapter 3 investigates the low-temperature effect on the zero-dimensional hybrid perovskite-like $[(CH_3)_2NH_2]_4BiBr_7$. Chapter 4 presents the pressure-induced structural phase transition on the 2D structure $CsPb_2Cl_5$. Chapter 5 investigates iodide doping and its impact on 2D $CsPb_2X_5$ (X = Br, I) perovskite-like properties. Chapter 6 explored the electron-phonon coupling in the 2D $CsPb_2Br_5$. Finally, it presents the conclusions and potential applications of these materials in future research.

2 Experimental Section

This chapter provides a comprehensive overview of the experimental methods employed in this study. The methodology includes the synthesis of a diverse range of compound families using a variety of techniques. Furthermore, the investigation explores the fundamental principles underlying the influence of low-temperature and high-pressure conditions on various analytical methods. Specifically, the effects of these conditions on Single Crystal X-Ray Diffraction (SCXRD), Synchrotron Powder X-Ray Diffraction (SPXRD), photoluminescence (PL), and Raman spectroscopy were thoroughly examined and analyzed.

2.1. Synthesis Method

All samples were synthesized by the slow evaporation method. The reagents used in synthesizing were from commercial sources purchased from Sigma Aldrich and Alfa Aesar.

$((CH_3)_2NH_2)_4BiBr_7$: The compound was grown by dissolving 1 mmol of $BiBr_3$ in N, N-dimethylformamide (DMF), adding an aqueous solution of HBr at 60 ºC. The resulting solution was stirred and then kept at room temperature. After 4 weeks, gradual evaporation of the solution led to the growth of high-quality, single-transparency crystals exhibiting a bright-yellow coloration in the form of bars.

$CsPb_2Cl_5$: The raw materials were cesium chloride (CsCl, 99.9 %), lead chloride ($PbCl_2$, 99.9 %), and HCl solution (47 wt % in H2O). The precursors CsCl/$PbCl_2$ were added in a small beaker in a 1:2 stoichiometric ratio. Then, 4 ml of deionized water and 2 ml of HCl were mixed at 80 ºC into the beaker under constant stirring at 480 rpm until a clear solution was obtained. The same temperature was maintained for 30 minutes. The resulting solution was placed to evaporate at 24 ºC, covered with parafilm containing tiny holes. The final crystals were washed with toluene several times.

$CsPb_2(Br_{1-x}I_x)_5$: Light-yellow square single crystals of iodine-substituted $CsPb_2Br_5$ were synthesized using Cesium bromide (CsBr, 99.9%) and lead bromide ($PbBr_2$, 99.9%) in a stoichiometric ratio, and mixed with 2 ml of N, N-dimethylformamide (DMF) at 80°C while being constantly stirred at 480 rpm until a clear solution was obtained. Cesium iodate (CsI, 99.9%) and $PbBr_2$ were used in the proper ratio and mixed for substitution. HBr solution (47 wt. % in H_2O) was added, and the temperature was maintained for 1 hour. The solution was

then evaporated at room temperature for several days, covered with paraffin film with tiny holes, and crystals were collected from the bottom of the beaker and washed with toluene.

2.3. Experimental measurements

Single crystal X-ray diffraction (SCXRD) measurements

Single crystal X-ray diffraction data (ϕ scans and ω scans with κ and θ offsets) were collected on a Bruker D8 Venture κ-geometry diffractometer equipped with a Photon II CPAD detector and an IμS 3.0 Incoatec Mo Kα (λ = 0.71073 Å) microfocus source. Suitable crystals from each sample were harvested and mounted on MiTeGen MicroMount using immersion oil. The APEX 4 software was used for the unit cell determination and data collection. The data reduction and global cell refinement were made using the Bruker SAINT+ software package, and a multi-scan absorption correction was performed with SADABS (Krause *et al.*, 2015). Using the Olex^2 (Dolomanov *et al.*, 2009) interface program to the SHELX suite (Sheldrick, 2008), the structure was solved by the intrinsic phasing method implemented in ShelXT (Sheldrick, 2015), allowing the location of most of the atoms. The remaining atoms were located from different Fourier maps calculated from successive full-matrix least-squares refinement cycles on F^2 with ShelXL and refined using anisotropic displacement parameters. MERCURY (Macrae *et al.*, 2020) and VESTA (Momma e Izumi, 2011) were used to prepare the artwork representations for publication.

Synchrotron Powder X-Ray Diffraction (SPXRD): SPXRD was performed at the XDS beamline of the Brazilian Synchrotron Laboratory (LNLS). High-pressure patterns were obtained with a wavelength of λ = 0.6199 Å. A sp2300 spectrometer from Princeton Instruments equipped with a 1200 gr/mm grating and an LN2- cooled CCD was used to record the measurements excited by a 405 nm solid-state laser. The sample and a small ruby chip were loaded in a diamond anvil cell (DAC) using Nujol (Mineral oil) as the pressure-transmitting medium. The pressure values were calibrated using the standard ruby luminescence lines.

Raman spectroscopy*:* The low-temperature Raman active dependence spectra, from 10 K until room temperature, were collected using a T64000 Jobin–Yvon spectrometer equipped with an Olympus microscope and an LN_2-cooled CCD to detect the scattered light. The spectra were

excited with an Argon ion laser ($\lambda = 514.5$ nm). The spectrometer slits were set to give a spectral resolution better than 2 cm^{-1}. All measurements were performed using a long working distance plan-achromatic objective (20.00×0.35×20.50 mm). The temperature-dependent spectra were obtained by keeping the sample in a vacuum inside a He-compressed closed-cycle cryostat. A Lakeshore 330 controller controlled the temperature, keeping the precision around 1 K.

The pressure-dependent spectra were obtained by keeping the powder sample in a diamond anvil cell chamber with stainless steel gaskets with holes of about 200 μm. Nujol was used as a pressure-transmitting pressure medium. The ruby pressure gauge method was used to quantify the relationship between the applied pressure (Shen *et al.*, 2020) and line emission. The powder of the sample and ruby were together in the gaskets without contact. Each Raman spectrum was deconvoluted in the sum of Lorentzian functions, using the Fityk software (Wojdyr, 2010).

Photoluminescence (PL): The PL spectra were collected using a T64000 Jobin–Yvon spectrometer equipped with an Olympus microscope and an LN_2-cooled CCD to detect the scattered light. The spectra were excited with an external lamp (405 nm) using a long working distance plan-achromatic objective of 20X. The temperature-dependent spectra were obtained by keeping the sample in a vacuum inside a He- compressed closed-cycle cryostat for PL analyses. A Lakeshore 330 controller controlled the temperature, keeping the precision around 1 K. The photoluminescent curves were adjusted with a Person fit profile using Fityk following the quantitative analysis of emission spectra.

Scanning Electron Microscopy (SEM): The analyses were performed using a Scanning Electron Microscope (SEM) QUANTA FEG 450 available at the Central Analítica of the Universidade Federal do Ceará (UFC).

3 Understanding the low-temperature effect on the zero-dimensional perovskite-like $[(CH_3)_2NH_2]_4BiBr_7$

In recent years, Lead Halide Perovskites (LHPs), including inorganic and hybrid variants, have emerged as groundbreaking semiconductors with diverse applications. However, concerns over the long-term stability and toxicity of lead (Pb) have spurred interest in exploring alternative lead-free perovskite materials (Wang *et al.*, 2019). Efforts to develop lead-free perovskites have focused on replacing Pb^{2+} ions with environmentally friendly metal cations, including Sn^{2+}, Bi^{3+}, Cu^{2+}, Sb^{3+}, and Ge^{2+} (Cao e Li, 2021; Zhao *et al.*, 2019) to mitigate environmental and health risks while maintaining or improving performance. These alternative cations offer reduced toxicity, enhanced stability, and tunable properties, making them promising candidates for next-generation optoelectronic devices (Chatterjee e Pal, 2018; Ke e Kanatzidis, 2019).

The search for suitable lead-free perovskite materials presents exciting opportunities and challenges. These alternative cations offer tunability and unique properties that have the potential to revolutionize optoelectronics. By systematically investigating the structural, electronic, and optical characteristics of these materials, researchers aim to unlock their full potential for a wide range of applications (Luo *et al.*, 2018). Extensive research has been dedicated to understanding the fundamental properties, optimizing synthesis methods, and exploring device applications of lead-free perovskite materials. Bi-based alternatives have garnered attention due to their non-toxic nature and high chemical stability, making them suitable for various applications, including organic synthesis and medicine. Researchers are actively exploring the unique properties of Bi-based halide perovskites and novel strategies to optimize their performance, paving the way for their potential use in diverse applications (Shen *et al.*, 2020; Zhang, Wang, e Zou, 2019).

Understanding the performance and characteristics of Bi-based halide perovskites will be crucial for their successful integration into various optoelectronic devices (Wu *et al.*, 2023). The field actively explores their applications and develops novel approaches to optimize their performance, offering promising prospects for future advancements. Among the extensively investigated Bi-based compounds are the zero-dimensional $A_3Bi_2I_9$ materials, where A represents Cs, Rb, and the organic molecule CH_3NH_3. These compounds have shown promise as high-performance metal halide perovskite photocatalysts for solar energy conversion (Li *et*

al., 2022; Park *et al.*, 2015; Zhang *et al.*, 2018) and as potential candidates for X-ray detectors due to their eco-friendly composition and high attenuation coefficient to X-ray irradiation (Lin *et al.*, 2023). Three-dimensional double perovskites, such as Cs_2AgBiX_6 (X= Cl, Br), have been investigated for their optoelectronic and photocatalytic applications. Moreover, Bi perovskites have been systematically studied for photocatalytic CO_2 reduction, making them highly attractive for sustainable energy conversion applications (McClure *et al.*, 2016; Tedesco e Malavasi, 2023; Wu *et al.*, 2021).

Despite the extensive investigations on Bi-based samples for perovskite, and perovskite-like formation, the presence of Bi^{3+} ions possess a significant challenge, and the complete substitution of Pb with Bi has not yet been achieved, resulting in limited hybrid compositions. Therefore, this study is focused on the novel organic-inorganic material known as Tetrakis (dimethylammonium) Bromide Hexabromobismuthate: $\{[(CH_3)_2NH_2]^+\}_4Br^-.[BiBr_6]^{3-}$ (Samet *et al.*, 2010) or its abbreviated form DMA= $[(CH_3)_2NH_2]^+$ (DMA_4BiBr_7). This compound has been systematically examined to analyze the structural-property changes under low-temperature conditions comprehensively. Several characterization techniques, including Single Crystal X-Ray Diffraction (SCXRD), Raman spectroscopy, and Photoluminescence (PL), have been employed to understand and characterize the properties of this compound.

3.1 Investigating the Crystal Structural Modification

The crystal structure of $[(CH_3)_2NH_2]_4BiBr_7$ at room temperature was accurately confirmed using the Single-Crystal X-Ray Diffraction (SCXRD) technique. The compound exhibits an orthorhombic perovskite-like structure with $P2_12_12$ space group. The unit cell dimensions of a = 10.8150(3) Å, b = 13.8872(3) Å, c = 8.9272(3) Å, and V = 1340.78(7) $Å^3$ (see Figure 5a). The asymmetric unit consists of various elements, which can be described by the chemical formula $\{[(CH_3)_2NH_2]^+\}_4Br^-.[BiBr_6]^{3-}$. Within the crystal structure, two crystallographic independent positions are occupied by $[(CH_3)_2NH_2]^+$ molecules. One of these molecules is linked to an isolated Br^- anion through hydrogen bonds, both found in disordering sites. Meanwhile, the other $[(CH_3)_2NH_2]^+$, along with the octahedral $[BiBr_6]^{3-}$ units, occupy the void spaces within the crystal structure.

The compound $[(CH_3)_2NH_2]_4BiBr_7$ exhibits intriguing behavior at low temperatures, remarkably avoiding any structural phase transition. However, at this temperature, all

dimethylammonium (DMA) cations assume well-defined positions and orientations (see Figure 5b), influencing the structural framework through an order-disorder mechanism that leads to the contribution of intermolecular hydrogen bonds (*H*-bonds) between the $DMA^{+} \cdots Br^{-}$ and the $DMA^{+} \cdots [BiBr_6]^{3-}$ units, in the crystal stability. The *H*-bonds at low temperatures involve a smaller energy change due to their partial interactions, and the octahedrons large and well-defined geometric arrangement could overlap with the electronic *H*-bonds. Comparing these two types of interactions, *H*-bonds are more flexible and sensitive to environmental changes, such as temperature variations, while octahedral interactions are relatively more robust, providing the structural stability of the crystal lattice. This observation suggests that the low-temperature conditions induce unique dynamic interactions within the crystal lattice, leading to the establishment of *H*-bonds that significantly influence the material properties.

Figure 5 – Crystal structure of the $[(CH_3)_2NH_2]_4BiBr_7$ at (a) room temperature and (b) low-temperatures. The black dashed line is presented as the H- bonds or the connection between $[(CH_3)_2NH_2]^{+} \cdots Br^{-}$ and the $[(CH_3)_2NH_2]^{+} \cdots [BiBr_6]^{3-}$.

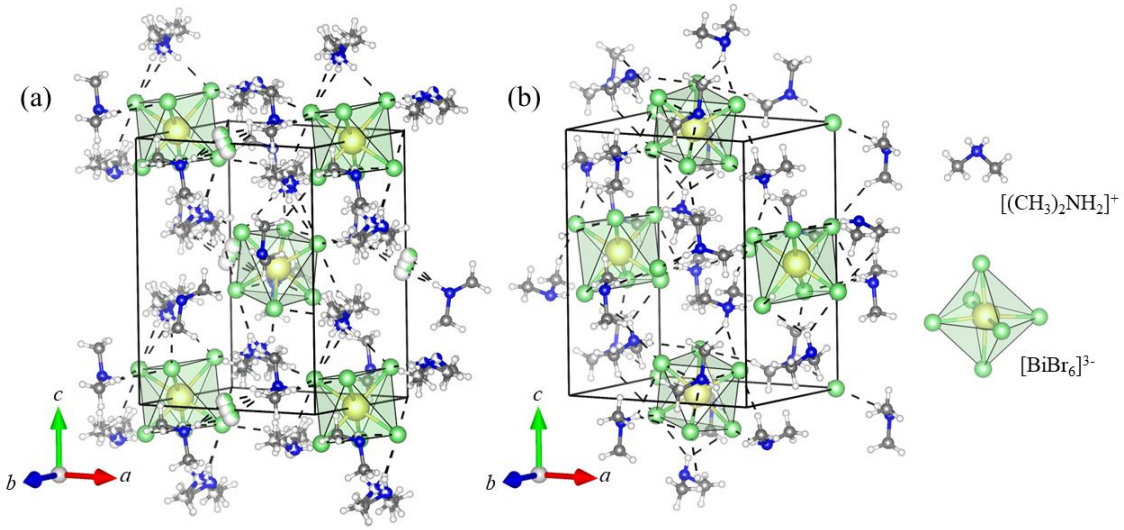

Source: Elaborated by the author.

Concurrently, a natural decrease in the cell parameters is observed at 100 K, indicating a contraction of the crystal lattice as the temperature decreases. This lattice contraction could be attributed to the reorganization of the molecular components. To gain deeper insights into these structural changes, comprehensive crystallographic data and structure refinement results for the sample at both room temperature and 100 K are provided in Table 1, offering detailed information about the variations in the structural parameters.

Table 1– Crystal data and refinement parameters of $[(CH_3)_2NH_2]_4BiBr_7$ at different temperature conditions.

Empirical formula	$(DMA)_4BiBr_7$	
Formula weight	952.72	
Temperature/ K	298	100
Crystal system	Orthorhombic	
Space group	$P2_12_12$	
Unit cell dimension	*a*=10.8150(3) Å *b*=13.8872(3) Å *c*=8.9272(3) Å	*a*= 10.7346(3) Å *b*= 13.7092(4) Å *c*= 8.8120(3) Å
Volume /Å^3	1340.78(7)	1296.80(7)
Density / Mg/m^3	2.360	2.440
μ /mm^{-1}	17.004	17.580
F /000	872	872
Z	2	
Radiation	MoKα (λ = 0.71073)	
2θ range for data collection/°	2.71 to 33.20	2.75 to 33.20
Crystal size/mm^3	0.302 x 0.29 x 0.09	
Reflections collected	5141	4978
Index ranges	-12 ≤ h ≤ 16, -21 ≤ k ≤ 21, -13 ≤ l ≤ 13	-16 ≤ h ≤ 16, -21 ≤ k ≤ 21, -13 ≤ l ≤ 13
Goodness-of-fit on F^2	1.043	1.041
Final R indexes [I>=2σ (I)]	R_1 = 0.0321, wR_2 = 0.0558	R_1 = 0.0235, wR_2 = 0.0590
Final R indexes [all data]	R_1 = 0.0593, wR_2 = 0.0638	R_1 = 0.0251, wR_2 = 0.0582

Source: Elaborated by the author.

The $[BiBr_6]^{3-}$ possesses a distorted octahedra configuration, with Bi-Br bond lengths ranging from 2.831 (8) Å to 2.859 (7) Å. Unlike the regular octahedra found in homogeneous compounds like the guanidinium $[C(NH_2)_3]_3BiBr_6$ compound (Bator *et al.*, 2001), the Br-Bi-Br angles different from the ideal 90° octahedra. To quantitatively assess the distortion of the $[BiBr_6]^{3-}$ units, the distortion parameter (Δd) based on the Bi-Br bond lengths and angle variance (σ) is employed using the following expression:

$$\Delta d = \left(\frac{1}{6}\right)\sum\left(\frac{d_n - d}{d}\right)^2 \quad (1)$$

$$\sigma = \left(\frac{1}{15}\right)\sum\left(\frac{\theta_n - 90}{90}\right)^2 \quad (2)$$

where d is the mean Bi-Br distance and d_n are the six individual Bi-Br, on the other hand, θ_n are the Br-Bi-Br angles (García-Fernández *et al.*, 2018; Katan *et al.*, 2015; Lufaso e Woodward, 2004). The obtained values show that the compound has a Δd = 0.69445 and σ = 2.70 at room-temperature, indicating a significant distortion in the octahedral geometry. Interestingly, the compound $[(CH_3)_2NH_2]_4BiBr_7$ undergoes no structural phase transition at low temperatures. However, a natural decrease in the cell parameters is observed, indicating a contraction of the crystal lattice. The crystal data and structure refinement results for the sample at both room temperature and 100 K are presented in Table 1, providing detailed information on the structural parameters.

Concurrently, a natural decrease in the cell parameters is observed at 100 K, indicating a contraction of the crystal lattice as the temperature decreases. This lattice contraction could be attributed to the reorganization of the molecular components. To gain deeper insights into these structural changes, comprehensive crystallographic data, and structure refinement results for the sample at both room temperature and 100 K are provided in Table 1, offering detailed information about the variations in the structural parameters.

To further investigate the low-temperature distortion effect and elucidate the modifications in the local symmetries, Raman spectroscopy was employed. Raman spectroscopy is a powerful technique that provides valuable insights into the materials vibrational modes and crystal symmetries. By analyzing the Raman spectra, it was detected the changes induced by temperature variations in $[(CH_3)_2NH_2]_4BiBr_7$. The temperature-dependent Raman spectra displayed numerous bands observed in the wavenumber range of 90 to 3250 cm^{-1}. The obtained Raman spectra for the compound where from 20 K to room temperature, as shown in Figures 6 to 12.

Table 2 – Frequencies (ν in cm^{-1}) and proposed assignments of experimental Raman-active modes in $[(CH_3)_2NH_2]_4BiBr_7$ in both temperatures compared for similar compounds $APbX_3$ (A=DMA, MA; X=Br, I) (Ivanovska et al., 2016; Leguy et al., 2016; Rodríguez-Hernández et al., 2022; Samet et al., 2010).

Mode (ν)	293 K (cm^{-1})	10 K (cm^{-1})	Ref. (cm^{-1})	Assignment	Mode (ν)	293 K (cm^{-1})	10 K (cm^{-1})	Ref. (cm^{-1})	Assignment
1	100	113	98-106	ν_{as} (Br-Pb-Br)	42	--	1406		
2	--	118	118	DMA Translation	43	1413	1416	1416-1428	δ_s (NH_2)
3	--	122	126-129	DMA Libration	44	1426	1424	1428	δ_s (CH_3)
4	--	130	126-129	DMA Libration	45	--	1429		
5	--	138	138	DMA Libration	46	--	1446		
6	134	142	138	DMA Libration	47	--	1453		
7	--	150	145-175	DMA Libration	48	1459	1461	1469	δ_{as} (NH_2)
8	154	160	145-175	DMA Libration	49	--	1469		
9	164	174	145-175	DMA Libration	50		1476		
10	--	204			51		1479		
11	--	215			52	--	1552		
12	256	259	262-297	τ (H_3C-N-CH_3)	53	1559	1560	1544-1596	δ_{as} (NH_2)
13	--	283			54	--	1611		
14	--	393	323-326	τ (H_3C-N-CH_3)	55	2756	2761		ν (C-H)
15	400	399	401-402	τ (H_3C-N-CH_3)	56		2774		
16	437	440			57	2786	2779		ν (C-H)
17	--	470			58	2796	2795		ν (C-H)
18	488	483			59	2808	2807		ν (C-H)
19	688	685			60		2817		
20	709	711			61	--	2828		
21	789	789			62	2842	2837	2844	ν (N-H)
22	805	801	803	δ (H_3C-N-CH_3)	63	--	2845		
23	--	822			64		2886		
24	825	827	823	ω (H_3C-N-CH_3)	65	2902	2904	2896	ν_s (C-H)
25	876	874			66		2933		
26	885	890	890-906	ρ (H_3C-N-CH_3)	67	2937	2941	2931-2938	ν_{as} (C-H)
27	1007	1004	994	ν (H_3C-N-CH_3)	68		2952		
28	1014	1013			69	2956	2960	2952-2966	ν_{as} (C-H)
29		1020			70	2961	2964	2961	ν (N-H)
30	1023	1025	1030-1059	ν_{as} (H_3C-N-CH_3)	71		2966		
31	1072	1068			72	3015	3011		
32	1080	1080	1078	ν_{as} (H_3C-N-CH_3)	73	3021	3019	3023	ν_s (C-H) + ν (N-H)
33		1219			74	3027	3028	3026	ν_{as} (C-H)
34		1225			75	3033	3036	3030-3036	ν_s (N-H)
35	1224	1231	1227	ρ (CH_3)	76		3040		
36	1248	1244	1231-1236	ρ_s (CH_3)	77	3090	3085	3080-3106	ν_s (N-H)
37	--	1252			78	3106	3119		ν_s (N-H)
38	--	1356	1351-1353	δ_s (CH_3)	79	3129	3147	3124-3144	ν_{as} (N-H)
39	1365	1362	1366-1370	δ_s (CH_3)	80	3163	3157	3161	ν_{as} (N-H)
40	--	1395			81	3184	3202	3172-3179	ν_{as} (N-H)
41	1404	1403	1399-1403	δ_{as} (CH_3) + ω(NH_2)	82		3209		

Abbreviations: ν: stretching; δ: bending; τ: twisting/torsion; ρ: rocking; ω: wagging; as:asymmetric; s: symmetric.

Source: Elaborated by the author.

To assign the observed modes in the Raman spectra, a comparison was made with other similar compounds, such as methylammonium (MA) $[CH_3NH_3]^+$ $MAPbX_3$ (X=Cl, Br, I) (Ivanovska *et al.*, 2016; Leguy *et al.*, 2016), and the $DMAPbBr_3$ (Rodríguez-Hernández *et al.*, 2022). The proposed assignments of the observed Raman modes at 290 K and 20 K are provided in Table 2. These assignments were based on the similarities in the vibrational characteristics between $[(CH_3)_2NH_2]_4BiBr_7$ and the reference compounds, facilitating the interpretation and analysis of the Raman spectra. By combining the low-temperature crystal structure analysis with the temperature-dependent Raman spectroscopy, it was suggested that $[(CH_3)_2NH_2]_4BiBr_7$ around 100 K displays an order-disorder mechanism modification, which could be attributed to the rearrangement of the distorted octahedral units internal angles, and the definition of the $[(CH_3)_2NH_2]$ organic molecule, this result it has been detected in perovskite-like $DMAPbX_3$ (X =Cl, Br, I) (Rodríguez-Hernández *et al.*, 2022).

The temperature-dependent spectra presented in Figure 6 correspond to the internal vibrations of the Br-Bi-Br (ν_1) and the rigid-body motions of the DMA organic cations modes ν_2 to ν_{11} (translations or/and librations). A noticeable softening of the phonons was observed upon heating, but at $T_{distortion}$ < 100 K, new vibrations related to the movements of the DMA cations were displayed. The distortion in the angle of the octahedra could affect the hydrogen bond between DMA and the $[BiBr_6]^{3-}$ unit, resulting in the observed changes. The shrinking of the DMA molecule may explain the appearance of the new bands since, at low temperatures, the lattice thermal expansion contributes less, which defines the positions of the disorder of both the bromide ion as well as the molecules of the DMA, which could be observed at the CH_2 and CH_3 vibrations. Vibrational modes associated with the internal vibrations of the DMA cation entities within the crystal structure were mainly observed at wavenumbers higher than 200 cm^{-1}. As previously described, the organic and inorganic sublattices can couple, leading to distortion (Grechko *et al.*, 2018; Menahem *et al.*, 2021).

Figure 6 – Left panel: Temperature-dependent normalized Raman spectra obtained for the $[(CH_3)_2NH_2]_4BiBr_7$ between 20-290 K in the 90–300 cm^{-1} range, Right panel: Temperature-dependent behavior of the mode positions observed in this wavenumber region.

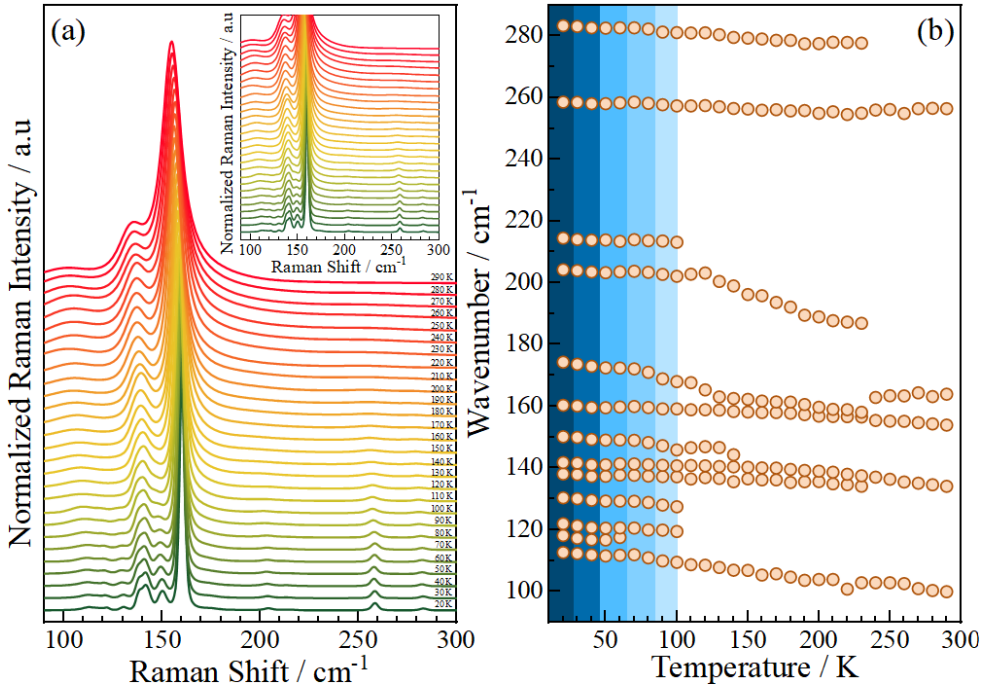

Source: Elaborated by the author.

In particular, hydrogen bonding plays a significant role in the relative stability of the crystal structure. Therefore, it is useful to examine vibrations with contributions from hydrogen bonding interactions (El-Mellouhi *et al.*, 2016; Svane *et al.*, 2017). Figure 7 shows the temperature-dependent behavior of Raman spectra in the range from 300 to 650 cm^{-1}, primarily showing the DMA molecule torsions. This region does not exhibit any discontinuity around 100 K, as well as Figure 8, which displays the temperature dependence of the modes observed between 650 and 1200 cm^{-1}.

The NH_2 or CH_3 bending, stretching, and rocking modes are sensitive to the hydrogen bond between the DMA cation and the inorganic framework, as described by Rodríguez *et al.* (Rodríguez-Hernández *et al.*, 2022). Hence, they serve as suitable probes for investigating this coupling interaction. The CH_3 rocking modes and CH_3 and NH_2 bending of the DMA groups are observed in the wavenumber region between 1200 and 1600 cm^{-1}, as shown in Figure 9.

Figure 7 – Left panel: Temperature-dependent normalized Raman spectra obtained for the $[(CH_3)_2NH_2]_4BiBr_7$ between 20-290 K in the 350–600 cm^{-1} range, Right panel: Temperature-dependent behavior of the mode positions observed in this wavenumber region.

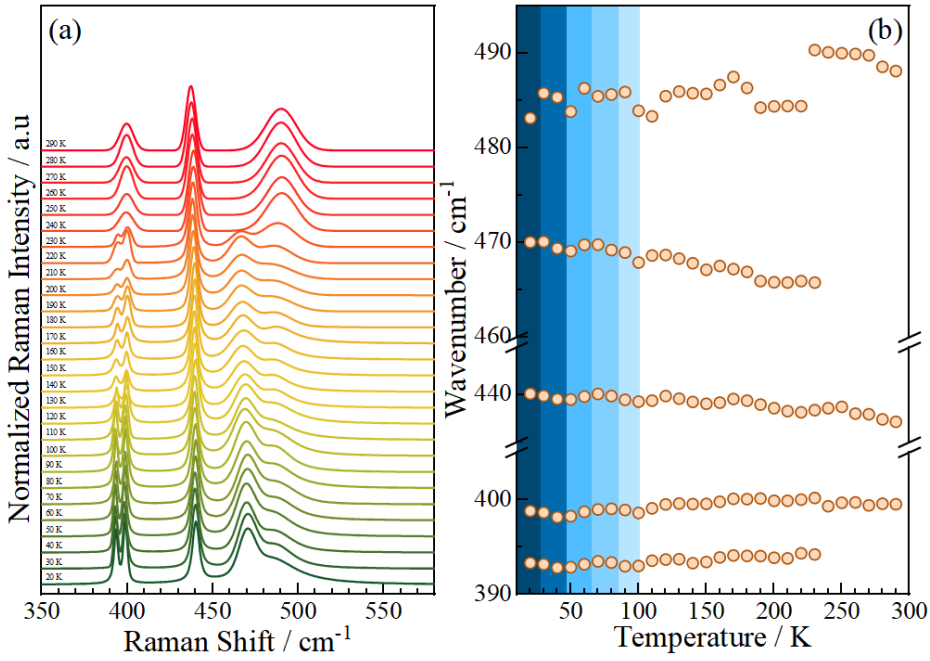

Source: Elaborated by the author.

Interestingly, the ρ (CH_3) and δ_s (CH_3) contribute to the new vibrations, which is not surprising considering the hydrogen bonding interaction between the DMA and the octahedra $[BiBr_6]^{3-}$. Figure 10 shows the measured Raman spectra related to the CH_3 and NH_2 stretching modes. Notably, some of the previously described observations are highlighted in this region, as well as the anomalous hardening (on heating) of the bands at 2786 cm^{-1} and 2842 cm^{-1}. Usually, that shift toward lower wavenumbers is associated with hydrogen bonding effects, which affect the C-H and N-H stretching vibrations (Arunan *et al.*, 2011; Arunan e Mani, 2015; Bordallo *et al.*, 2007; Haughey e Beveridge, 1969), suggesting the presence of hydrogen bonds in the structure. These hydrogen bonds dynamically contribute to the distortion, as illustrated in Figures 11 and 12.

Figure 8 – Left panel: Temperature-dependent normalized Raman spectra obtained for the $[(CH_3)_2NH_2]_4BiBr_7$ between 20-290 K in the 600–1200 cm^{-1} range, Right panel: Temperature-dependent behavior of the mode positions observed in this wavenumber region.

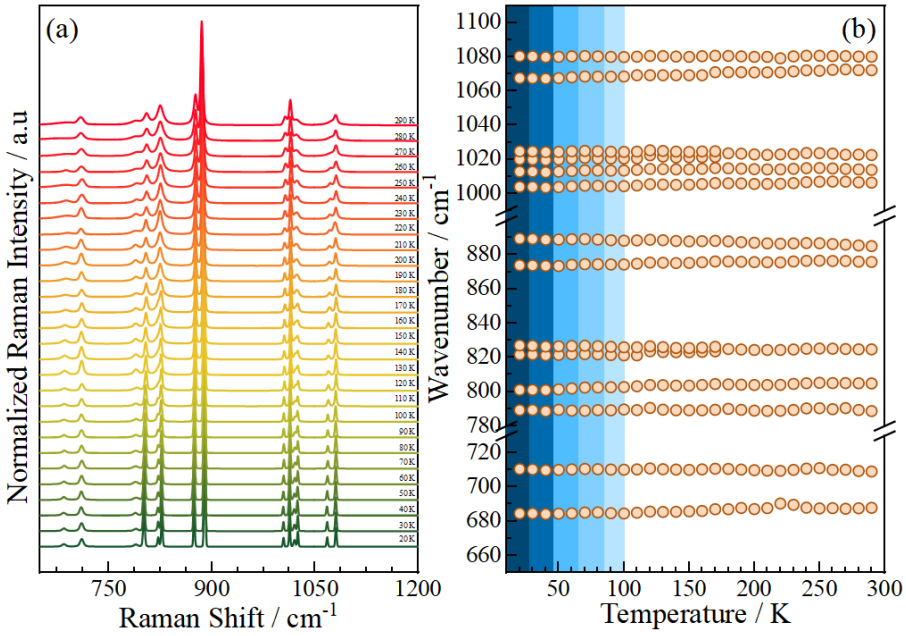

Source: Elaborated by the author.

Figure 9 – Left panel: Temperature-dependent normalized Raman spectra obtained for the $[(CH_3)_2NH_2]_4BiBr_7$ between 20-290 K in the 1200–1650 cm^{-1} range, Right panel: Temperature-dependent behavior of the mode positions observed in this wavenumber region.

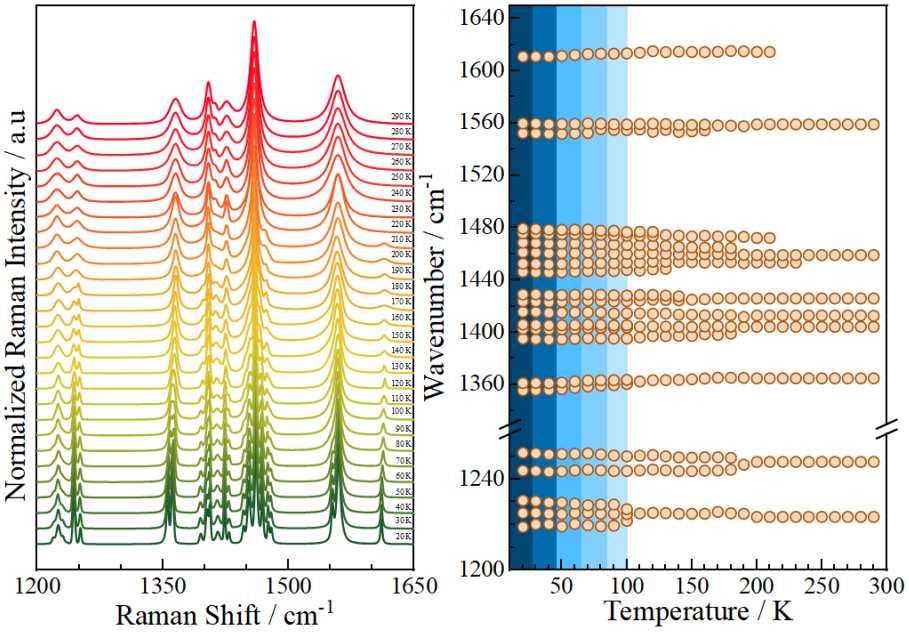

Source: Elaborated by the author.

Figure 10 – Left panel: Temperature-dependent normalized Raman spectra obtained for the $[(CH_3)_2NH_2]_4BiBr_7$ between 20-290 K in the 2750–2860 cm^{-1} range, Right panel: Temperature-dependent behavior of the mode positions observed in this wavenumber region.

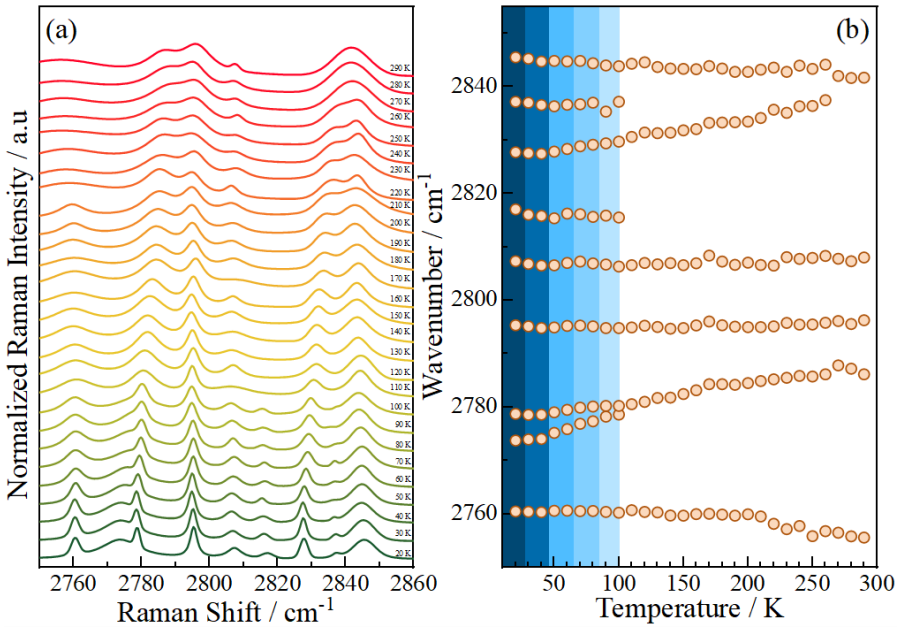

Source: Elaborated by the author.

Figure 11 – Left panel: Temperature-dependent normalized Raman spectra obtained for the $[(CH_3)_2NH_2]_4BiBr_7$ between 20-290 K in the 2870–3050 cm^{-1} range, Right panel: Temperature-dependent behavior of the mode positions observed in this wavenumber region.

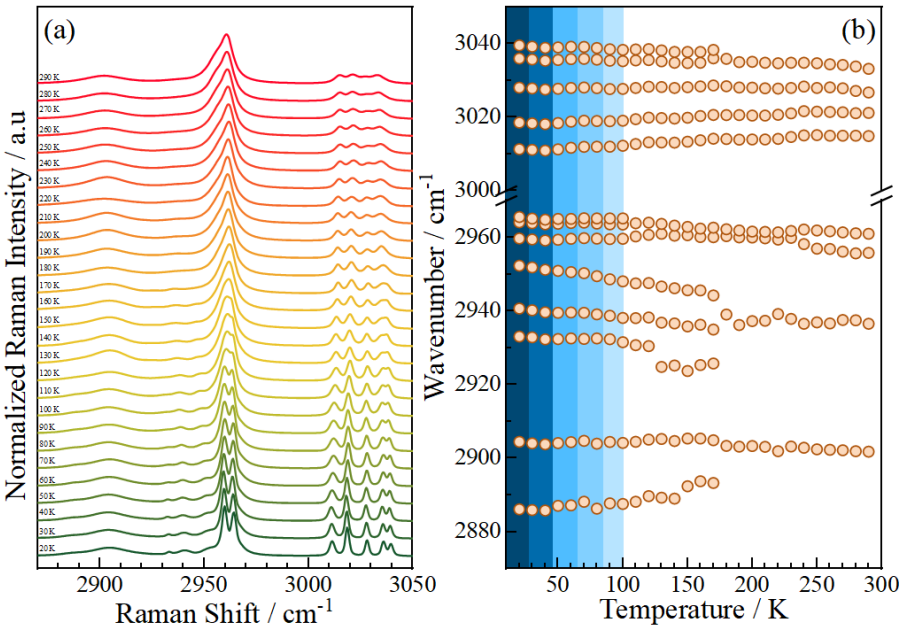

Source: Elaborated by the author.

Figure 12 – Left panel: Temperature-dependent normalized Raman spectra obtained for the $[(CH_3)_2NH_2]_4BiBr_7$ between 20-290 K in the 3050–3250 cm^{-1} range, Right panel: Temperature-dependent behavior of the mode positions observed in this wavenumber region.

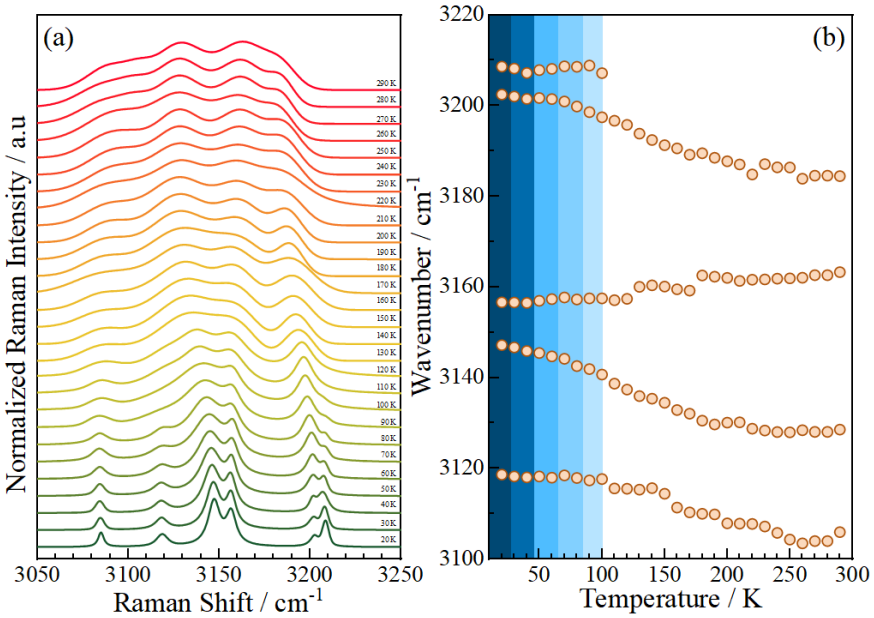

Source: Elaborated by the author.

Furthermore, it has been observed that the weakening of the intermolecular interactions (*H*-bond) upon heating indicates the correlation with the DMA^+ cation dynamics in the high-temperature related to the frameworks. These observations suggest that the dynamics of the DMA cations and the framework are strongly coupled and contribute to the octahedra distortion. The observed changes in the Raman modes analysis demonstrate a correlation between the strength of hydrogen bonding, the free motion of the DMA, the effect and contribution of the distortion of the octahedra, and the order-disorder DMA mechanisms. The comprehensive analysis of the temperature-dependent Raman spectra provides a deeper understanding of the structural dynamics and hydrogen bonding effects in $[(CH_3)_2NH_2]_4BiBr_7$, which is essential for harnessing its unique properties and exploring its potential in optoelectronic applications.

3.2 Examining the Photoluminescence Properties

The metal halide ionic octahedron is the fundamental structural unit in halide perovskites, influencing their optoelectronic and chemical properties. As a result, the dynamic behaviors of metal halide perovskites can be correlated with their responses to various environmental stimuli. Low-temperature Single-Crystal X-Ray Diffraction (SCXRD) and Raman spectroscopy studies on $[(CH_3)_2NH_2]_4BiBr_7$ have shown that at temperatures below $T_{distortion} < 100$ K, there is an increase in the distortion of the $[BiBr_6]^{3-}$ octahedra, as evidenced by modifications in the internal angles. These structural changes also impacted the hydrogen bonds within the compound.

The low-dimensional nature of the perovskite-like structure is an essential aspect to consider. This characteristic allows for efficient localization and confinement of excitons within the crystal lattice, forming self-trapped excitons (STEs) (Liu S. *et al.*, 2021; Roy *et al.*, 2021). The strong interaction between excitons and phonons further enhances the stability and radiative recombination of these STEs, giving rise to the observed broad emission spectra. The difference in photoluminescence (PL) profiles between high and low temperatures can be attributed to the interplay between thermal lattice effects and electron-phonon interactions (Han *et al.*, 2022). Both processes are maximized at elevated temperatures, leading to a non-radiative emission path. However, at lower temperatures, lattice relaxation facilitates the generation of electron-hole pairs, promoting STEs states with radiative emissions, which aligns with the observed photoluminescence spectra centered around 425 nm (Blue-Turquese) at 90 K.

Figure 13 shows the PL measurements at low temperatures of the $[(CH_3)_2NH_2]_4BiBr_7$. Observe that when the temperature decreases, the intensity of the PL spectra emission increases. In addition, was observed a notable blueshift in the emission of the sample as the temperature gradually decreased from 90 to 14 K. It is important to highlight that the compound exhibited the production of STEs. Accordingly, STEs are a band-to-band luminescence, indicating that electrons in the conduction band recombine with holes in the valence band, and the recombination process emits a phonon by a defect (Li *et al.*, 2019; Shi, Y. *et al.*, 2021). Thus, once electrons and holes are photogenerated, these excitons are self-trapped instantly because these self-trapped states are accessible and more stable in the presence of lattice distortion.

Figure 13 – The low-temperature photoluminescence evolution spectra in the $[(CH_3)_2NH_2]_4BiBr_7$ compound.

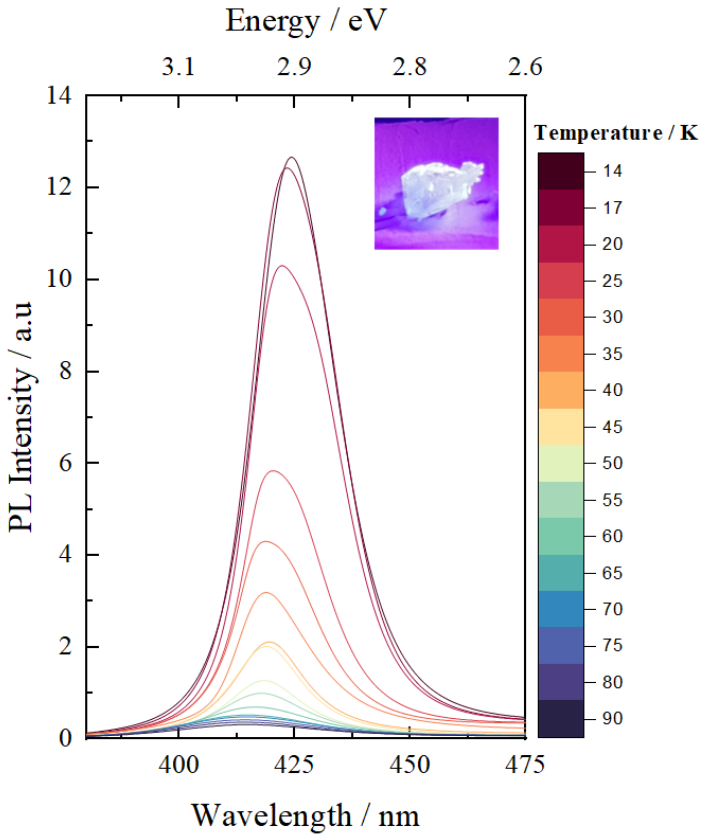

Source: Elaborated by the author.

Photoluminescence spectroscopy has revealed that the PL spectra are highly sensitive to structural distortions and the presence of electronic charge carriers. These factors influence the energy emission, intensity, and full width at half maximum (FWHM) of the broadband emission, and they are directly linked to the significant dependency of STEs emissions on structural distortions. Notably, low-dimensional perovskite-type materials with distorted octahedra, intrinsically exhibiting electron-phonon interaction, are more likely to produce STEs emissions. In some cases, these states can only be accessed under specific external conditions that help relax the crystal structure, further increasing the contribution of STEs states (Li *et al.*, 2020; Zhang *et al.*, 2021). The strength of electron-phonon can be evaluated by the Huang-Rhys factor $S = \Delta E/\hbar\omega$, which is the number of phonons emitted after the carrier capture (Whalley *et al.*, 2021). All STE recombination processes could be explained and fitted (see Figure 14) by the equations described in Table 3.

Table 3 – Fitted values of the adjustments for the PL center and FWHM parameters with equations (3-5) where k_b in all the expressions is the Boltzmann constant ($8.617\ x10^{-5}$ eV/K).

$E(T) = E_0 + A_{TE}T + A_{EP}\left[\frac{2}{e^{\frac{\hbar\omega}{k_bT}}-1}+1\right]$ (3)	$E_{g\,(T=0)}$ (eV)	A_{TE} (meV/K)	A_{EP} (meV)	$\hbar\omega$ (meV)
	2.97 ± 0.03	3.16 ± 0.01	140± 30	16 ± 3
$I(T) = \left[\frac{I_0}{1+Ae^{\frac{-E_A}{k_bT}}}\right]$ (4)	I_0 (μa.u)	A	E_A (meV)	
	7.9 ± 0.3	-	10.6 ± 0.9	
$\Gamma(T) = \Gamma_0 + \gamma_{ac}T + \frac{\gamma_{LO}}{e^{\frac{E_{LO}}{k_bT}}-1}$ (5)	Γ_0 (meV)	γ_{ac} (meV/K)	γ_{LO} (meV)	E_{LO} (meV)
	0.4 ± 0.1	4 ± 1	60 ± 16	7 ± 3

Source: Elaborated by the author.

Figure 14– The PL parameters (a) center, (b) intensity, and (c) FWHM for $[(CH_3)_2NH_2]_4BiBr_7$.

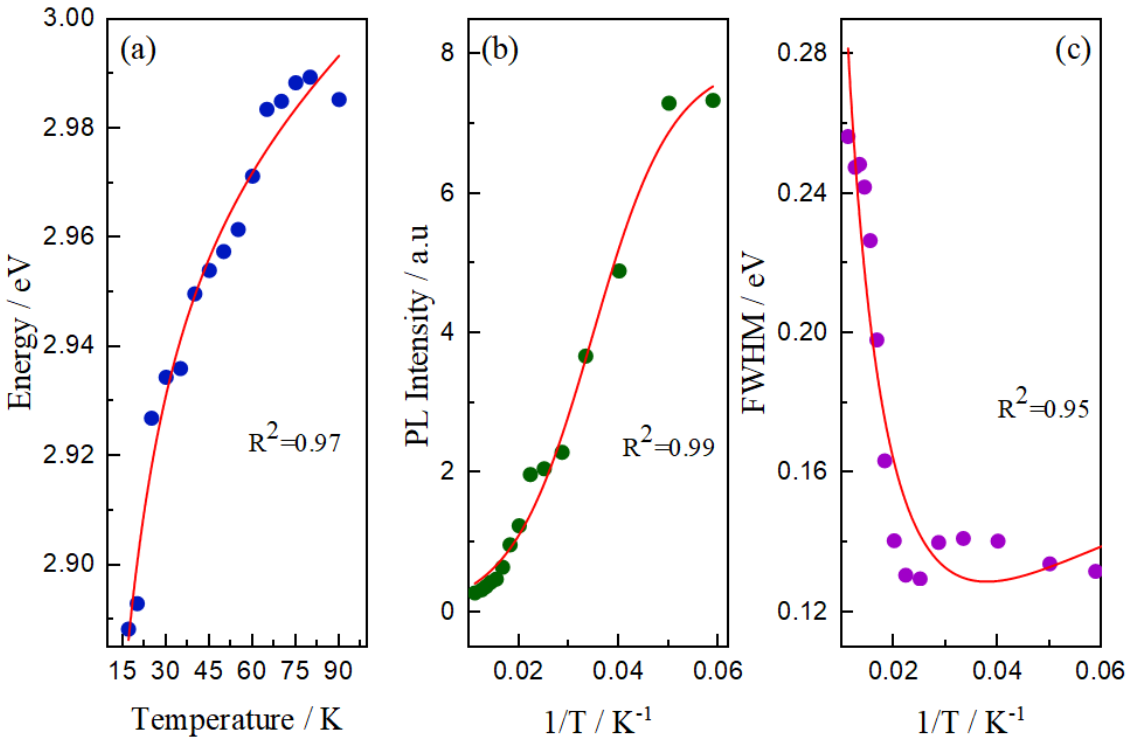

Source: Elaborated by the author.

The energy-temperature relationship (Figure 14 (a)) $E(\mathrm{T})$ in the system can be described as the sum of distinct contributions, including the unrenormalized bandgap at $T = 0$ (E_0), the electron-phonon energy interaction (A_{EP}), the weight thermal expansion (A_{TE}), and $\hbar\omega$ representing the average optical phonon energy. Using the fitted values, the Huang-Rhys factor $S = \Delta E/\hbar\omega$ of the $[(CH_3)_2NH_2]_4BiBr_7$ is 8.8, which indicates a strong electron-phonon coupling regime, similar to other halide perovskite such as the inorganics $CsPbBr_3$ ($S = 12$) (Pan *et al.*, 2022).

Characterizing the photoluminescence behavior of the system involves several crucial parameters in the intensity model. Firstly, I_0 represents the PL intensity at $T = 0$. Additionally, E_A, indicates the contribution of thermal dissociation of self-trapped excitons (STEs) to enhance the PL intensities. It represents the energy required for the thermal activation process that promotes the release of carriers and subsequent increases in PL intensity. The constant factor A, dependent on the luminescence lifetime, helps understand the dynamics of the emitted light (Sahoo et al., 2022). It reflects the interplay between radiative and nonradiative decay processes, providing insights into the radiative recombination efficiency and overall lifetime of excitonic states (see Figure 14(b)).

The full width at half maximum (FWHM) function is influenced by associated parameters that contribute to the broadening of the PL spectra (see Figure 14 (c). Γ_0 captures scattering effects arising from disorder and crystallographic imperfections in the material. It represents the FWHM value at T = 0 K, reflecting the intrinsic broadening without thermal effects. The FWHM adjustment includes terms related to homogeneous broadening. Specifically, the Fröhlich coupling constants γ_{ac} and γ_{LO} account for the interaction between charge carriers and acoustic and longitudinal optical phonons (Iaru *et al.*, 2021). These terms influence the dynamics of excitonic states and contribute to broadening the PL spectra. Additionally, the phonon energy, represented by E_{LO}, lays a crucial role in determining the energy scale associated with the phonon modes involved in electron-phonon interactions. Finally, electron-phonon interaction in the sample, as indicated by the activation energy E_A= 10.6 meV, is closely tied to the exciton-phonon coupling characterized by the activation energy E_{LO}=7 meV. This coupling enables phonon-assisted electronic transitions, enhancing the photoluminescence intensity through the population of phonons.

Figure 15 – CIE-1931 color space with the temperature-dependent chromaticity coordinates of PL emissions of $[(CH_3)_2NH_2]_4BiBr_7$ (blue dots).

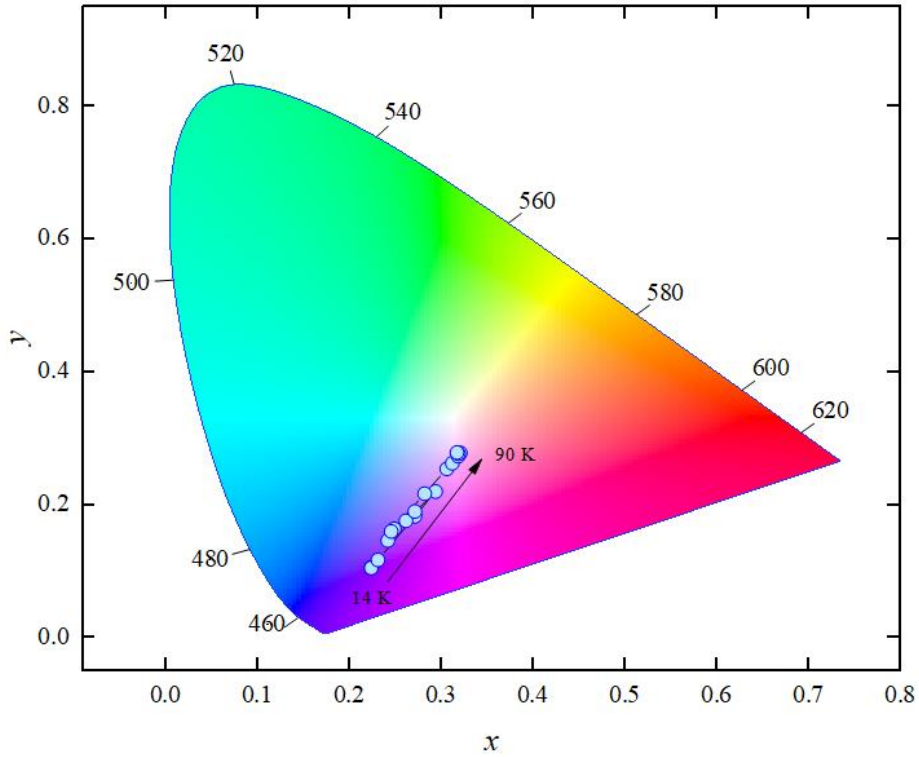

Source: Elaborated by the author.

Table 4 – Temperature-dependent chromaticity coordinates

Temperature (K)	CIE *x*	CIE *y*
14	0.22357	0.10577
17	0.2237	0.10487
20	0.23084	0.11704
25	0.27109	0.18283
30	0.29351	0.21994
35	0.26129	0.17593
40	0.27111	0.18981
45	0.2416	0.1461
50	0.24874	0.16362
55	0.24544	0.1599
60	0.28181	0.21665
65	0.3058	0.25402
70	0.31187	0.26258
75	0.31827	0.27334
80	0.32058	0.27811
90	0.31853	0.27706

Source: Elaborated by the author.

The potential applications of the $[(CH_3)_2NH_2]_4BiBr_7$ as blue-turquoise light-emitting diodes (LEDs) were investigated by evaluating the spectral power distribution using the CIE 1931 color space curve, which characterizes the (*x,y*) chromaticity coordinates (Zhu *et al.*, 2019). Figure 15 displays the chromaticity coordinates of the CIE-1931 color space as a temperature function; the corresponding values are provided in Table 4.

At 90 K, the photoluminescence (PL) emitted by self-trapped excitons (STEs) produces a distinct blue-turquoise color. As the temperature decreases, the chromaticity coordinates exhibit variations, leading to a shift in the perceived color. This behavior aligns with the earlier discussion on the blueshift of the PL center. Remarkably, light violet emission is observed at the lowest temperature, showcasing the material's optical properties and tunability.

The investigation of the hybrid perovskite-like $[(CH_3)_2NH_2]_4BiBr_7$ at low temperatures has provided valuable insights into the effects of distorted octahedra on its luminescent properties. The modification of internal angles within the $[BiBr_6]^{3-}$ octahedra permits the appearance of novel self-trapped exciton (STEs) contributions, resulting in a blue-turquoise (425 nm) PL emission at 90 K. Furthermore, at low temperatures, the PL profile exhibits a blueshift behavior, demonstrating the sample ability to tune the color emission from blue turquoise to light violet at different temperature values.

4 Pressure-induced structural phase transition on the 2D structure $CsPb_2Cl_5$

Numerous studies have extensively investigated the remarkable properties of metal halide perovskite (MHP) materials, which exhibit versatility in various forms, including thin films, micro/nanocrystals, and bulk crystals (Zhang, J., Hodes, Jin e Liu, S. (Frank), 2019). These compounds, particularly the lead-based MHPs with Cs-Pb-X (where X represents chloride (Cl), bromide (Br), and iodide (I) elements), have gained considerable traction in the industry due to their remarkable advancements (Bati et al., 2023; Wang, Y. P. et al., 2023). These efforts aim to mitigate the detrimental effects of moisture, oxidation, and other environmental influences, ensuring the sustained performance and longevity of the materials in practical applications. Consequently, these remarkable properties and advancements have positioned these materials as promising candidates for a wide range of optoelectronic devices, including solar cells, light-emitting diodes (LEDs), photodetectors, and sensors (Akkerman et al., 2017; Hu et al., 2022b; Song et al., 2015; Zhang et al., 2015).

The chemical composition of perovskites determines their crystal structure and stability, but their most attractive properties lie in the halide- and size-dependent bandgap tuning and carrier confinement, which govern the generation, dynamics, and recombination of charge carriers and excitons (Cao *et al.*, 2020b; Chouhan *et al.*, 2020; Ullah *et al.*, 2021). In particular, Cs-Pb-X compounds, such as $CsPb_2X_5$, have intriguing characteristics due to their distinctive crystal structure. $CsPb_2X_5$ consists of layers of octagonal-shaped PbX_8 polyhedra forming a unique two-dimensional (2D) arrangement, with Cs^+ ions occupying the interstitial spaces between the layers (Chen, Y. *et al.*, 2018a; Li *et al.*, 2022).

This 2D structure enhances the stability of the $CsPbX_5$, contrary to the $CsPbX_3$ compounds, against moisture in an air environment, with benefits from the intrinsic two-dimensional (2D) structure, which made them gain considerable attention as potential candidates for light-emitting diodes LEDs applications (Protesescu *et al.*, 2015), photodetectors (Li *et al.*, 2020), lasers (Zhang *et al.*, 2021), flexible electronics (Wang *et al.*, 2022), and solar cell applications (Jena, Kulkarni e Miyasaka, 2019; Yin *et al.*, 2015) due to their low cost, elemental constituents, and straightforward crystallization. Despite the enhanced optical properties exhibited by $CsPb_2X_5$ (Huang *et al.*, 2020; Ruan *et al.*, 2017; Wang *et al.*, 2016a), several challenges remain regarding the underlying mechanisms of its structural evolution and electronic properties (Li, J. *et al.*, 2017a; Zhang, T., Chen, Zhihui, Shi e Xu, Q.-H., 2019),

which directly impact its performance and can be modified under extreme conditions, such as low temperatures and high pressures, opening up new possibilities for applications.

The optical properties and structural behavior of $CsPb_2Cl_5$ have received significant research attention due to their similarities to Pb-based perovskite counterparts, such as $CsPbCl_3$ (Behera *et al.*, 2018; Bhat *et al.*, 2021; Stefanski *et al.*, 2021). The face-connected layers of $PbCl_8$ polyhedra in $CsPb_2Cl_5$ induce significant lattice distortions, playing a crucial role in enhancing the creation of self-trapped excitons (STE) even at room temperature. Interestingly, the photoluminescence (PL) characteristics of $CsPb_2Cl_5$ strongly depend on the excitation energy. At higher excitation energies (>3.85 eV), excitons centered at 2.32 eV dominate the emission. However, at lower excitation energies (<3.85 eV), a remarkable phenomenon occurs, resulting in the emergence of self-trapped excitons (STE) as the primary emission feature. These self-trapped excitons exhibit a broadband emission centered at 1.8 eV with a broad full width at half maximum (FWHM) exceeding 120 nm, highlighting the unique optical properties of $CsPb_2Cl_5$ (Xu et al., 2021a; Yao et al., 2021).

The pressure-induced modifications in related compounds, such as $CsPb_2Br_5$, have also garnered attention. Previous studies (Ma *et al.*, 2019a) have reported a reversible isostructural phase transition at a critical pressure of 1.6 GPa from the *I*4/*mcm* phase, as confirmed by Angle Dispersive Synchrotron X-Ray Diffraction (ADXRD) experiments. These investigations demonstrated a gradual increase in the absorption onset with pressure, with a notable shift occurring at the critical pressure (Drushliak e Szafrański, 2022a). Similar studies have been conducted on perovskite compounds, such as $CsPbBr_3$ and $CsPbCl_3$, revealing that lattice distortions characterized by variations in Pb-X bond lengths and PbX_6 octahedral tilts influence the energy gaps in these materials. The compression of B−X bonds and bending−X−B bond angles can lead to intriguing phenomena under extreme conditions (Zhang, L. *et al.*, 2018; Zhang, Zeng e Wang, 2017).

To provide a comprehensive analysis of the structural-property changes under high pressure in $CsPb_2Cl_5$ was being systematically examined the crystal structure obtained using the synchrotron facility - Laboratório Nacional de Luz Síncrotron (LNLS) and Raman spectroscopy performed on powder crystals of $CsPb_2Cl_5$. The analysis was based on two high-impact journals publications (*The Journal of Physical Chemistry C:* IF-4.177) with the name: ***Pressure-Induced Structural and Optical Transitions in Luminescent Bulk Cs_4PbBr_6*** (Castro

Ferreira, Araújo, Gómez, M. A. P., et al., 2022) and (Crystal Growth & Design: IF-4.010) with the name: ***The Effect of High Pressure on Polymorphs of a Derivative of Blatter's Radical: Identification of the Structural Signatures of Subtle Phase Transitions*** (Broadhurst *et al.*, 2023).

4.1 Response of the Unit Cell Dimensions to Pressure

The crystalline structure of $CsPb_2Cl_5$ at room temperature was accurately confirmed using the Single-Crystal X-Ray Diffraction (SCXRD) technique. The crystal data and structure refinement results for the sample are presented in Table 5. The obtained crystallographic parameters indicate that the crystal belongs to the tetragonal space group P_I: *I*4/*mcm* (140), consistent with (Chen, Y. *et al.*, 2018b). The obtained cell parameters are $a = b = 8.1523$ (3) Å, $c = 14.8068$ (10) Å and $V = 984.06$ (10) $Å^3$. To explore the pressure dependence of $CsPb_2Cl_5$, the Synchrotron Powder X-Ray Diffraction (SPXRD) measurements were conducted, shedding light on its structural behavior under varying pressures. The corresponding pressure-dependence SPXRD is illustrated in Figure 16. Remarkably, up to $P_c^{I\text{-}II} = 1.27$ GPa, the diffraction patterns consistently exhibit the same crystal structure characterized by the *I*4/*mcm* space group, which suggests that the material maintains its structural phase within this pressure range. However, beyond this pressure, an intriguing structural phase transition occurs, leading to a modification in the crystal structure where the P_I transforms, as it will be shown, into the P_{II}: *I*4/*m* (87), which persists until $P_c^{II\text{-}III} = 4.69$ GPa, involving another SPT from P_{II} into the P_{III}: *C2* (5). After, no remarkable changes at $CsPb_2Cl_5$ undergo any other phase transformation until the explored pressure range.

The diffraction patterns observed at the P_I and P_{II} phases exhibit similar characteristics, featuring a tetragonal *I* base. However, a closer analysis reveals a decrease in the intensity of specific diffraction peaks, particularly those around 10°, 19°, and 24°. This decrease provides clear evidence of a crystal modification occurring during the P_{II} phase, despite maintaining the same crystallographic tetragonal system. Furthermore, the diffractograms obtained during the transition from P_{II} to P_{III} exhibit abrupt changes. The diffraction peak profiles illustrate the presence of new angle reflections, particularly noticeable around 8°, 11°, and 13°. Additionally, at higher 2θ angles, the number of displayed diffraction peaks becomes denser, resulting in decreased peak resolution. These observations can be attributed to the decreased structural symmetry within the crystal lattice.

Table 5 – Crystal data and structure refinement for $CsPb_2Cl_5$

Empirical formula	$CsPb_2Cl_5$
Formula weight	724.54
Temperature/K	298.0
Crystal system	Tetragonal
Space group	*I*4/*mcm*
a/Å	8.1523 (3)
c/Å	14.8068 (10)
Volume/Å^3	984.06 (10)
Z	4
ρ_{calc}g/cm^3	4.890
μ/mm^{-1}	39.091
F(000)	1216
Crystal size/mm^3	0.452 x 0.424 x 0.13
Radiation	MoKα (λ = 0.71073)
2θ range for data collection/°	2.75 to 28.12
Index ranges	$-10 \leq h \leq 10$, $-10 \leq k \leq 10$, $-19 \leq l \leq 19$
Reflections collected	6172
Independent reflections	348 [R_{int} = 0. 0597, R_{sigma} = 0. 0413]
Goodness-of-fit on F2	1.136
Final R indexes [I>=2σ (I)]	R_1 = 0.0316, wR_2 = 0.0787
Final R indexes [all data]	R_1 = 0.0413, wR_2 = 0.0797

Source: Elaborated by the author.

The crystallographic analysis of $CsPb_2Cl_5$ was carried out with the highest precision, employing the Rietveld method implemented in the EXPO2014 software (Altomare *et al.*, 2013). The diffractograms obtained for the P_I were refined within the I4/mcm space group determined in the SCXRD. A systematic methodology was adopted to elucidate the crystal structures of the P_{II} and P_{III} phases. Initially, the interest phase was indexed using the DICVOL program (Boultif e Louër, 2004) implemented in EXPO2014. This indexing step enabled the determination of essential parameters such as the lattice system and unit cell parameters, laying the foundation for subsequent analysis; to explore the possible crystal structures, a group-subgroup diagram was employed to identify potential symmetry changes between different phases.

Consequently, the symmetry of each structure was rigorously verified using the pseudosymmetry search tools available at the Bilbao Crystallographic Server (La Flor, de *et al.*, 2016). This meticulous verification process ensured the accuracy and reliability of the determined symmetry. Finally, the verified symmetry and crystal cells were used as inputs to

simulate the new structure by the thermal annealing function, incorporating the atomic positions of the elements within the compound. The experimentally observed diffraction patterns were refined using the appropriate simulated models derived from the past process. This iterative refinement procedure allowed for meticulously determining the crystal structure for the high-pressure phases of $CsPb_2Cl_5$. The Rietveld refinement of each phase is shown in Figure 17, providing detailed information on the corresponding tolerance factors. The fractional atomic coordinates of each refinement are described in Table 6.

Figure 16 – Variation of the SPXRD pattern of the $CsPb_2Cl_5$ under pressure.

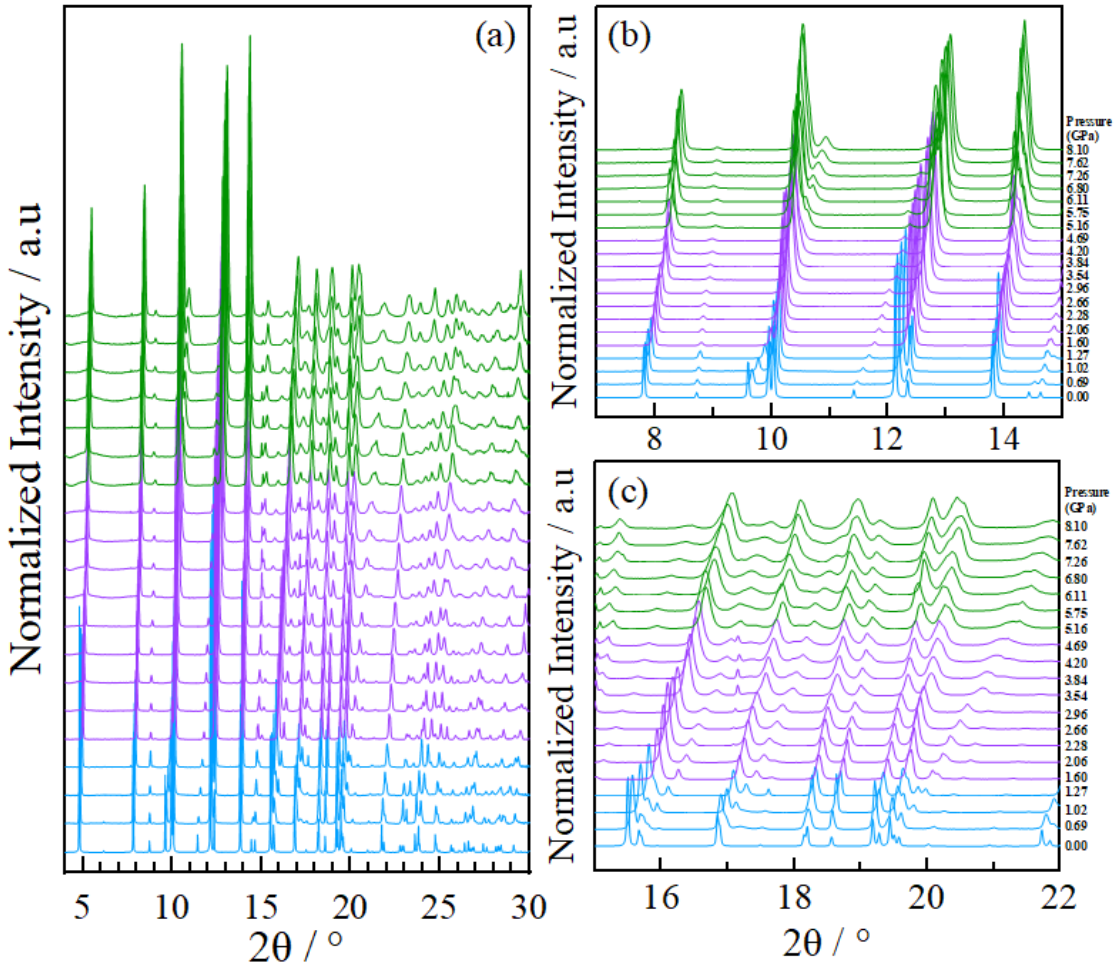

Source: Elaborated by the author.

To establish a comparison between the structure and unit cell parameters, a thorough investigation was conducted to determine the *C*2 space group base into the tetragonal phases, resulting in the transformation: $(1/\sqrt{2})a = a_{C2}$; $(1/\sqrt{2})b = b_{C2}$; $(2\sin(\beta_{C2}))\ c = c_{C2}$). These features contribute to the enhanced understanding of the structural arrangement and provide important

insights for further analysis. The crystal structure of $CsPb_2Cl_5$ exhibits three distinct phases induced by pressure, namely P_I, P_{II}, and P_{III}; all phases presented bicapped trigonal prisms of $PbCl_8$ polyhedral units are interconnected through their faces, forming layers perpendicular to the *c*-axis in each phase in P_I, P_{II}, and to *a*-axis for P_{III}. These layers arrange themselves in a two-dimensional (2D) configuration, while Cs^+ cations act as spacers between the layers. It is worth noting the robustness of the 2D arrangement, which remains well-preserved under the influence of hydrostatic compression, as shown in Figure 18.

Figure 17 – Rietveld refinement of $CsPb_2Cl_5$ at selected hydrostatic pressures.

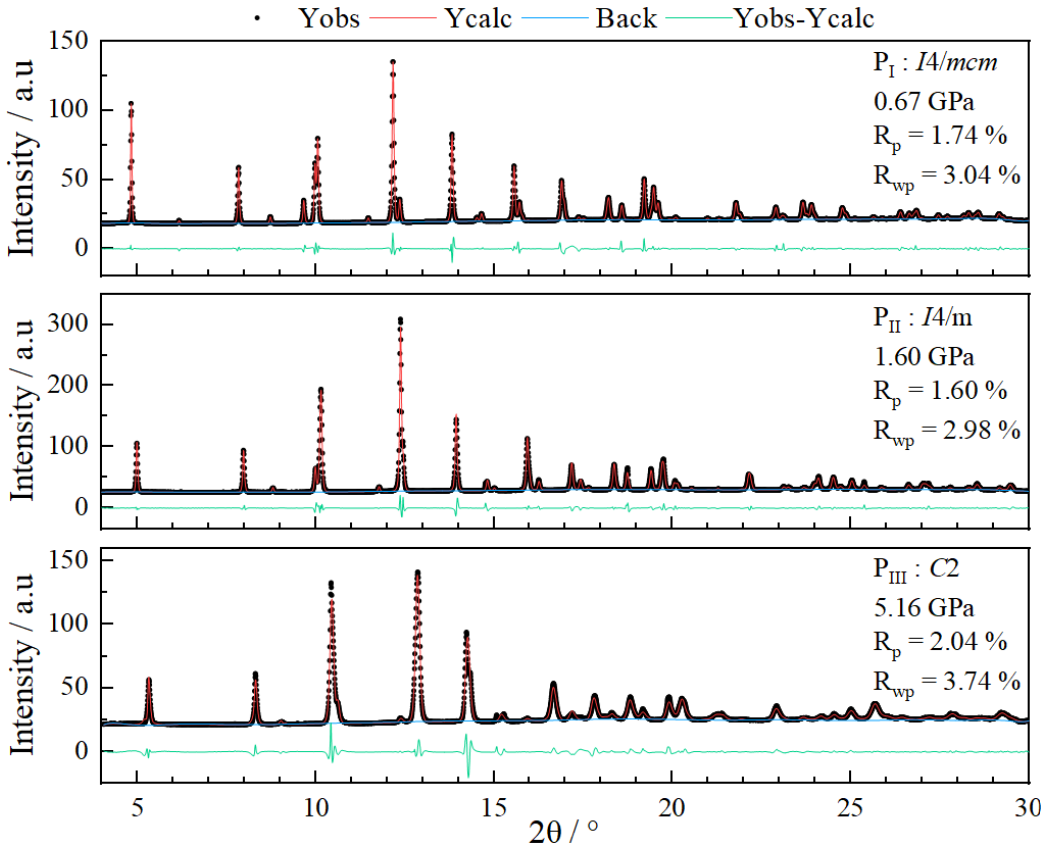

Source: Elaborated by the author.

Table 6– Fractional atomic coordinates and equivalent isotropic displacement parameters in Å for I, II and III phases of $CsPb_2Cl_5$.

			a = 8.1428 (6) Å, c = 14.712 (2) Å				
Pressure: 0.67 GPa							
			Volume: 974.71 (11) Å^3, Space Group: *I*4/*mcm*, Z: 4				
Element	Name	x	Y	z	Occ.	U	Site
Pb	Pb_1	0.664	0.836	0.5	1	0.029	8h
Cs	Cs_1	0.5	0.5	0.25	1	0.035	4a
Cl	Cl_1	0.8379	0.662	0.3658	1	0.025	16l
Cl	Cl_2	0.5	0.5	0.5	1	0.027	4c

			a = 8.0770 (3)Å, c = 14.2374 (10)Å				
Pressure: 1.60 GPa							
			Volume: 928.82 (8) Å^3, Space Group: *I*4/*m*, Z: 4				
Element	Name	x	y	z	Occ.	U	Site
Pb	Pb_1	0.3349	0.1601	0.5	1	0.03	8h
Cs	Cs_1	0	0	0.7382	1	0.04	4e
Cl	Cl_1	0.173	0.343	0.6328	1	1.00	16i
Cl	Cl_2	0.5	0.5	0.5	1	1.00	2a
Cl	Cl_3	0	0	0.5	1	0.01	2b

Pressure: 5.67 GPa			a = 11.174(2) Å, b = 11.2142 (15) Å, c = 8.724 (8) Å β = 129.82 (6) ° Volume: 839.7(11) Å^3, Space Group: *C*2, Z: 4				
Element	Name	x	y	z	Occ.	U	Site
Pb	Pb_6	0.5	0.2999	0.5	1	1.00	2b
Cs	Cs_1	0	0.71	0	1	0.01	2a
Pb	Pb_5	0.186	0.46	0.536	1	0.01	4c
Pb	Pb_4	0.5	0.614	0.5	1	1.00	2b
Cl	Cl_1	0.1	0.6	0.8	1	1.00	4c
Cs	Cs_2	0.5	0.7	1	1	0.02	2a
Cl	Cl_6	0.3	1	0.797	1	1.00	4c
Cl	Cl_7	0.499	0.5	0.805	1	1.00	4c
Cl	Cl_9	0.3	0.8	1.2	1	1.00	4c
Cl	Cl_{10}	0.28	0.71	0.568	1	1.00	4c

Source: Elaborated by the author.

Figure 18 – Crystal structures of phases (a) P_I, (b) P_{II}, and (c) P_{III}.

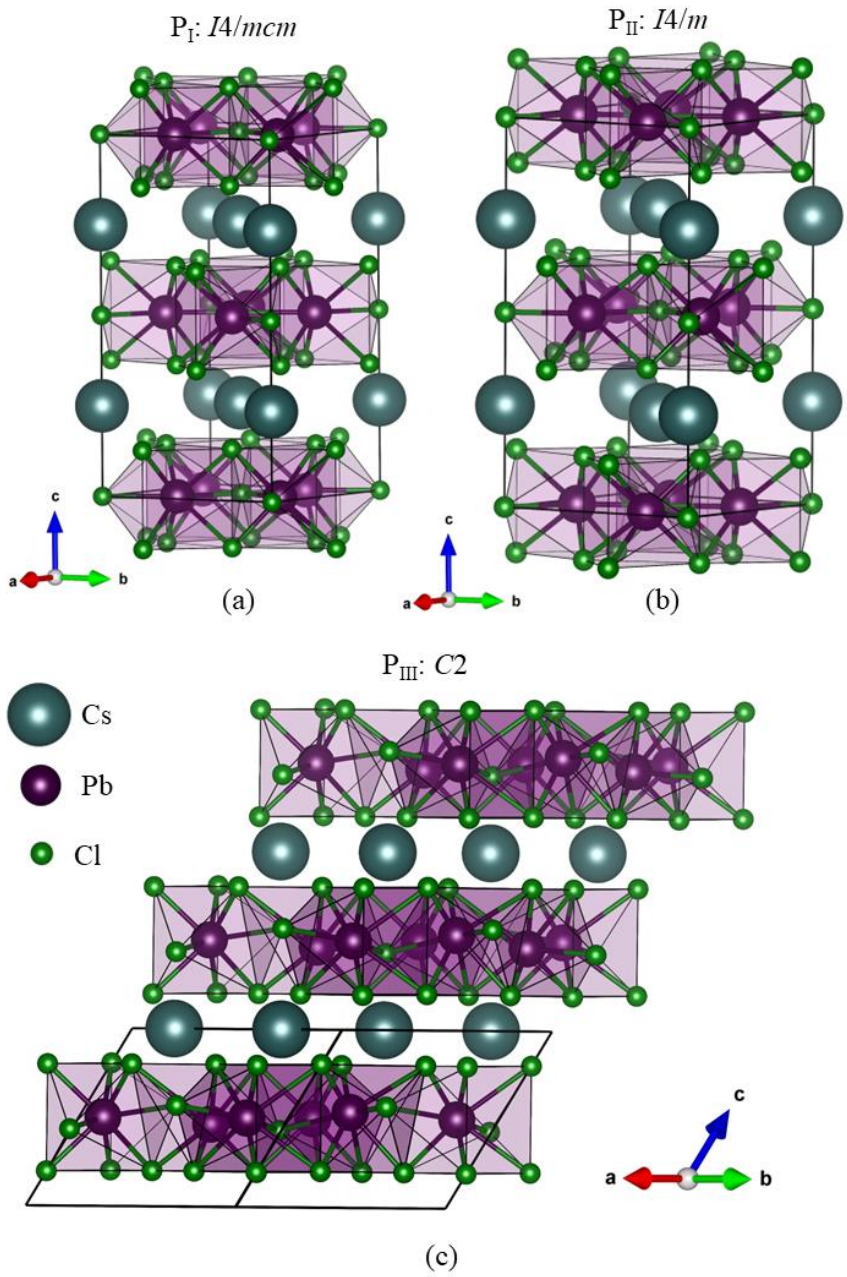

Source: Elaborated by the author.

The pressure dependence of the crystal cell parameters of $CsPb_2Cl_5$ is systematically investigated across a wide pressure range, extending up to 8.11 GPa, as depicted in Figure 19a. Notably, distinct discontinuities in the pressure-dependent behavior of all lattice parameters are observed around the P_I and P_{II}. A remarkable feature is observed between P_{II} to P_{III}, where a pronounced shift occurs, characterizing a significant structural phase transition. The

transformation of the lattice parameters from *a* related to P_{II} into *a* and *b* for P_{III} is the main characteristic of this transition. These abrupt changes signify both phase transitions in the sample, providing compelling evidence for the sensitivity of the crystal lattice to external pressure. This unexpected behavior challenges conventional expectations and underscores the complexity of the structural response to high pressure in $CsPb_2Cl_5$. Importantly, despite the considerable alterations in the crystal cell parameters, a consistent monotonic contraction of the crystal volume is observed throughout the investigated pressure range. This unidirectional change in volume points towards intricate structural modifications within the crystal lattice, further emphasizing the complex nature of the compound's response under high pressures.

Figure 19 – (a) The lattice parameters as a function of pressure. (b) Third-order Birch-Murnanghan fit for each pressure phase.

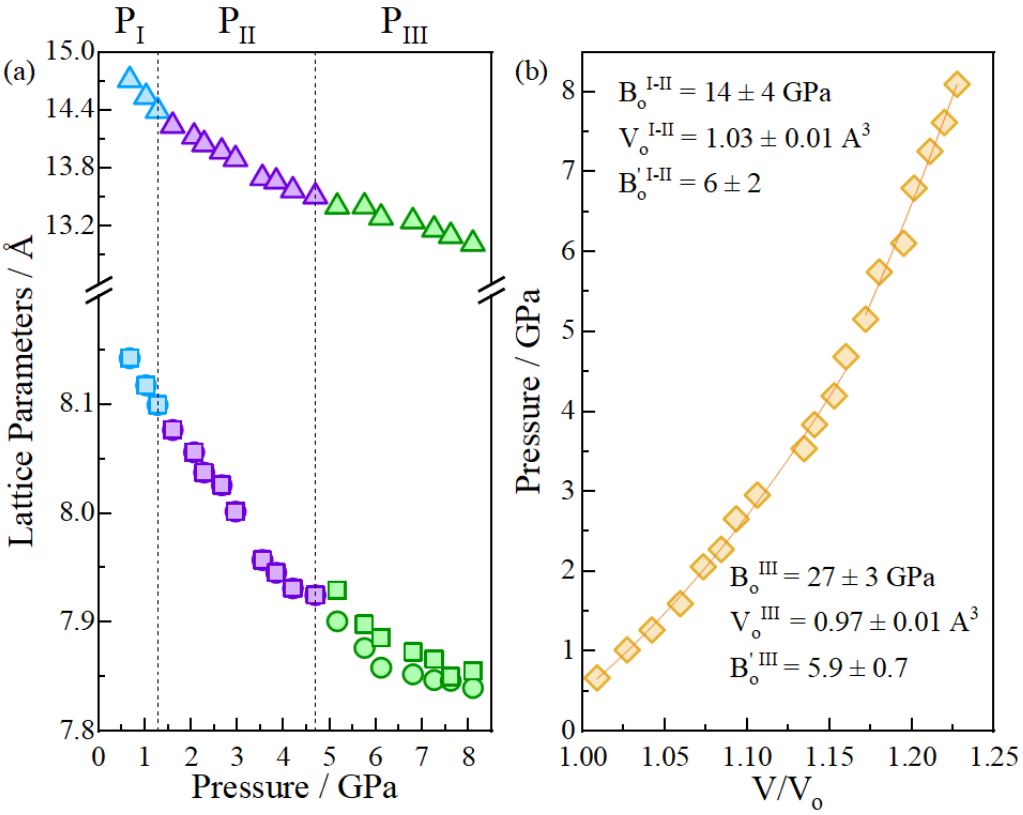

Source: Elaborated by the author.

Figure 19a illustrates the anisotropic compression observed throughout the process, with the *c* parameter exhibiting the highest compressibility compared to the *a* and *b* parameters. At

room conditions, the *a* and *b* parameters show similar values, but as pressure increases, the difference in their compression ratios gradually becomes more pronounced, particularly evident until reaching the P_{III} phase. Continuous contraction of the cell parameters *a* and *b* are maintained during the P_I and P_{II} phases. While the pressure-induced structural phase transitions in $CsPb_2Cl_5$ have been successfully characterized through diffractograms and lattice parameters, it is crucial to consider the resulting relative shift, which can generate uniaxial stress due to the compound's elastic anisotropy. Such stress can be predicted using the Equation of State (EOS) (Birch, 1947; Goodwin, Keen e Tucker, 2008; Sata *et al.*, 2002). In this context, the experimental $P = (V_0/V)$ V(P) data presented in Figure 19b were fitted using the third-order Birch-Murnaghan equation of state:

$$P = \frac{3}{2}B_0\left[\left(\frac{V_0}{V}\right)^{\frac{7}{3}} - \left(\frac{V_0}{V}\right)^{\frac{5}{3}}\right]\left[1 + \frac{3}{4}(B' - 4)\left\{\left(\frac{V_0}{V}\right)^{\frac{2}{3}} - 1\right\}\right] \quad (6)$$

Here, the equation is expressed in terms of the volume at zero pressure (V_0), the bulk modulus ($B_0 = (-V\partial P/\partial V)_T$), and the dimensionless pressure derivative ($B' = (\partial B/\partial P)_T$), which describes the variation of B_0 with pressure (Katsura and Tange, 2019). The isothermal bulk modulus for the tetragonal base P_I-P_{II} of $CsPb_2Cl_5$ was estimated to be $B_0 = 14\ (4)$ GPa and it is derivative $B' = 6\ (2)$. Similarly, for the P_{III} phase, the values were determined as $B_0 = 27\ (3)$ GPa and $B' = 6\ (1)$. The observed change of *I*4/*mcm*→*I*4/*m*→*C2* was associated with an increased unit-cell volume, consistent with the expected behavior of high-pressure phases characterized by higher bulk moduli, reflecting their denser and less compressible crystal structures. In hybrid and inorganic materials based on metal halide perovskites, the B_0 values typically range from 10 to 70 GPa (Agbaoye, Adebambo e Adebayo, 2019; Chaves *et al.*, 2014; Tu *et al.*, 2021). The low bulk modulus of metal halide perovskites is believed to contribute to their unique properties, such as self-healing, ion migration, and low thermal conductivity, making them suitable for applications in the flexible electronics industry due to their ductility (Rakita *et al.*, 2015; Sun *et al.*, 2015), and the observed value of B' indicates a slow stiffening of the material.

The bulk modulus of $CsPb_2Cl_5$ can be compared with various Cs-Pb-Br perovskites and perovskites-like compounds, including $CsPb_2Br_5$ ($B_0 = 11.5\ (3)$ GPa, $B' = 9.3\ (6)$) (Drushliak e Szafrański, 2022b), and the perovskite polymorphs of $CsPbBr_3$ (*Pbnm:* $B_0 =$

15.0 (8) GPa, $B' = 6.0\ (18)$) (Szafrański, Katrusiak e Ståhl, 2021), (*Pnma:* $B_0 = 18.847$ GPa), (*I*4/*mcm:* $B_0 = 19.02$ GPa), (*Cmcm:* $B_0 = 20.65$ GPa), as well as the non-perovskite $CsPbBr_3$ (*Pnma:* $B_0 = 20.37$ GPa) (Schryver e Lamichhane, 2023). The results reveal good agreement among these compounds, indicating similar structural behavior under pressure. Notably, this characteristic is also shared with 3D organic-inorganic metal halide perovskites. For instance, $CH_3NH_3SnI_3$ has a bulk modulus of $B_0 = 12.6\ (7)$ GPa, $HC(NH_2)_2SnI_3$ has $B_0 = 8.0\ (7)$ GPa, and $HC(NH_2)_2PbI_3$ has $B_0 = 11.0\ (2)$ GPa (Lee *et al.*, 2003; Liu *et al.*, 2017). Furthermore, the high value of the pressure derivative of the bulk modulus, B' ($B' > 4$), observed in $CsPb_2Cl_5$, can be attributed to its layered crystal structure. Comparable values have been reported for graphite ($B' = 8.0\ (6)$) (Solozhenko *et al.*, 2006) and layered $GeSe_2$ ($B' = 9.1\ (22)$) (Stølen *et al.*, 2000), emphasizing the influence of the layered nature of the crystal structure on the mechanical response to pressure.

4.2 Influence of the Pb-Cl bonds P_I and P_{II} phases

Therefore, gaining further insights into the physical mechanisms underlying the P_I to P_{II} transition in $CsPb_2Cl_5$ is essential. To elucidate the structural changes accompanying the pressure-induced phase transitions, a comprehensive investigation of the Pb-Cl bond lengths (l_1 and l_2) and the Cl-Pb-Cl bond angles (θ_1 and θ_2) within the $PbCl_8$ polyhedral motif is carried out, as illustrated in Figure 20 a–d. Therein, the parameters l_1 and θ_1 represent the top view Pb-Cl bond lengths and Cl-Pb-Cl bond angles within the inorganic layers, respectively, while l_2 and θ_2 correspond to the side view of the Pb-Cl bond lengths and Cl-Pb-Cl bond angles.

The analysis reveals that l_1 undergoes a progressive contraction, and θ_1 gradually narrows as the sample is compressed, resulting in a successive decrease in both parameters until reaching the critical pressure $P_c^{I\text{-}II} = 1.27$ GPa. At this point, a shift is observed in both the θ_1 and l_1. On the other hand, l_2 exhibits a linear reduction at relatively low pressures as compression progresses towards $P_c^{I\text{-}II}$. However, beyond this critical point, l_2 undergoes a successive increase with increasing pressure, leading to elongation. Notably, the inflection point of the bond length l_2 coincides with the pressure-induced structural phase transition from P_I to P_{II}. Furthermore, the bond angle θ_2 demonstrates a widening dependence on pressure. To quantitatively assess the distortion of the $PbCl_8$ polyhedra, the distortion parameter (Δd) based on the Pb-Cl bond lengths is employed using the following expression:

$$\Delta d = \left(\frac{1}{8}\right)\sum\left[\frac{d_n - d}{d}\right]^2 \quad (7)$$

where d is the mean Pb-Cl distance and d_n are the eight individual Pb-Cl (García-Fernández *et al.*, 2018; Katan *et al.*, 2015; Lufaso e Woodward, 2004).

Figure 20 – (a) – (d) Refined Pb–Cl bond lengths and Cl–Pb–Cl bond angles (l_1, l_2, θ_1 and θ_2) with increasing pressure. (e) – (f) Schematic diagram of the Pb–Cl bonds and Cl–Pb–Cl angles within the Pb–Cl layers for tetragonal $CsPb_2Cl_5$. (g) Schematic illustrations of the Pb–Cl bond lengths and Cl–Pb–Cl bond angles.

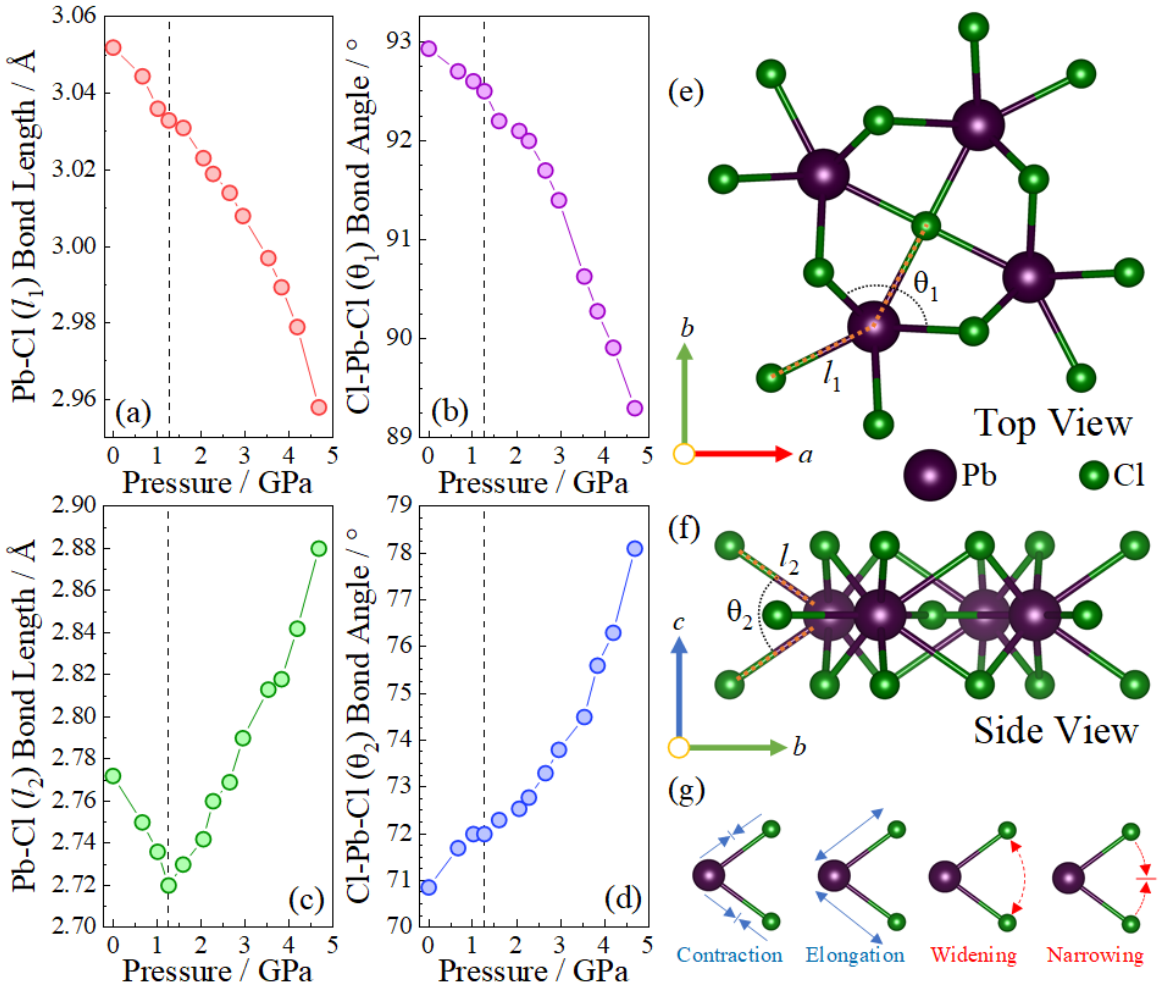

Source: Elaborated by the author.

The obtained values indicate that both Pb-Cl bond lengths contribute significantly to the distortion, with l_2 being the predominant factor. The pressure dependence of Δd, as depicted in Figure 21, highlights the crucial role played by the variations in l_2 and θ_2 under pressure in

driving the observed structural phase transitions. These changes in the Pb-Cl network structure induced by compression have a direct impact on the electronic configuration, thereby influencing the photoelectric properties of the material, as the related compound $CsPbCl_3$, which exhibits intriguing phenomena, such as the disappearance of photoluminescence or an unexpected increase in the band gap during the proper structural phase transition (SZAFRAŃSKI; KATRUSIAK; STÅHL, 2021; ZHANG et al., 2018).

Figure 21 – (a) Distortion (Δd) pressure-dependence of the $PbCl_8$ polyhedra, with (b) – (c) the P_I and P_{II} layers, respectively.

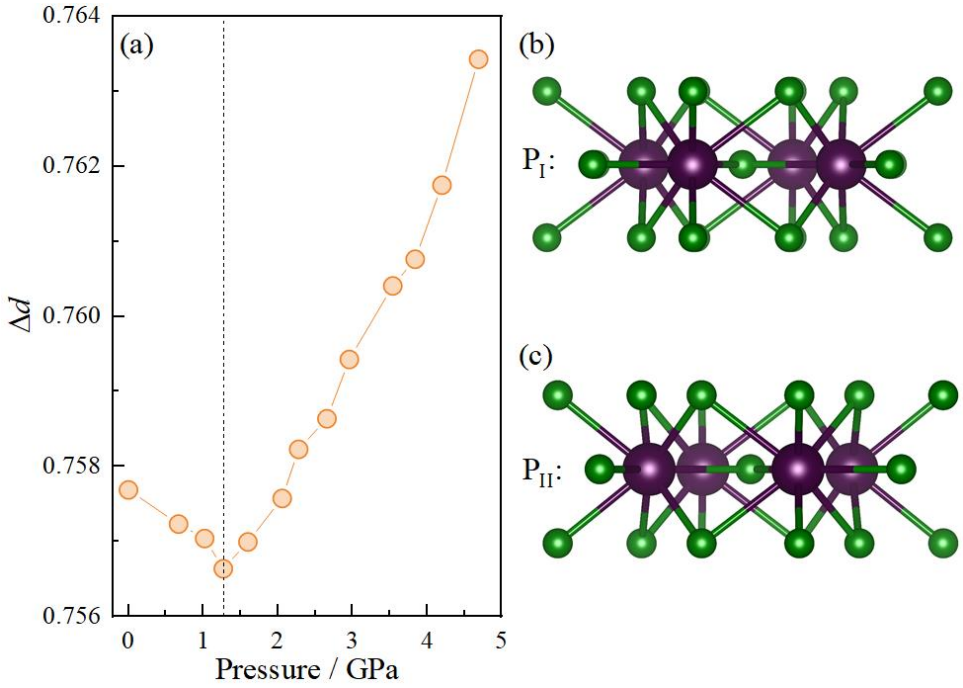

Source: Elaborated by the author.

4.3 High-pressure Raman Spectroscopy

Since the Raman spectra under extreme conditions are highly sensitive to the crystalline structure, it is imperative to investigate the vibrational properties of $CsPb_2Cl_5$. The Raman spectroscopy was conducted on $CsPb_2Cl_5$ at room temperature, employing increasing hydrostatic pressure to validate the structural phase transition. The group theory analysis (Kroumova *et al.*, 2003; Rousseau, Bauman e Porto, 1981a) predicts that the compounds exhibit 13 vibrations modes in the P_I (*I*4/*mcm*), 21 vibrations in P_{II} (*I*4/*m*), and 45 vibrations in P_{III} (*C*2). The Raman-active mode distributions are represented as $\Gamma_{raman}^{I}=3A_{1g}\oplus 2B_{1g}\oplus 3B_{2g}\oplus 5E_g$

$\Gamma_{raman}^{II}=6A_g\oplus5B_g\oplus10E_g$ and $\Gamma_{raman}^{III}=21A\oplus24B$ for the point group P_I: D_{4h} (4/*mmm*), P_{II}: C_{4h} (4/*m*), and P_{III}: C_2 (2), respectively.

Figure 22 – High-resolution Raman spectrum of $CsPb_2Cl_5$ at the pressure-induced P_I, P_{II} and P_{III}. The continuous blue, purple and green lines represent the convolution of Lorentzian line profiles (black lines) for each phase, which best fit the experimental data (black dots).

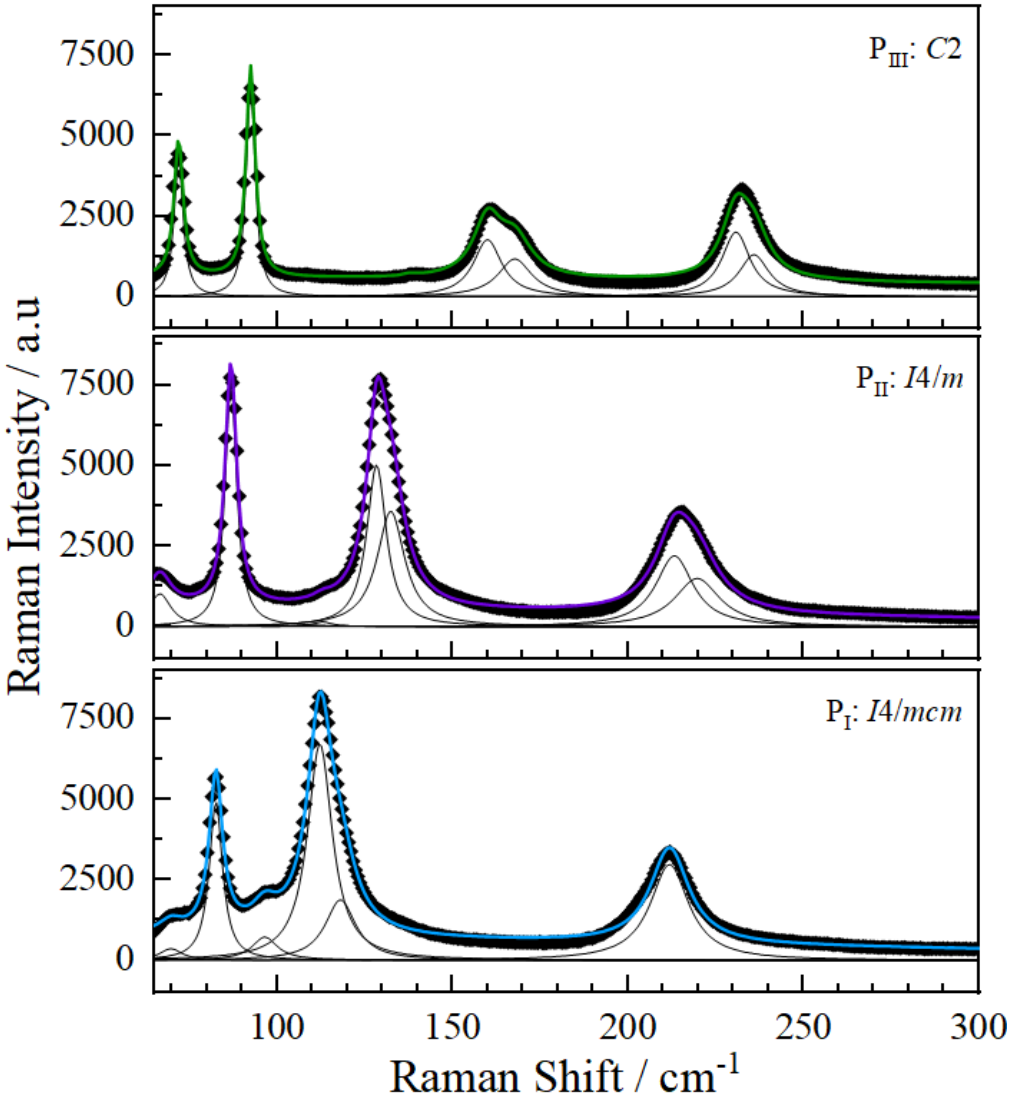

Source: Elaborated by the author.

Figure 22 displays selected Raman spectra of $CsPb_2Cl_5$ in the 65-300 cm^{-1} range for each pressure-induced phase on $CsPb_2Cl_5$. At room conditions, six distinct Raman vibrational modes were observed. Through comparisons with previous Raman studies on metal-halide perovskite materials (ZHANG et al., 2018; ZHANG; ZENG; WANG, 2017) and the $CsPb_2Br_5$

(Hadjiev et al., 2018), the phonon assignments were established. The displayed Raman bands predominantly arise from vibrations of the Pb-Cl bonds. The low-frequency ($\omega < 70$ cm^{-1}) vibrations correspond to the top-view layer visualization and involve the phonons associated with the l_1 length. On the other hand, vibrations with $\omega > 70$ cm^{-1} are attributed to the l_2 bond vibrations. In Figure 22, the side-view vibrations in the P_{II} and P_{III} phases exhibit increased displayed bands, indicating a crystal structure modification. This observation validates the crucial role of the l_2 length on the structural phase transition mechanisms in the $CsPb_2Cl_5$ related to the $PbCl_8$ polyhedra continuous distortion, even though the layers are well preserved as was observed in synchrotron powder X-ray diffraction (SPXRD) results.

To gain further insights into the pressure-induced modifications, a comprehensive Raman spectrum as a function of pressure is presented in Figure 23a, revealing notable redshifts in all vibrational modes. Remarkably, the pressure-induced Raman spectrum exhibits the same profile as the P_I phase from room pressure up to 1.24 GPa, providing strong evidence for the reorganization and progressive contraction of the $PbCl_8$ polyhedra. However, a sudden shift in the frequency pressure-dependence is observed beyond this point, emphasizing the distinct nature of the subsequent phase transitions. Consistent with the SPXRD findings, a significant change in the l_2 vibration becomes evident in the pressure-dependent Raman spectra at 1.54 GPa. This transition coincides with a new Raman active band at $\omega = 230$ cm^{-1} in the P_{II} phase. Intriguingly, all phonons persist until encountering a discontinuity at the threshold of the P_{III} phase, suggesting the structural phase transition in the crystal structure. These findings are clearly illustrated in Figure 23b, which provides a comprehensive visualization of the evolving vibrational modes under increasing pressure and underscores the intricate interplay between pressure and crystal symmetry. Another notable feature observed in the Raman spectra is the sudden and significant increase in the phonon intensity at $\omega = 60$ cm^{-1} in P_{II}. This pronounced change suggests that the aggravated pressure-induced distortion of the $PbCl_8$ polyhedra primarily drives the modification in the Pb-Cl network structure.

Figure 23 – (a) Pressure-induced Raman spectra of $CsPb_2Cl_5$. (b) Phonon energy as a function of the hydrostatic pressure. Vertical dashed lines represent the phase transitions identified by SPXRD.

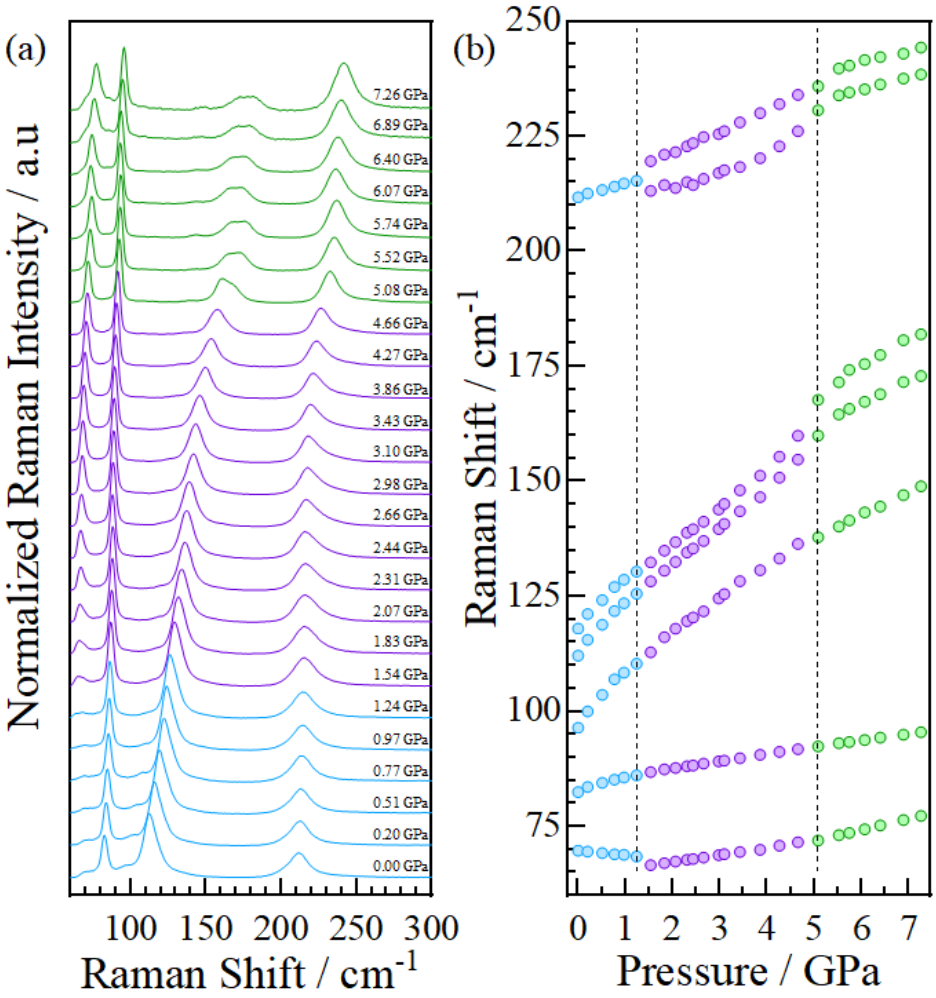

Source: Elaborated by the author.

In conclusion, the structural phase transition of $CsPb_2Cl_5$ under pressure has been systematically investigated utilizing synchrotron powder X-ray diffraction (SPXRD) and Raman spectroscopy techniques. The obtained results shed light on the complex phase evolution of the compound. It was observed that $CsPb_2Cl_5$ undergoes a structural transition from phase P_I with space group I4/mcm to phase P_{II} with space group I4/m at a pressure of 1.60 GPa, and subsequently transforms to phase P_{III} with space group C2 at 5.16 GPa. To gain further insights into the structural changes, a comprehensive analysis was conducted on the Pb-Cl bond lengths (l_1 and l_2) and the Cl-Pb-Cl bond angles (θ_1 and θ_2) within the $PbCl_8$ polyhedral motif.

The obtained values highlight the significant contributions of both Pb-Cl bond lengths, with l_2 being the predominant factor in the distortion of the structure.

Additionally, bulk modulus calculations were performed for each phase, resulting in values of Bo^{I-II} = 14 ± 4 GPa and Bo^{III} = 27 ± 3 GPa. These findings suggest that $CsPb_2Cl_5$ exhibits a certain degree of structural softness, rendering it suitable for applications in the flexible electronics industry. Moreover, Raman measurements further validate the crucial role played by the l_2 bond length in the structural phase transition mechanisms of $CsPb_2Cl_5$, specifically about the continuous distortion of the $PbCl_8$ polyhedra. Remarkably, the layers within the compound remain well-preserved, as observed in the SPXRD results. The comprehensive understanding gained from this study enhances the knowledge of the structural properties and phase transitions of $CsPb_2Cl_5$ under pressure.

5 Iodide Doping and its Impact on 2D $CsPb_2X_5$ (X = Br, I) Perovskite-like Properties

Over the past decade, perovskite solar cells (PSCs) have received considerable attention from researchers due to their remarkable increase in power conversion efficiency (PCE), approaching that of conventional inorganic semiconductors. Among them, lead halide PSCs have emerged as strong contenders against commercially available silicon-based solar cells owing to their low-cost solution process photovoltaic technology (Bati *et al.*, 2023; Wang, Y. P. *et al.*, 2023).

Metal halide perovskites exhibit various physical properties due to structural and compositional modifications (Gao *et al.*, 2019; Yan *et al.*, 2023). Thus, further investigation into the underlying mechanisms and anion exchange phenomena is crucial to understand these materials comprehensively. Octahedral tilting and anion exchange are key mechanisms that play pivotal roles in controlling the phase and composition of perovskite structure (Shi *et al.*, 2017).

Anion exchange involves halide ions' partial or complete substitution within the perovskite structure. The flexibility of the lattice and the presence of vacancies allow for anion switching during or after synthesis using a variety of halide precursors or mixtures of other anion species. The concentration of halide ions influences the diffusion of ions into the crystal lattice, thus significantly impacting the bandgaps, primarily determined by the anion composition and valence. As a result, anion exchange exhibits diverse effects on perovskites' structural, physical, and optical properties. Moreover, it offers the capability to modify or shift the photoluminescence (PL) emission across the visible spectrum, providing tunability and versatility in the optical properties of these materials (Bella *et al.*, 2016; Protesescu *et al.*, 2015c). Proper control and implementation of anion exchange have demonstrated the potential to effectively modify the structures and properties of metal halide perovskites, opening up opportunities for tailoring their characteristics to specific applications (Schmidt-Mende *et al.*, 2021). A comprehensive understanding of anion exchange phenomena will pave the way for developing advanced perovskite-based devices with enhanced performance and functionality.

Within the realm of metal halide perovskites, the two-dimensional (2D) perovskite-like $CsPb_2Br_5$ compound, derived from $CsPbBr_3$, has gained significant interest for its promising applications in photodetectors and solar cells. It exhibits advantages such as utilizing low-cost raw elements and possessing high-quality optoelectronic properties (Chen, Chen, e Huang,

2023). To enhance its anion exchange properties, a comprehensive investigation of the low-dimensional tetragonal $CsPb_2(Br_{1-x}I_x)_5$ family has been conducted to explore and expand its potential for various applications. Several characterization techniques, including Single Crystal X-Ray Diffraction (SCXRD), Raman spectroscopy, and Photoluminescence (PL), have been employed to understand and characterize the properties of these compounds. The SCXRD and Raman spectroscopy analyses have provided detailed information on the crystal structure of the materials, enabling the elucidation of the effects of I^- halide substitution on the lattice parameters. A significant focus has been placed on the photoluminescence properties of the $CsPb_2(Br_{1-x}I_x)_5$ compounds. Intriguing changes in the PL characteristics have been observed by systematically varying the composition through halide substitution. Specifically, an increase in PL intensity accompanied by a decrease in energy emission has been observed, highlighting the tunability of the compounds across the entire visible spectrum. This tunability makes them highly attractive for applications where precise control over the emission wavelength is crucial.

5.1 Influence of the iodide in the crystal structure

The results of SCXRD structure determination on all iodine-substituted compounds reveal they are isostructural to the $CsPb_2X_5$ (X= Cl, Br) family (Dursun *et al.*, 2017; Li, J. *et al.*, 2017b; Yin, Zhang e Tao, 2019). The $CsPb_2(Br,I)_5$ solid solution has a body-centered tetragonal structure with I4/mcm symmetry at room temperature. Table 7 summarizes the crystallographic data and principal parameters of selected determined crystal structures. In Figure 24a, the $CsPb_2(Br,I)_5$ crystal structure is illustrated and depicted, showcasing both the top and side views of the Pb-X layers. These compounds can be effectively described by a conventional two-dimensional framework, where Cs^+ ions reside between the planes of Pb-X polyhedra. The lead atoms coordinate with seven halogen atoms, forming a PbX_8 (X = Br or Br/I). These polyhedra are connected through edges, giving rise to sheets parallel to the crystal's ab plane. There are two non-equivalent halide anions: X_1 (4*c* site), located on a plane half-height of the sheet and shared by four polyhedra, and X_2 (16*l* site), defining the top and bottom planes of the sheet. SEM and EDX analysis was conducted to explore the morphological characteristics and spatial distribution of I^- cations on the surface of a $CsPb_2(Br,I)_5$ single crystal. Figure 24b displays the SEM image, providing the crystal morphology. The accompanying EDX images (Figure 24c) display a consistent and uniform distribution of I- cations across the crystal surface. The intensity of the I^- signal remains constant throughout, indicating a high degree of homogeneity within the synthesized crystals.

Table 7 – Crystal data and refinement parameters of selected members of the $CsPb_2(Br_{1-x}I_x)_5$ family at room-temperature conditions

Empirical formula	$CsPb_2Br_5$	$CsPb_2(Br_{0.88}I_{0.12})_5$	$CsPb_2(Br_{0.78}I_{0.22})_5$	$CsPb_2(Br_{0.66}I_{0.34})_5$
Formula weight (g/mol^{-1})	946.84	975.97	997.00	1024.61
Crystal system	Tetragonal			
Space group	*I*4/*mcm*			
Unit cell Dimensions	*a*=8.4952 (5) Å *b*=8.4952 (5) Å *c*=15.1959 (12) Å	*a*=8.5291 (8) Å *b*=8.5291 (8) Å *c*=15.3428 (19) Å	*a*=8.625 (5) Å *b*= 8.625 (5) Å *c*=15.519 (13) Å	*a*=8.705 (4) Å *b*= 8.705 (4) Å *c*=15.664 (6) Å
Volume ($Å^3$)	1096.66 (16)	1116.1 (3)	1154.5 (15)	1186.9 (12)
Density (Mg/m^3)	5.735	5.808	5.736	5.734
μ (mm^{-1})	52.078	50.666	48.631	46.852
F (000)	1576	1621	1653	1695
Radiation type	Mo *Kα*			
Z	4			
Crystal shape	Block			
Absorption correction	Multi-scan			
R factor (all data)	R_1 =0.0754 wR_2=0.1737	R_1=0.0339 wR_2=0.0886	R_1=0.0320 wR_2=0.0619	R_1=0.0320 wR_2=0.0692
GooF=*S*	1.035	1.092	1.203	1.093

Source: Elaborated by the author.

An interesting characteristic of $CsPb_2(Br,I)_5$ compounds is the preference of iodine to occupy the larger cage, leading to a substitution that exclusively occurs at the X_2 sites. Notably, regardless of the iodine content, when iodine was allowed to occupy X_1 sites, the refinement of the crystalline structure became unstable. This behavior is quite distinct from the $CsPb_2(Br_{1-x}Cl_x)_5$ system (Chen, Y. *et al.*, 2018c), where the larger anion (Br) occupies both X sites of the layers, with a preference but not exclusivity for the X_2 sites. Based on this atomic distribution, the stoichiometry of the $CsPb_2(Br,I)_5$ solid solution could be better described as $CsPb_2Br(Br_{1-y}I_y)_4$, but to keep a consistent notation with previous reports, the iodine concentration will be denoted relative to the overall bromine content as $CsPb_2(Br_{1-x}I_x)_5$.

Figure 24 – (a) Room temperature body-centered tetragonal crystal structure of the low-dimensional $CsPb_2(Br,I)_5$ solid solution, and the top and side views of the polyhedra layers (b) SEM image and (c) EDX image of the compound.

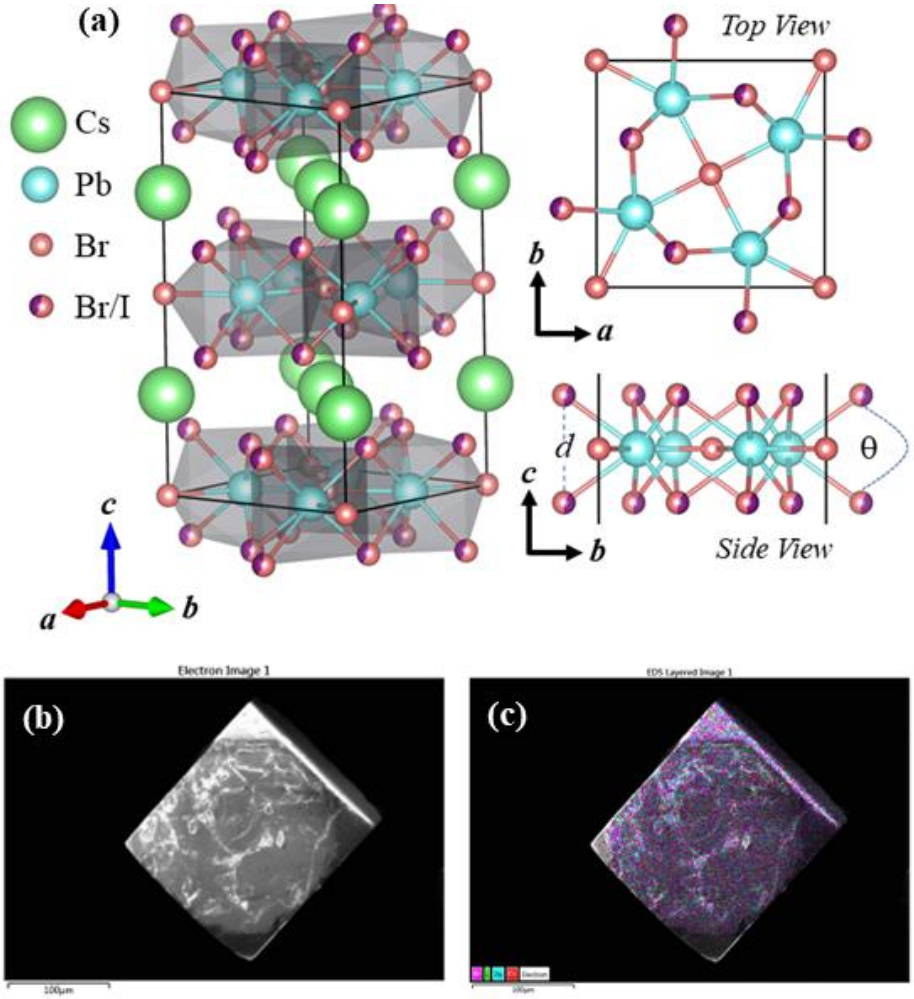

Source: Elaborated by the author.

The most noticeable effect of iodine substitution is the consistent expansion of the lattice parameters and volume, as depicted in Figure 25 and summarized in Table 7 for selected structures. The lattice parameters of the unsubstituted compound agree very well with those reported by other authors (Chen Y. *et al.*, 2018c; Dursun *et al.*, 2017; Maity e Pradhan, 2020). The changes in these parameters attributed to the varying iodine content observed within the investigated concentration range can be effectively described by Vegard's law of linear proportionality, which is also observed in $CsPbBr_3$ when substituted with both chlorine and iodine (Chen *et al.*, 2018) synthesized the $CsPb_2(Cl_{1-x}Br_x)_5$ system, which demonstrates a

monotonic increase in the lattice parameters as the concentration of the larger anion increases. However, linear proportionality is not observed unlike the previously described solid solutions. Moreover, unlike the Br/Cl system, the complete solubility range cannot be achieved in the Br/I solid solution. The fully substituted $CsPb_2I_5$ compound does not crystallize under ambient conditions and has only been recently synthesized using high-pressure and high-temperature techniques (Li *et al.*, 2022b). Figure 25 and Table 7 included its corresponding lattice parameters for comparison purposes. As expected, the lattice parameters are larger than those of $CsPb_2Br_5$, but they do not follow the trend established by the low substitution side of the phase diagram (Figure 25). It has been proposed that these differences in lattice parameters could be related to the stress induced by the synthesis method (Li *et al.*, 2022b). However, it is worth noting that the same methodology was used to produce $CsPb_2Br_5$, whose lattice parameters do not differ considerably from crystals obtained by the conventional slow evaporation strategy. Therefore, it is more likely that the anomalous behavior of $CsPb_2I_5$ is due to its metastable nature, which can only be produced under extreme conditions.

The expansion of the lattice parameters in $CsPb_2(Br,I)_5$ can be attributed to the increase in bond lengths, which follow the same linear behavior observed in Figure 25. This relationship is further exemplified by the Pb-X distances presented in Figure 26a. The larger ionic radii of iodine anions in the Pb-Br_2/I bond elucidates this expansion phenomenon. However, even in the absence of substitution and while residing on the same plane as Pb, the distances associated with Br_1 experience an expansion due to the higher iodine content. Notably, the bond lengths of $CsPb_2I_5$ do not follow the linear trend defined by the low iodine content region, a characteristic that can be attributed to its previously discussed metastable nature.

Figure 25 – Unit cell lattice parameters and volume of the $CsPb_2(Br,I)_5$ solid solution. Data corresponding to $CsPb_2I_5$ was extracted from reference (Li et al., 2022b).

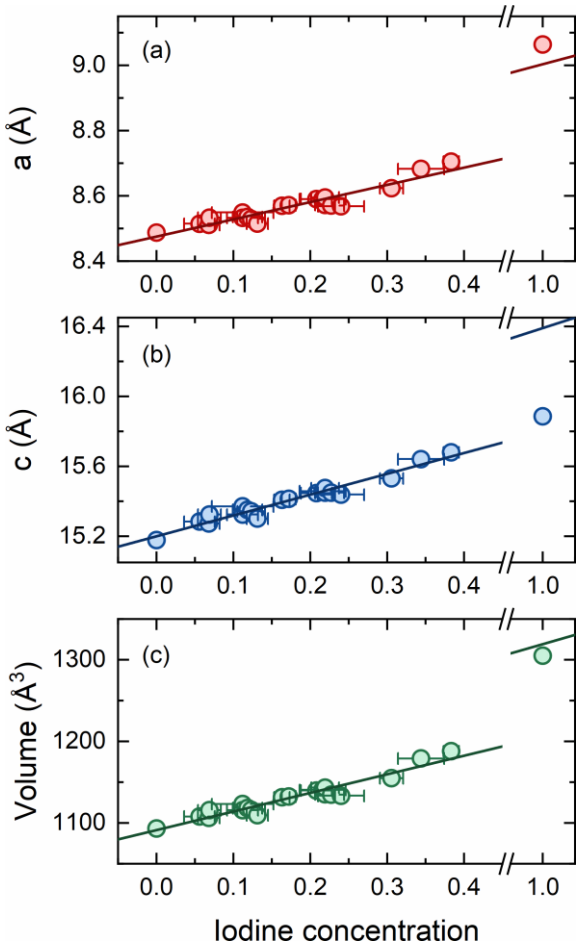

Source: Elaborated by the author.

The optoelectronic properties of $CsPb_2(Br,I)_5$ compounds result from the exciton dynamics within the 2D-planar $[PbX_8]^{6-}$ layers, making it essential to consider their structural characteristics. Figures 26b and 26c illustrate the layer distortion (θ) and height (d), respectively, with their definitions provided in Figure 24a. Due to the difference in the ionic radii of the halogens, the $[PbX_8]^{6-}$ polyhedron and, consequently, the layers expand with increasing iodine content, resulting in a linear trend for layer height.

However, none of the previous parameters provide evidence suggesting a limit on the solubility range of the $CsPb_2(Br,I)_5$ phase diagram. The observed layer distortion can be attributed to the X-Pb-X bond angles shown in Figure 26b. Notably, the angles involving the Br_1 anion appear nearly unaffected by iodine substitution. On the other hand, the X_2-Pb-X_2

angles, which are directly related to the layer height, exhibit a linear trend up to x ~ 0.3, but saturate beyond this value, defining an upper limit for this magnitude. It is worth highlighting that the X_2 sites define the eight nearest vertices of the CsX_{10} coordination polyhedron, and the expansion of the layers may be constrained by steric repulsion between these groups and the interlayer cesium cations. This limitation suggests a potential mechanism for controlling the layer height and maintaining structural stability within a specific range of iodine substitution.

Figure 26 – Selected (a) bond distances and (b) bond angles of the compounds in the $CsPb_2(Br,I)_5$ solid solution. (c) Height of the $[PbX_8]^{6-}$ layers. Data corresponding to $CsPb_2I_5$ were extracted from ref. (Li et al., 2022b).

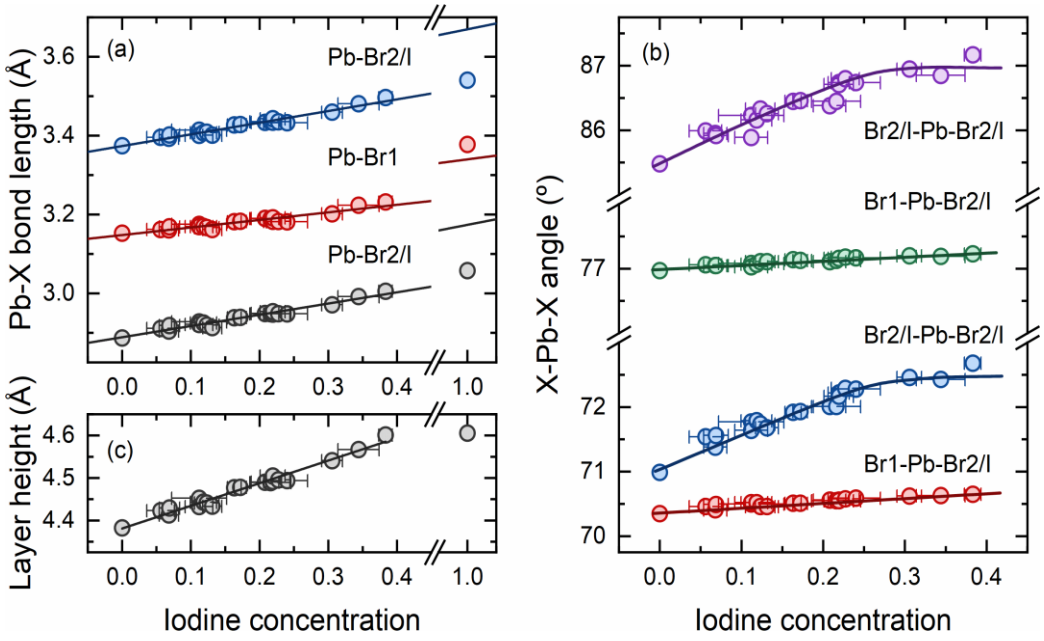

Source: Elaborated by the author.

The bond valence (BV) method can be used to estimate the strength of chemical bonds in a crystal lattice and to determine the valence states of the elements (Brown e Altermatt, 1985). It is often used to validate crystal structures (Brown, 2009). However, the conventional parameters used in the BV method tend to overestimate the length of Pb-X bonds and underestimate those of A-X bonds (Linaburg *et al.*, 2017). To address this, the parameters set of Pb-X parameters were calculated based on the gas phase bond length (Sheng-Zhi, 2007), and the Cs-X parameters were determined by considering second neighbors (Adams, 2001). This

parametrization provides reliable valences for unsubstituted $CsPb_2Br_5$ (Pb: 2.04 and Cs: 1.06) and $CsPb_2Cl_5$ (Pb: 2.01 and Cs: 1.02).

In order to analyze the solid solutions, the bond valence sums (BVS) were calculated using a weighted average approach, where each site's anion occupation was considered the weighting factor. To illustrate this methodology, let us consider the case of Pb. The bond valence sum for Pb was calculated using two non-substituted BV with Br_1 (3.1529(8) Å for x=0) and four substituted Br_2 sites, using two short BV (2.8870(9) Å for x=0) and four long BV (3.3746(10) Å for x=0) were employed. The BVS as a function of the iodine concentration are shown in Figure 27. Additionally, to facilitate comparison, the valences determined from the structural data of the $CsPb_2(Cl_{1-x}Br_x)_5$ system (Chen, Y. *et al.*, 2018c) are also presented in this figure. As chlorine replaces both anion sites, its contribution to the BVSs was accounted for appropriately.

The calculated valence sums of the cations in the chlorine region of Figure 27 closely match the nominal values, which agrees with the full solubility observed for the Cl/Br solid solution. Consequently, the Pb BVS remains constant within the expected valence state within the chlorine-substituted region and for iodine concentrations up to about 0.3. Beyond this value, Pb BVS reduces until reaching the upper limit of the solid solution. The Cs BVS has a slightly different substitution dependence, remaining close to the nominal value in the chlorine-rich region and increasing slightly up to 1.18 at x~0.3 due to the iodine substitution. Above this value, it remains constant until reaching the maximum observed concentration.

Regarding the anions, it is interesting to notice that at the X_2 sites, the BVS does not depart considerably from the nominal value within the whole range of concentrations. On the other hand, the X_1 BVS constantly increases as the Br anion is substituted, reaching the nominal value at the limit of the miscibility region. Also, the global instability index (GII) does not depart from the stability region. These findings suggest that the cations are favorably bonded for all the chlorine concentrations and up to x~0.3 in the case of iodine substitution, suggesting that instabilities increase beyond this value. As the limit value of the iodine substitution (x~0.5) is reached, the structure becomes non-viable, and it is impossible to obtain $CsPb_2X_5$ with higher iodine substitutions.

Figure 27 – (a) Lead, (b) cesium, and (c) anion calculated bond valences sum and (d) global instability index (GII) as a function of the iodine and chlorine content. Data corresponding to $CsPb_2Cl_5$ and $CsPb_2I_5$ were extracted from ref. (Chen, Y. et al., 2018c) and (Li et al., 2022b), respectively.

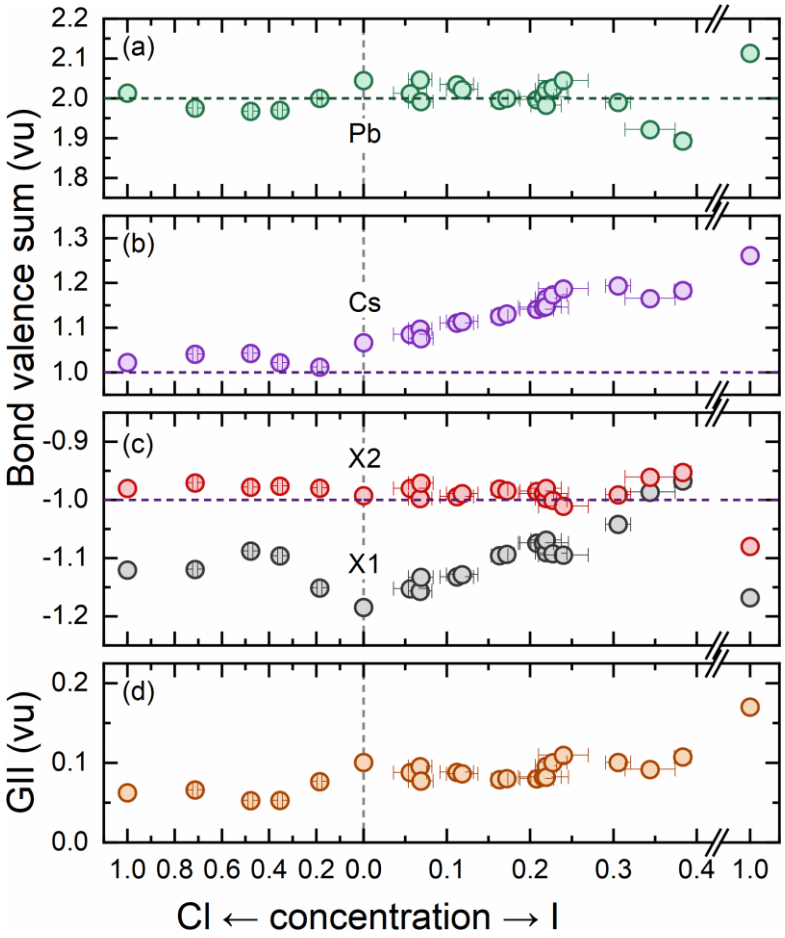

Source: Elaborated by the author.

5.2 Insights into the Effect of Iodide Incorporation on Raman Spectroscopy

Since all the investigated compounds have the same crystalline structure, group theory analysis based on the $CsPb_2X_5$ structure can predict the number of vibrational modes. The analysis was conducted using the body-centered tetragonal system with I4/mcm symmetry, and the distribution of the phonons and mode classifications are summarized in Table 8. At the Γ-point of the Brillouin zone, 13 Raman-active modes are predicted (Rousseau, Bauman e Porto, 1981), which are distributed according to the irreducible representation of the D_{4h} point group as $\Gamma_{Raman} = 3A_{1g} \oplus 2B_{1g} \oplus 3B_{2g} \oplus 5E_g$. However, due to the layered PbX_8 polyhedra crystal habit of the samples, along with the [001] direction, the Raman selection rules of the D_{4h} point group,

vibrational modes with E_g symmetry are not expected to be observable, even under non-polarized scattering geometries. Figure 28 shows that all Raman-active modes were identified in the room-temperature Raman spectra of $CsPb_2(Br,I)_5$. The symmetry of the observed bands was classified based on the polarized Raman results, confirmed by DFPT calculations reported by (Hadjiev et al., 2018) on $CsPb_2Br_5$.

Additionally, the vibrational modes involving Br_1 atoms do not contribute to the Raman spectrum. As seen in Figure 28, all the Raman-active modes were identified in the Raman spectra of $CsPb_2(Br,I)_5$ at room temperature. The symmetry of the observed bands was classified based on the polarized Raman result reported by (Hadjiev et al., 2018) and confirmed by DFPT calculations on $CsPb_2Br_5$.

Table 8 – Distribution of vibrational modes based on the group theory for the $CsPb_2(Br,I)_5$ solid solution.

Atoms	Wyckoff notation	Site symmetry	Irreducible representations
Pb	8h	C'_{2v}	$A_{1g}\oplus A_{2g}\oplus A_{2u}\oplus B_{1g}\oplus B_{2g}\oplus B_{1u}\oplus E_g\oplus 2E_u$
Cs	4a	D_4	$A_{2g}\oplus A_{2u}\oplus E_g\oplus E_u$
Br_1	4c	C_{4h}	$A_{1u}\oplus A_{2u}\oplus 2E_u$
Br_2/I	16l	C_s^d	$2A_{1g}\oplus A_{2g}\oplus A_{1u}\oplus 2A_{2u}\oplus B_{1g}\oplus 2B_{2g}\oplus 2B_{1u}\oplus B_{2u}\oplus 3E_g\oplus 3E_u$
	Total		$3A_{1g}\oplus 3A_{2g}\oplus 2A_{1u}\oplus 5A_{2u}\oplus 2B_{1g}\oplus 3B_{2g}\oplus 3B_{1u}\oplus B_{2u}\oplus 5E_g\oplus 8E_u$
Mode Classification			
$\Gamma_{acoustic} = A_{2u}\oplus E_u$			
$\Gamma_{optic} = 3A_{1g}\oplus 3A_{2g}\oplus 2A_{1u}\oplus 4A_{2u}\oplus 2B_{1g}\oplus 3B_{2g}\oplus 3B_{1u}\oplus B_{2u}\oplus 5E_g\oplus 7E_u$			
$\Gamma_{IR} = 4A_{2u}\oplus 7E_u$			
$\Gamma_{Raman} = 3A_{1g}\oplus 2B_{1g}\oplus 3B_{2g}\oplus 5E_g$			
$\Gamma_{silent} = 2A_{1u}\oplus 3B_{1u}\oplus B_{2u}$			

Source: Elaborated by the author.

The Raman spectra obtained from $CsPb_2(Br,I)_5$ single crystals exhibit a notable shift of most bands towards lower wavenumbers with increasing iodine substitution. This observed phenomenon can be attributed to the softening of vibrational modes caused by increased Pb-X bond distances and the corresponding changes in the effective mass at the Br_2/I sites. These conclusions are supported by the structural characterization results obtained through SCXRD. The shift towards lower wavenumbers in the Raman spectra indicates a reduction in the vibrational stiffness and increased vibrational amplitude within the crystal lattice upon iodine

substitution. The elongation of the Pb-X bonds, arising from the larger ionic radius of iodine compared to bromine, leads to weaker bonding interactions and, consequently, a decrease in the force constants of the relevant vibrational modes. Furthermore, the increased effective mass at the Br_2/I sites, resulting from the larger atomic mass of iodine, contributes to the overall softening of these vibrational modes.

Figure 28 – Raman spectra of $CsPb_2(Br,I)_5$ single crystals. The asterisk indicates a leaking plasma line of the 568 nm excitation laser line.

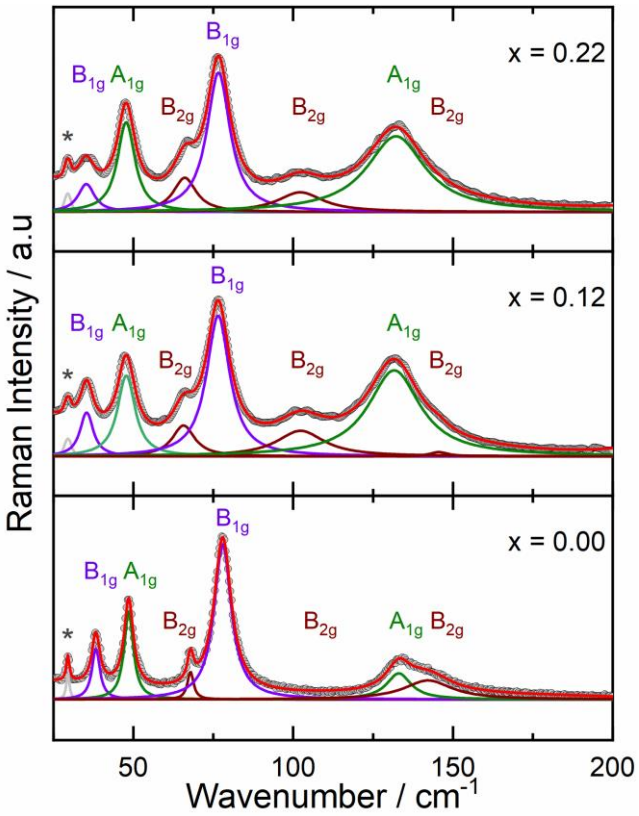

Source: Elaborated by the author.

Another interesting observation is the appearance of a peak at 102 cm^{-1} in the iodine-substituted samples, which is absent in the pure compound. In their lattice dynamics calculations, Hadjiev et al. (Hadjiev et al. 2018) predicted this peak and was attributed to a B_{2g} mode that is not detectable experimentally due to its weak Raman activity. However, the bond polarizability increases upon iodine substitution, resulting in an enhancement of the intensity of this mode. The $CsPb_2Br_5$ sample displays narrower bands, indicating a more ordered crystal

structure than the iodine-substituted samples. Table 9 summarizes and compares the experimental band positions with theoretical literature results.

Table 9 – Mode symmetry comparison between experimental $CsPb_2(Br_{1-x}I_x)_5$ (x = 0.00, 0.12 and 0.22) Raman spectrum positions and the DFPT Raman of the $CsPb_2Br_5$ crystal.

Mode Symmetry	DFPT PAW $(cm)^{-1}$ [(Hadjiev et al., 2018)]	$CsPb_2Br_5$ $(cm)^{-1}$	$CsPb_2(Br_{0.78}I_{0.22})_5$ $(cm)^{-1}$	$CsPb_2(Br_{0.78}I_{0.22})_5$ $(cm)^{-1}$
E_g	36	38	36	36
B_{1g}	41			
A_{1g}	54	49	48	48
E_g	56			
B_{2g}	69	68	66	66
E_g	70			
B_{1g}	77	78	77	77
E_g	78			
A_{1g}	82			
B_{2g}	95		102	102
E_g	114			
A_{1g}	132	133	132	132
B_{2g}	148	142		

Source: Elaborated by the author.

5.3 Unraveling the Role of Iodide in the Photoluminescence

The partial substitution of bromine by iodine in the $CsPb_2Br_5$ crystal structure has significantly influenced the lattice parameters and the arrangement of the two-dimensional (2D) layers. This substitution increases interatomic distances, potentially resulting in notable modifications to the optoelectronic properties of the crystals. Previous studies conducted by (Li, P. *et al.*, 2018), (Tang *et al.*, 2018), (Ma *et al.*, 2019b) and (Sichert *et al.*, 2015) have extensively investigated the emission characteristics of $CsPb_2Br_5$ nanocrystals, microplates, and films, revealing a strong green emission peak centered at approximately 520 nm. Having explored the emission properties under various experimental settings, these investigations have offered insightful information into the PL behavior of $CsPb_2Br_5$-based materials.

However, the PL mechanism of $CsPb_2Br_5$ has been a topic of extensive debate, as theoretical calculations suggest that it should exhibit low PL activity due to being an indirect bandgap semiconductor. Several proposals have been in contradiction, and one possible explanation is the presence of emissive $CsPbBr_3$ impurities within the $CsPb_2Br_5$ crystal lattice. These impurities may introduce localized states or defects that facilitate radiative recombination

and contribute to the observed PL signal. A similar phenomenon was observed in another compound within the Pb-Cs-Br phase diagram, Cs_4PbBr_6, where the PL emission was attributed to nano-inclusions of $CsPbBr_3$ as an extrinsic effect. In this case, the nano sized $CsPbBr_3$ inclusions act as efficient emitters due to their direct bandgap nature, which contrasts with the indirect bandgap of Cs_4PbBr_6 (Castro Ferreira, Araújo, Gómez, M. A. P., *et al.*, 2022a). It is plausible that a similar extrinsic effect involving $CsPbBr_3$ nano-inclusions may contribute to the PL emission observed in $CsPb_2Br_5$.

In contrast, iodine pure crystals were characterized in nanocrystals form (Zhang *et al.*, 2020). The presence of I ion decreases the optical bandgap, which agrees with experimental absorption results in $CsPb(Br,I)_3$ perovskites (Wang et al., 2016). The PL spectrum of the single crystals $CsPb_2(Br_{1-x}I_x)_5$ (x = 0.00, 0.12, and 0.22) recorded at room temperature are presented in Figure 29.

The $CsPb_2Br_5$ displays a strong and continuous green PL around 525 nm (2.36 eV) after exposure to different excitation energies, as described in previous studies of nanoplates and thin films based on this compound. This PL behavior is reminiscent of other perovskite-related compounds, such as $CsPbBr_3$ and Cs_4PbBr_6 (Akkerman, Abdelhady e Manna, 2018; Castro Ferreira, Araújo, Gómez, M. A. P., et al., 2022), which also exhibit bright green PL within a similar wavelength range. With the addition of iodine, the PL intensity increases, and its center shifts to 2.34 eV (528 nm) for x=0.12 and 2.32 eV (535 nm) for x=0.22. These shifts in the PL wavelength can be attributed to the expansion of the Pb-X bond distances caused by the incorporation of iodine. As the interatomic distances increase, the energy levels associated with the radiative recombination processes are affected, resulting in the observed shifts in the PL spectrum. The tunability of the optical properties, including both PL intensity and emission wavelength, makes $CsPb_2(Br,I)_5$ compounds promising candidates for applications in photodetectors and optoelectronic devices. The ability to control and tailor these properties through iodine substitution offers opportunities for designing materials with desired optical characteristics for specific device requirements.

Figure 29 – (a) The optical photoluminescence measurement spectra of the $CsPb_2(Br_{1-x}I_x)_5$ for x=0 (Black), x=0.12 (Blue), and x=0.22 (Green) sample, (b) the PL center modification over the substitution of the iodine content, and (c) the spectrum difference in intensity between the pure bromide crystal and the substitution samples.

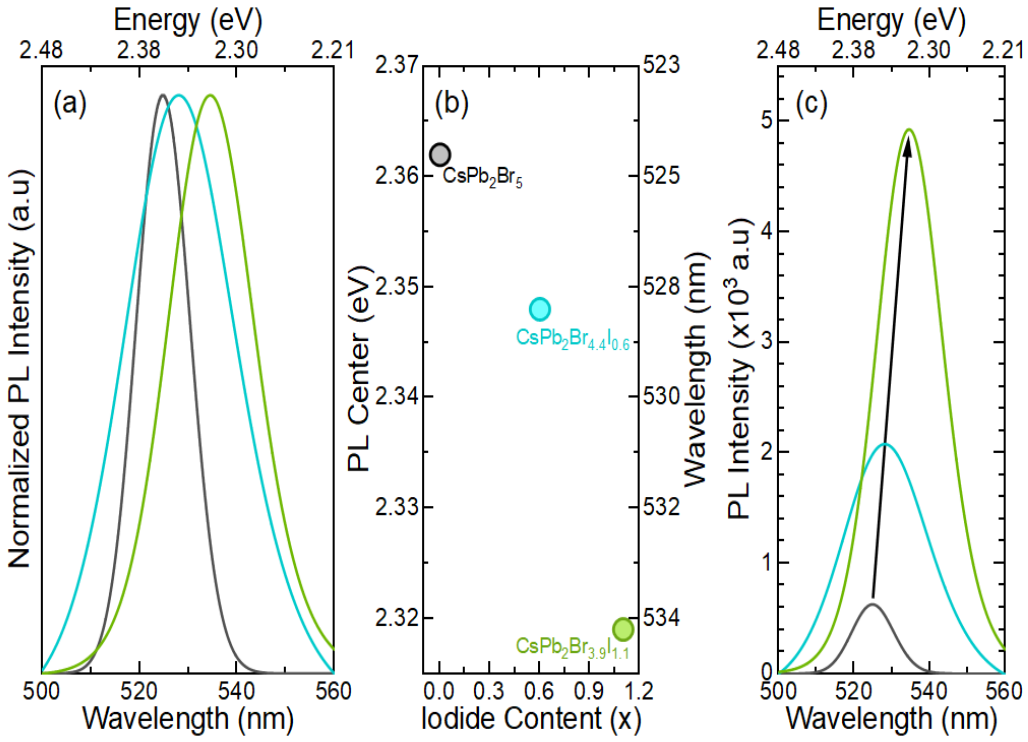

Source: Elaborated by the author.

The family of inorganic 2D perovskite-related compounds $CsPb_2(Br_{1-x}I_x)_5$ was successfully synthesized and characterized. Through SCXRD analysis, we observed an interesting occupational disorder at the 16l site, with both Br and I ions occupying the same position. This disorder leads to structural distortions in the decagons and proper layers, expanding the crystal lattice parameters proportional to the difference in ionic radii between the two halogens. Raman spectroscopy studies further support the well-ordered crystal structure of $CsPb_2Br_5$ compared to its iodine-substituted counterparts. The characteristic vibrational modes exhibit minimal shifts, indicating the structural integrity of $CsPb_2Br_5$ and stability upon iodine incorporation. This finding highlights the successful incorporation of iodine into the crystal lattice without introducing significant structural distortions.

Regarding photoluminescence (PL) properties, $CsPb_2Br_5$ demonstrates a continuous emission spectrum centered at 524.98 nm, corresponding to an energy emission of 2.36 eV. Introducing iodine in the $CsPb_2Br_5$ crystal notably results in a redshift of the PL center. Specifically, $CsPb_2Br_{4.4}I_{0.6}$ exhibits a PL center at 2.34 eV (528.1 nm), while $CsPb_2Br_{3.9}I_{1.1}$ displays a PL center at 2.32 eV (534.71 nm). Remarkably, all these materials exhibit intense green photoluminescence, indicating their potential for optoelectronic applications. The observed redshift in the PL center can be attributed to the expansion of the Pb-X bond distances, which alters the interatomic interactions and energy levels associated with radiative recombination processes. This modification in the crystal structure and electronic properties enables tuning the PL emission wavelength in the green spectral range. Additionally, the introduction of iodine leads to a significant enhancement in the intensity of photoluminescence in the $CsPb_2(Br,I)_5$ compounds.

6 Exploring the Electron-Phonon Coupling in the 2D $CsPb_2Br_5$.

Multiple reports have highlighted the exceptional properties of materials based on halide perovskites (MHPs) (McGehee, 2013, 2014; Yakunin *et al.*, 2015). The basic crystal structure of MHPs is a simple cubic lattice with the space group $Pm\bar{3}m$ and a general stoichiometric formula of ABX_3, where A represents a monovalent isolated cation situated at the center of the unit cell with a cube-octahedral symmetry. The divalent metallic element B is located at the corners of the cube, coordinated by twelve halide ions X, with B and X organized as BX_6 octahedra (Huang *et al.*, 2017; Li, Z. *et al.*, 2018; Lin *et al.*, 2018).

Replacing organic cations with inorganic components has emerged as a promising approach to enhance the stability of perovskites (Hu et al., 2022). In this context, cesium-based perovskites have attracted significant attention due to their improved long-term stability against humidity and extreme conditions, making them promising candidates for efficient and durable photovoltaic devices (Zhang, J., Hodes, Jin e Liu, S., 2019). Pure inorganic halide devices based on lead and cesium ($CsPbX_3$) have played a significant role in the field of photovoltaics, exhibiting a power conversion efficiency (PCE) of 17.1%, stable light absorption properties, and the ability to tune their properties through crystal polymorphism, thus showing potential for applications in light-emitting diodes (LEDs) (Protesescu *et al.*, 2015a) photodetectors, (Zhang, Z. *et al.*, 2018) lasers (Li *et al.*, 2017), and flexible electronics compounds (Yuan *et al.*, 2017).

Parallel to the advancements in $CsPbX_3$ achievements, its all-inorganic derivatives, Cs_4PbX_6 and $CsPb_2X_5$, have been rapidly developed (Cao et al., 2020; Castro Ferreira, Araújo, Gómez, M. A.P., et al., 2022; Cho e Yun, 2020). However, all these $Cs_xPb_yX_z$ materials share the same elemental components but exhibit entirely different connectivity patterns, such as octahedra or polyhedra. The $CsPbX_3$ adopts a three-dimensional (3D) perovskite for the corner-shared octahedra along all three crystal axes, while $CsPb_2X_5$ is characterized by a sandwich arrangement of Pb-X planes formed by polyhedra regarded as a 2D phase (Lange *et al.*, 2020). Cs_4PbX_6, on the other hand, features completely decoupled $[PbX_6]^{4-}$ octahedra, resulting in a zero-dimensional (0D) structure. These low-dimensional cesium lead halide-related perovskites, including Cs_4PbX_6 and $CsPb_2X_5$, have garnered attention due to their excellent photophysical properties, including high photoluminescence quantum yields (PLQY), narrow

emission linewidths, broad absorption spectra, high color purity, and tunable emission in the visible light region through halide substitution (Le et al., 2018; Yin et al., 2017).

In the case of 2D $CsPb_2X_5$, the electronic bands are confined within the Pb-X planes and do not easily dissociate in all crystal dimensions, resulting in larger band gaps than $CsPbX_3$. The photoluminescence (PL) of $CsPb_2Br_5$ has been extensively studied, and different growth habits have been observed, leading to discrepancies in the PL values and origin mechanisms (Ghaithan *et al.*, 2020; Zhang e Yin, 2018). Two possible origins for the photoluminescence have been proposed: i) the emissive clusters of the $CsPbBr_3$ impurities (Shamsi *et al.*, 2019); and ii) the dominant intrinsic defects that facilitate exciton-assisted emission (Tan *et al.*, 2019). It has been described that $CsPb_2Br_5$ nanosheets are PL-inactive semiconductors (Li *et al.*, 2016). However, other studies have reported strong green PL in $CsPb_2Br_5$ microplates (Zhang, T., Chen, Zhihui, Shi e Xu, Q. H., 2019). On the other hand, (Bao e Hadjiev, 2019) found that nanosheets produced by converting $CsPbBr_3$ traces into $CsPb_2Br_5$, the nanostructures displayed a high PL centered at 514 nm. $CsPb_2Br_5$ nanoplates with a narrow emission peak of 530 nm were produced by (Sahoo et al., 2022). Thin films with a thickness of 100 nm showed a PL wavelength peak of 517 nm (Qin *et al.*, 2017), and (Li *et al.*, 2017) reported that $CsPb_2Br_5$ presented quantum dots (QDs) PL centered at 500-519 nm. Due to that discrepancy, the comprehensive analysis of the PL emission and its origin in $CsPb_2Br_5$ is related; the analysis was carried out at low-temperature experiments to provide a deeper understanding.

The $CsPb_2Br_5$, as an indirect bandgap compound, presents an electronic transition where phonons participate in the radiative electron recombination process (Hu *et al.*, 2016). Hence, it is more susceptible to electron-phonon interactions (Li, Wang e Li, 2020). Materials with strong electron-phonon coupling often display intrinsic electronic transitions, forming localized excitonic carriers that can contribute to diverse photoluminescence (PL) processes (Grancini e Nazeeruddin, 2018). Therefore, a comprehensive investigation was conducted to gain insights into the origin of the PL mechanism in $CsPb_2Br_5$ using low-temperature Raman spectroscopy and photoluminescence measurements. The analysis of low-temperature Raman spectra provides valuable information about the dynamics within the crystal lattice, particularly focusing on the influence of anharmonic effects. These effects have a significant impact on the behavior of the Raman modes, shedding light on the lattice dynamics and providing insight into the interaction between phonons and charge carriers, which in turn contributes to the understanding of the photoluminescence processes in $CsPb_2Br_5$.

6.1. Study of the emissive cluster traces on $CsPbBr_3$ through Raman Spectroscopy

The room-temperature structure of $CsPb_2Br_5$ was determined using Single-Crystal X-Ray Diffraction (SCXRD), revealing a tetragonal structure with *I*4/*mcm* symmetry. The low-temperature compound did not present structural phase transitions (Hadjiev et al., 2018). The group theory analysis indicates that the Br_1 atom, represented by the 4*c* site, does not contribute to the Raman-active phonons. On the other hand, the Cs atom at the *4a* site exhibits one active band with E_g symmetry. The Pb atom at the *8h* is associated with vibrational modes $A_{1g}\oplus B_{1g}\oplus B_{2g}$, which result from the shifting of lead cations from an off-centered position within the polyhedra surrounding the *16l* site occupied by the Br_2 atom, which vibrations correspond to bendings directly linked to the atomic displacements of the polyhedra tip, possessing $A_{1g}\oplus B_{1g}\oplus B_{2g}$ symmetries.

To investigate the vibrational response of $CsPb_2Br_5$ over a wide temperature range, measurements were performed from room temperature down to 14 K. At low temperatures, the Raman peaks exhibit enhanced resolution and sharper profiles compared to those observed at higher temperatures (see Figure 30a). This improved spectral resolution enables a more detailed analysis of the vibrational modes and their corresponding frequencies. Lorentzian peak fitting was employed to quantify the temperature dependence of the Raman-active bands, determining the center parameter for each mode as a function of temperature. The results are presented in Figure 30b, demonstrating that no significant shifts in the Raman modes were observed across the investigated temperature range. The frequencies associated with the lattice vibrations, such as the mode at 156 cm^{-1}, indicate that the crystal lattice of $CsPb_2Br_5$ and its interaction with excitons are sensitive to temperature-induced changes in the lattice dimensions. These findings highlight the importance of considering the temperature effects on the lattice dynamics and their impact on the properties of $CsPb_2Br_5$.

Figure 30 – (a) The normalized Raman spectra of the $CsPb_2Br_5$ sample from 290 K until 14 K, and (b) the center low-temperature evolution of the Raman active modes.

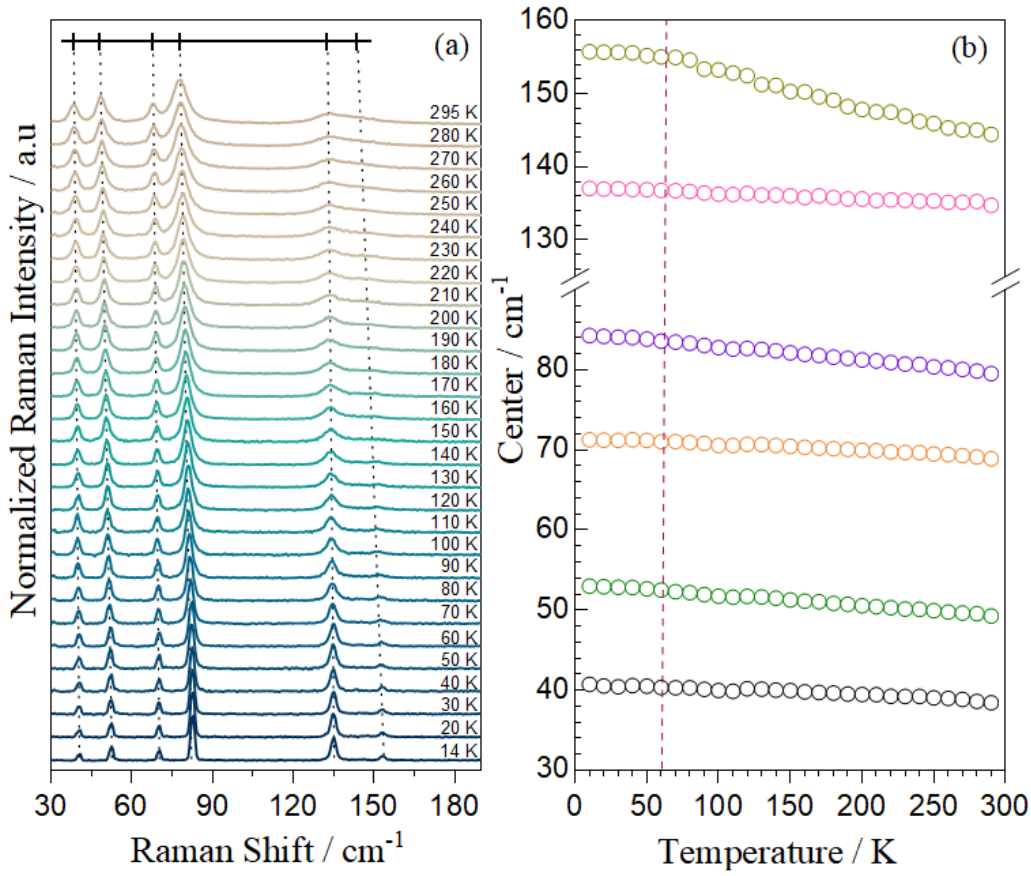

Source: Elaborated by the author.

Contrary to the findings (Hadjiev et al., 2018), the low-temperature Raman spectra did not reveal any discernible peaks corresponding to the characteristic vibrations of $CsPbBr_3$. Specifically, the absence of characteristics $CsPbBr_3$ phonons 28 cm^{-1} and 32 cm^{-1} provides compelling evidence to refute the hypothesis that the observed photoluminescence (PL) in $CsPb_2Br_5$ originates from emissive clusters of $CsPbBr_3$ impurities. The absence of $CsPbBr_3$-related Raman bands strongly suggests that the observed PL in $CsPb_2Br_5$ samples can be attributed to intrinsic mechanisms within the crystal lattice. This finding is of great significance as it highlights the integrity of $CsPb_2Br_5$. The absence of $CsPbBr_3$ enhances the understanding and paves the way for optimizing the optoelectronic properties of $CsPb_2Br_5$. By discarding the $CsPbBr_3$ contribution, it confidently focuses on investigating and manipulating the intrinsic mechanisms of the $CsPb_2Br_5$ crystal lattice, which plays a crucial role in the electronic carrier

dynamic. These results contribute to a more comprehensive understanding of the fundamental photophysical properties of $CsPb_2Br_5$ and provide valuable insights for developing advanced optoelectronic devices based on this material.

6.2. *The exciton dynamics and their contribution to electron-phonon coupling at low-temperature.*

As previously reported, $CsPb_2Br_5$ has been shown to exhibit continuous green photoluminescence centered at 524.98 nm, corresponding to an energy emission of 2.36 eV. Notably, this investigation revealed intriguing changes in the photoluminescence spectra at low temperatures, particularly an enhancement in the emission intensity (Figure 31a). At 60 K, the low-dimensional nature of the compound manifested as a dual-emission band, as depicted in Figure 31b. It is plausible to attribute this phenomenon to the interplay between thermal expansion effects and the vibrational lattice dynamics, which lead to modifying the emission characteristics at elevated temperatures.

To further understand the underlying mechanisms governing the temperature-dependent photoluminescence behavior, it was analyzed the intensity ratio (I_{narrow}/I_{new}) as a function of temperature, as presented in Figure 31c. Remarkably, the intensity ratio exhibited a linear decrease with decreasing temperature, indicative of the involvement of prohibited states and the intricate dynamics of electronic carriers within the crystal lattice. These observations align with previous studies (Smith e Karunadasa, 2018; Yangui *et al.*, 2015), which have elucidated the role of forbidden states and carrier dynamics in dictating the optical properties of similar materials.

The observed a decrease in intensity which can be attributed to an energy process involving the thermal activation of trapped carriers (Peters *et al.*, 2021). This phenomenon has been previously observed in certain lead halide perovskites that exhibit narrow room-temperature photoluminescence outside the $CsPbBr_3$ cluster hypothesis, and it is associated with the radiative recombination of free excitons (FE). The exciton strongly interacts with the lattice in these materials, leading to lattice distortions. As a result, the FE decays into an excited state associated with point defects, giving rise to a new exciton-exciton binding and recombination process. These lattice-induced deformations effectively stabilize the exciton, leading to a broad emission known as self-trapped excitons (STE) (Xu *et al.*, 2021). The energy of the STE peaks is typically only a few meV below that of the FE band and is often observed

near each other. STE in the photoluminescence spectra indicates localized exciton states forming due to strong exciton-lattice interactions. These self-trapped excitons contribute to the broadening and spectral shifts observed in the low-temperature photoluminescence spectra. The STE emission is commonly observed in the energy range close to that of the FE band, further confirming their interplay and the influence of lattice deformations on the optical properties of the material.

Figure 31 – (a) The low-temperature photoluminescence evolution spectra in the $CsPb_2Br_5$ sample, (b) the photoluminescence emissions from 60 K until 11 K where are displayed the emissions bands, and (c) the intensity relationship ratio between both emissions as a function of temperature.

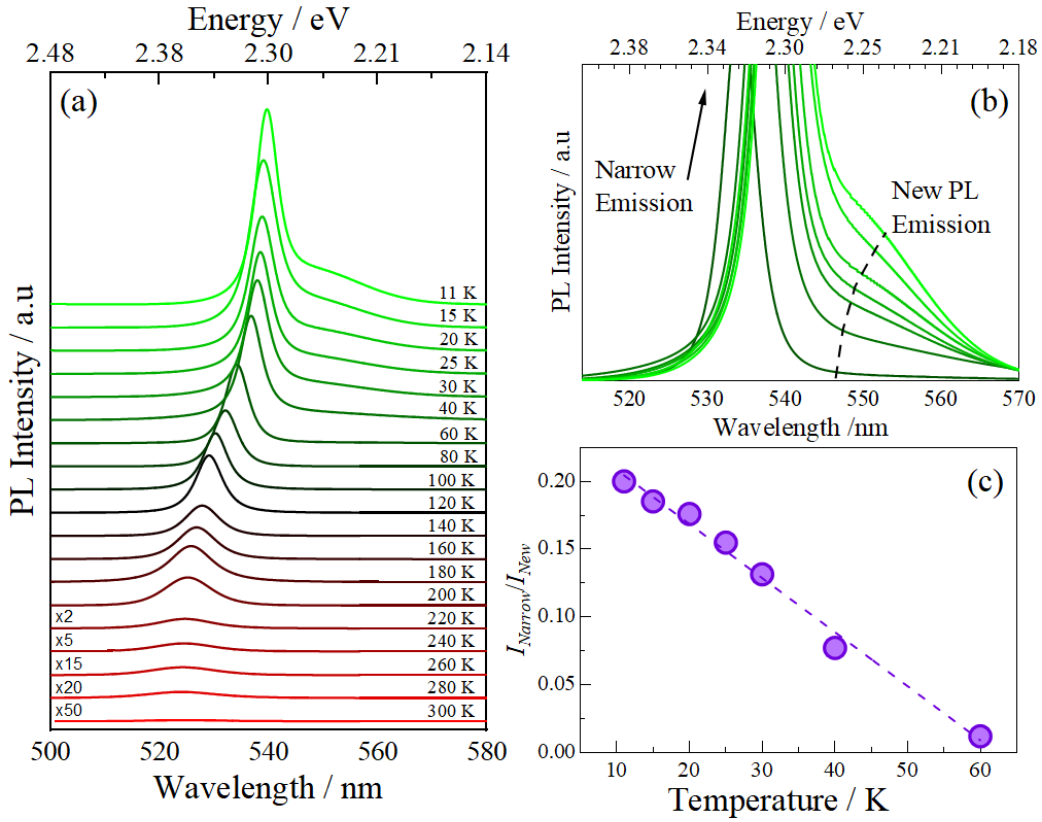

Source: Elaborated by the author.

Unlike the room-temperature PL, the self-trapped exciton (STE) emission in $CsPb_2Br_5$ occurs at significantly lower energies compared to the bandgap and the free exciton (FE) emission, owing to the higher potential energy associated with the ground state lattice

deformation (Lin *et al.*, 2022). The formation of the self-trapped state involves a distortion in the lattice configuration, which requires an activation energy (E_{st}) for the STE emission to occur. This activation energy is a barrier that facilitates the stabilization and subsequent emission of the self-trapped excitons. In Figure 32a, the distinct PL bands in $CsPb_2Br_5$ are clearly illustrated. The blue curve corresponds to the narrow emission from free excitons in the FE band, while the red curve represents the self-trapped exciton emission arising from the recombination of excitons in the STE band. The presence of STE leads to the observed dual-emission band, where both FE and STE contribute to the photoluminescence at low temperatures (Figure 32b). At high temperatures, the thermal energy is insufficient to overcome the activation energy barrier for self-trapping, making it difficult for electrons in the FE band to access the prohibited states associated with STE (Li, Wang e Li, 2020). Consequently, only the emission from free excitons is observed at higher temperatures, as the population of the self-trapped exciton states is limited. This temperature-dependent behavior explains the absence of STE emission at elevated temperatures and highlights the importance of the activation energy barrier in regulating the excitation and emission processes in $CsPb_2Br_5$.

Table 10 – Fitted values of the adjustments for the PL center and FWHM parameters.

$E(T) = E_0 + A_{TE}T + A_{EP}\left[\frac{2}{e^{\frac{\hbar\omega}{k_bT}}-1}+1\right]$ (8)	$E_{g\,(T=0)}$ (eV)	A_{TE} (meV/K)	A_{EP} (meV)	$\hbar\omega$ (meV)
	2.2920 ± 0.0005	47.772 ± 0.001	146 ± 13	43 ± 3
$I(\mathrm{T}) = \left[\frac{I_0}{1+Ae^{\frac{-E_A}{k_bT}}}\right]$ (9)	I_0 (μa.u)	A	E_A (meV)	
	1.1 ± 0.1	-	41 ± 2	
$\Gamma(T) = \Gamma_0 + \gamma_{ac}T + \frac{\gamma_{LO}}{e^{\frac{E_{LO}}{k_bT}}-1}$ (10)	Γ_0 (meV)	γ_{ac} (meV/K)	γ_{LO} (meV)	E_{LO} (meV)
	10.6 ± 0.5	27 ± 9	68 ± 9	32 ± 3

Source: Elaborated by the author

Figure 32 – (a) Nuclear coordinate diagram for the PL emissions in the $CsPb_2Br_5$, (b) the dual-emission band energy as a function of temperature. (GS = Ground State, FC = Free Carrier, FE = Free Exciton, STE = Self-Trapped Exciton, E_g = Band Gap Energy, E_b = Activation Energy for FE process, E_{st} = Activation Energy for STE detrapping, $E_{PL,\,FE}$ = FE Photoluminescence,

and $E_{PL,\ STE}$ = STE Photoluminescence) and (c) the intense blue-green (teal) light-emitting photoluminescence of $CsPb_2Br_5$.

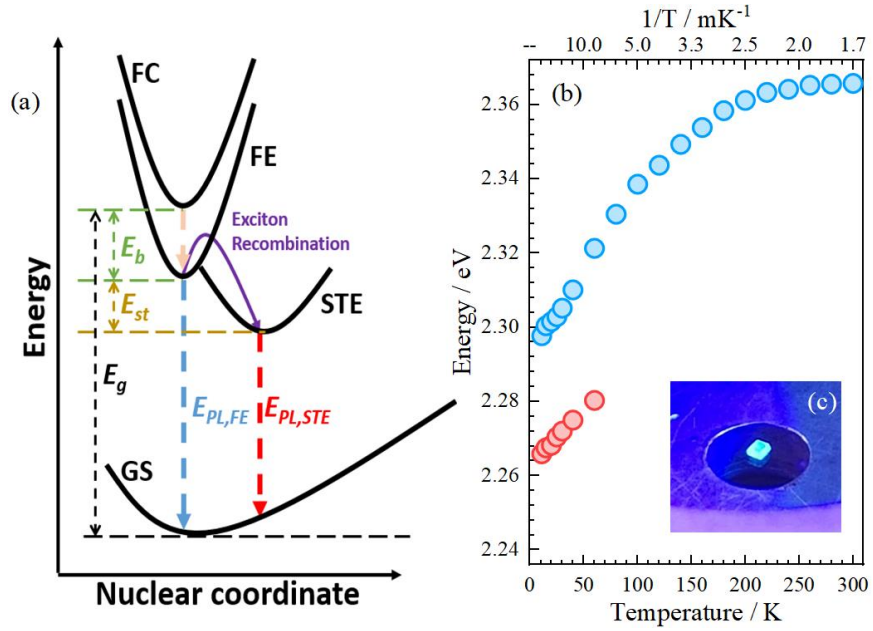

Source: Elaborated by the author.

Based on the observed exciton-exciton recombination behavior in the broad PL band and the limited understanding of the physical origins of these low-temperature dependencies, a comprehensive analysis of the peak center position, intensity, and full width at half maximum (FWHM) of the novel band was not performed. However, to gain further insights into the strength of the electron-phonon coupling and the impact of lattice thermal expansion, the temperature dependence of the principal band associated with the free excitons (FE) was carefully examined. In this regard, the models presented in Table 10 were employed to fit the temperature-dependent behavior of the FE-related band. By employing these models, a systematic analysis of the FE band allowed for a more comprehensive understanding of the underlying mechanisms governing its temperature dependence. The fitting procedure provided valuable information about the electron-phonon interactions and the influence of lattice thermal expansion on the FE emission.

Figures 33a-c provide a comprehensive analysis of the temperature-dependent evolution of the investigated parameters, offering valuable insights into the underlying physics of $CsPb_2Br_5$. The energy-temperature relationship $E(T)$ (see Figure 18a) is described by the sum

of distinct contributions as an unrenormalized bandgap at $T = 0$ (E_0), the electron-phonon energy interaction (A_{EP}), the weight thermal expansion (A_{TE}), and $\hbar\omega$ representing the average optical phonon energy.

In the intensity model, several parameters play a crucial role in characterizing the photoluminescence behavior of the system. Firstly, I_0 represents the PL intensity at $T = 0$, providing insights into the initial emission intensity of the material. Additionally, E_A, the activation energy indicates the significant contribution of thermal dissociation of free excitons (FE) to enhance the PL intensities. This parameter captures the energy required for the thermal activation process that promotes the release of carriers and subsequent increases in PL intensity. The constant factor A, which depends on the luminescence lifetime, is crucial for understanding the dynamics of the emitted light (Sahoo et al., 2022). The A parameter reflects the interplay between radiative and nonradiative decay processes, providing insights into the radiative recombination efficiency and the excitonic states overall lifetime.

Turning to the full width at half maximum FWHM function, the associated parameters contribute to the broadening of the PL spectra. Γ_0 captures the scattering effects arising from disorder and crystallographic imperfections in the material. It represents the FWHM value at $T = 0\,K$, reflecting the intrinsic broadening of the material in the absence of thermal effects. Moreover, the FWHM adjustment includes terms related to homogeneous broadening. Specifically, the Fröhlich coupling constants γ_{ac} and γ_{LO} account for the interaction between charge carriers and acoustic and longitudinal optical phonons (Iaru *et al.*, 2021). These terms contribute to the broadening of the PL spectra by influencing the dynamics of the excitonic states. Furthermore, the phonon energy, represented by E_{LO}, plays a crucial role in determining the energy scale associated with the phonon modes involved in the electron-phonon interactions. The analysis of E_{LO}, as depicted in Figure 32c, provides valuable insights into the vibrational properties of the material and their influence on the observed PL spectra.

Figure 33 – The FE PL parameters (a) center, (b) intensity, and (c) FWHM for $CsPb_2Br_5$.

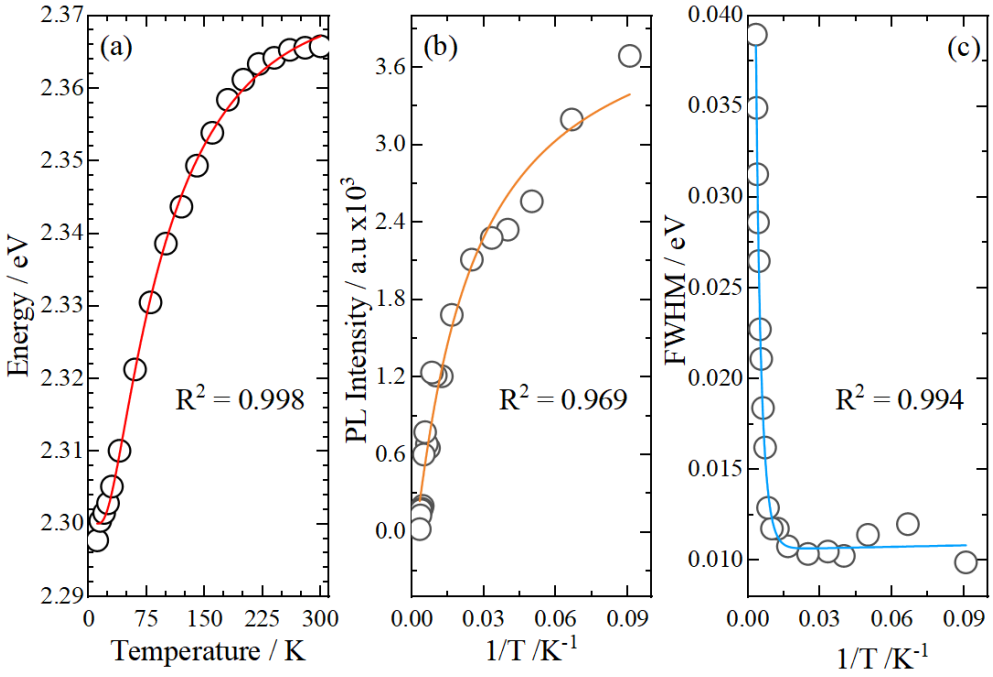

Source: Elaborated by the author.

The analysis of S, characterizes the degree of interaction between electronic excitations and lattice vibrations, including the formation and dynamics of excitons, phonon-assisted processes, and the overall optoelectronic performance. A strong electron-phonon coupling regime signifies a significant coupling between the electronic and vibrational degrees of freedom, indicating a substantial exchange of energy and momentum between the charge carriers and lattice vibrations. Upon photogeneration of electrons and holes, it is observed that excitons in $CsPb_2Br_5$ quickly self-trap due to the availability and increased stability of self-trapped states in the presence of lattice distortion. The formation of self-trapped excitons (STEs) relies on strong electron-phonon coupling, which can be evaluated using the Huang-Rhys factor $S = A_{TE}/\hbar\omega$. This factor quantifies the strength of electron-phonon coupling by indicating the number of phonons emitted after carrier capture (Whalley *et al.*, 2021). Typically, a value of $S \gg 1$ indicates a strong coupling regime. In the case of $CsPb_2Br_5$, the determined value of S is approximately 4, indicating a strong electron-phonon coupling regime. This value is comparable to other halide perovskites, such as the inorganic counterpart $CsPbBr_3$ ($S = 3.22$) (Chen, Chen e Huang, 2023). However, it should be noted that $CsPb_2Br_5$ does not exhibit as significant room-temperature STEs emissions as observed in $Cs_3Sb_2I_9$ ($S = 42.7$), $Rb_3Sb_2I_9$

($S = 50.4$), $Cs_3Bi_2I_9$ ($S = 79.5$) (McCall *et al.*, 2017) or in one-dimensional hybrid perovskites such as $C_5H_{16}N_2Pb_2Br_6$ ($S = 54$), $[C_6H_7ClN]CdCl_3$ ($S = 62.94$)(Xu *et al.*, 2022), and $[C_7H_{10}N]_3[BiCl_5]Cl$ ($S = 45$) (Klement *et al.*, 2021), for the low-temperature STEs emissions.

However, at higher temperatures, the energy barrier between the FE and STE states impedes the simultaneous emission of both bands. This behavior can be attributed to the Fröhlich interactions present in $CsPb_2Br_5$, which manifest as an exciton-phonon coupling phenomenon. To further support this hypothesis, the strength of the exciton-phonon interaction by analyzing the FWHM of the photoluminescence spectra needs to be done. The obtained fitted values of γ_{ac} and γ_{LO} exhibit an interesting relationship, with γ_{LO} being approximately three times larger than γ_{ac}. This finding suggests a significant contribution of exciton-phonon coupling involving optical modes, commonly observed in two-dimensional lead halide semiconductors (Wang, Y. *et al.*, 2023). Notably, the γ_{LO} value in $CsPb_2Br_5$ (40-65 meV) is similar to reported for $CsPbBr_3$, which also exhibits broad emission from free excitons (FE) and a second band attributed to self-trapped excitons (STE) at low temperatures (Anni *et al.*, 2021; Li *et al.*, 2023). In contrast, the γ_{LO} values observed in Rb_3BiCl_6 (693.6 meV) and Rb_3BiCl_6:4.55%Sb (347.3 meV) (Zhou *et al.*, 2021) indicate multiple STE emissions. Electron-phonon interaction in the sample, as indicated by the activation energy E_A= 41 meV, is closely tied to the exciton-phonon coupling characterized by the activation energy E_{LO}=32 meV. This coupling enables phonon-assisted electronic transitions, enhancing the photoluminescence intensity through the population of optical phonons.

6.3. Exciton Dynamics and Color Purity Revealed through CIE Chromaticity Diagram

To explore the potential applications of the intense teal-emitting photoluminescence in $CsPb_2Br_5$ for low-temperatures Light Emitting Diode (LEDs), a comprehensive investigation was conducted to analyze the influence of the spectral power distribution on the emission color. The analysis utilized the CIE 1931 color space curve, which characterizes the perceived human optical color based on the (x, y) chromaticity coordinates established by the Commission Internationale de l'Eclairage (CIE) (Zhu *et al.*, 2019). Figure 34 depicts the calculated chromaticity coordinates in the CIE-1931 plot for the single crystal of $CsPb_2Br_5$ across a range of temperatures, and the corresponding (x, y) values are provided in Table 11. As previously described, the chromaticity coordinate falls at room temperature in the green (teal) region. However, at low temperatures, a noticeable modification in the emission color is observed,

resulting in an intense green color, which has been associated with green luminescence in Cs-Pb-Br perovskites within the visible spectrum (Yin *et al.*, 2023).

The observed changes in the photoluminescence emission color of $CsPb_2Br_5$ can be attributed to the emergence of self-trapped excitons (STEs) at low temperatures. The presence of STEs significantly influences the intensity of the emitted light and leads to alterations in the chromaticity coordinates. This behavior aligns with the previous discussions regarding the pronounced dependence on STEs and emphasizes the importance of comprehending their role in determining the luminescent properties of low-dimensional materials. It is worth noting that the detection of novel contributions from STEs at low temperatures indicates the relaxation of the crystal structure, enabling the appearance of previously inaccessible states. Furthermore, the observed color transition in $CsPb_2Br_5$ highlights the tunability of the optical properties of these materials at low temperatures, thus paving the way for the development of innovative light-emitting devices.

Table 11 – Temperature-dependent chromaticity coordinates of $CsPb_2Br_5$.

Temperature (K)	CIE *x*	CIE *y*	Temperature (K)	CIE *x*	CIE *y*
300	0.13031	0.80233	120	0.15298	0.80309
280	0.12966	0.79938	100	0.16265	0.79734
260	0.12019	0.81115	80	0.17348	0.79275
240	0.12184	0.81128	60	0.19773	0.77497
220	0.12493	0.80943	40	0.23785	0.7417
200	0.12292	0.81526	30	0.24631	0.73648
180	0.13539	0.80537	25	0.25062	0.73329
160	0.13554	0.8109	20	0.25401	0.7309
140	0.14197	0.80924	15	0.25304	0.73207
120	0.15298	0.80309	11	0.25932	0.72706

Source: Elaborated by the author.

The investigation conducted at low temperatures on the 2D $CsPb_2Br_5$ compound has provided valuable insights into the origin of its photoluminescence. Through analysis using Raman spectroscopy, and definitively ruled out the possibility of $CsPbBr_3$ clusters as the source of the observed photoluminescence. The evolution of the photoluminescence spectra at low temperatures reveals an intriguing increase in emission intensity and the emergence of a dual-emission band beyond 60 K.

Figure 34 – CIE-1931 color space with the temperature-dependent chromaticity coordinates of PL emissions of $CsPb_2Br_5$ (purple dots).

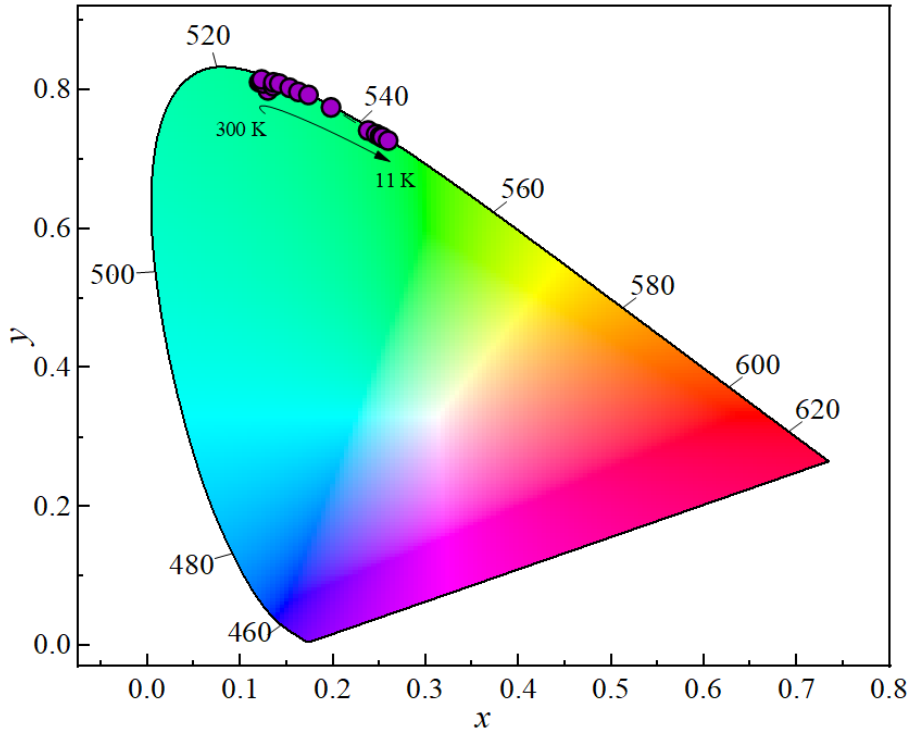

Source: Elaborated by the author.

Both emission processes are closely associated with the inherent electron-phonon interaction in the sample, which gives rise to excitons that carry the emission signals. Specifically, the narrow photoluminescence observed at room temperature can be attributed to the radiative recombination of free excitons, whereas the broad emission observed at low temperatures is ascribed to the presence of self-trapped excitons (STE). The fitting models employed in our study successfully confirm the strong electron-phonon coupling present in the $CsPb_2Br_5$compound. Additionally, the exciton-exciton recombination process highlights the significant effect of exciton-phonon coupling on the photoluminescence behavior. Furthermore, a detailed examination of the spectral power distribution was made by utilizing the CIE 1931 color space curve as a function of temperature. Overall, this study significantly contributes to our understanding of the photoluminescence characteristics of $CsPb_2Br_5$ at low temperatures. The identified emission processes, along with the confirmed electron-phonon coupling, shed light on the fundamental mechanisms underlying the optical properties of this material.

Conclusions

The primary aim of this work is to comprehensively investigate the structural properties relationship of perovskite-like compounds under extreme conditions. The research explores the low-temperature effects on the zero-dimensional $[(CH_3)_2NH_2]_4BiBr_7$ structure. Additionally, it focuses on the pressure-induced structural phase transition in the 2D structure of $CsPb_2Cl_5$, providing valuable insights into the materials response to high pressure. Also, it explores the influence of iodide doping on the perovskite-like properties of 2D $CsPb_2X_5$ (X = Br, I). Moreover, it investigates the electron-phonon coupling in 2D $CsPb_2Br_5$ to understand the mechanisms governing charge transport and phonon interactions.

In summary, the investigation conducted on the $[(CH_3)_2NH_2]_4BiBr_7$ hybrid perovskite-like at low temperatures has provided valuable insights into the correlation between distorted octahedra and their luminescent properties. By manipulating the internal angles within the $[BiBr_6]^{3-}$ octahedra, we were able to observe the emergence of novel self-trapped exciton (STEs) contributions, leading to a distinctive blue turquoise (425 nm) photoluminescence (PL) emission at 90 K. This observation highlights the ability of the material to generate excitonic states that are strongly localized within the crystal lattice. At lower temperatures, we also observed a notable blueshift in the PL profile, showcasing the material's capability to tune the color emission from blue turquoise to light violet as the temperature decreases. These findings demonstrate the potential of $[(CH_3)_2NH_2]_4BiBr_7$ as a versatile candidate for optoelectronic applications, where its luminescent properties can be finely tuned by controlling the temperature. Further investigations are warranted to fully comprehend the underlying mechanisms responsible for the emergence of self-trapped excitons and the observed blueshift behavior, which will contribute to developing novel photonic devices and advancements in the field of perovskite-based optoelectronics.

The structural phase transition of $CsPb_2Cl_5$ under pressure was thoroughly investigated using Synchrotron Powder X-ray Diffraction (SPXRD) and Raman spectroscopy. The experimental findings indicate a sequence of phase transitions from P_I: I4/mcm to P_{II} at 1.60 GPa: I4/m and subsequently to P_{III} at 5.16 GPa: C2. A comprehensive analysis of the Pb-Cl bond lengths (l_1 and l_2) and the Cl-Pb-Cl bond angles (θ_1 and θ_2) within the $PbCl_8$ polyhedral motif was conducted to gain further insights into the structural changes. The results suggest that both Pb-Cl bond lengths significantly contribute to the observed distortion, with l_2 playing a

more dominant role. Moreover, bulk modulus calculations were performed for each phase, yielding values of Bo^{I-II} = 14 ± 4 GPa and Bo^{III} = 27 ± 3 GPa. These findings indicate that $CsPb_2Cl_5$ exhibits structural softness, making it suitable for applications in the flexible electronics industry. The Raman measurements further validate the critical influence of the l_2 bond length on the underlying mechanisms of the structural phase transitions in $CsPb_2Cl_5$, primarily associated with the continuous distortion of the $PbCl_8$ polyhedra. Notably, the Raman spectroscopy results confirm that, despite the observed distortion, the layered structure of $CsPb_2Cl_5$ remains intact, consistent with the observations from SPXRD measurements.

A family of inorganic 2D perovskite-related compounds was successfully synthesized and characterized, $CsPb_2(Br_{1-x}I_x)_5$, where x = 0.00, 0.12, 0.22, and 0.34. Through the analysis of single crystal X-ray diffraction (SCXRD) data, the occupational disorder was observed at the 16l site, with both Br and I ions occupying the same lattice position. This disorder induces structural distortions in the decagonal and layer structures, resulting in the expansion of crystal lattice parameters in proportion to the difference in ionic radii between the two halogens. Further investigation using Raman spectroscopy supports the notion of a well-ordered crystal structure in $CsPb_2Br_5$ compared to its iodine-substituted counterparts. The characteristic vibrational modes exhibit minimal shifts, affirming the structural integrity and stability of $CsPb_2Br_5$ upon incorporating iodine. This finding highlights the successful integration of iodine into the crystal lattice without introducing significant structural distortions.

Regarding the photoluminescence (PL) properties, $CsPb_2Br_5$ exhibits a continuous emission spectrum centered at 524.98 nm, corresponding to an energy emission of 2.36 eV. Introducing iodine into $CsPb_2Br_5$ crystal results in a noticeable redshift in the PL center. Specifically, $CsPb_2Br_{4.4}I_{0.6}$ exhibits a PL center at 2.34 eV (528.1 nm), while $CsPb_2Br_{3.9}I_{1.1}$ displays a PL center at 2.32 eV (534.71 nm). Remarkably, all these materials exhibit intense green photoluminescence. The observed redshift in the PL center can be attributed to the expansion of the Pb-X bond distances, which affects the interatomic interactions and energy levels associated with radiative recombination processes. This modification in the crystal structure and electronic properties enables precise tuning of the PL emission wavelength in the green spectral range. Additionally, introducing iodine significantly enhances the intensity of photoluminescence in the $CsPb_2(Br,I)_5$ compounds, further establishing their potential for optoelectronic applications.

The investigation conducted at low temperatures on the 2D $CsPb_2Br_5$ compound has yielded valuable insights into the origin of its photoluminescence. Through comprehensive analysis utilizing Raman spectroscopy, we have definitively ruled out the possibility of $CsPbBr_3$ clusters as the source of the observed photoluminescence. The observed evolution of the PL spectra at low temperatures reveals intriguing phenomena, including increased emission intensity and the emergence of a dual-emission band beyond 60 K. These emission processes are closely associated with the inherent electron-phonon interaction within the sample, leading to the formation of excitons that carry the emission signals. Specifically, the narrow photoluminescence observed at room temperature can be attributed to the radiative recombination of free excitons, while the broad emission observed at low temperatures is recognized as the presence of self-trapped excitons (STE). The employed fitting models in our study successfully confirm the strong electron-phonon coupling in the $CsPb_2Br_5$ sample.

Furthermore, the analysis highlights the significant influence of exciton-phonon coupling on the photoluminescence behavior, specifically in the exciton-exciton recombination process. Moreover, we conducted a detailed examination of the spectral power distribution by utilizing the CIE 1931 color space curve as a function of temperature. This comprehensive study contributes significantly to our understanding of the photoluminescence characteristics of $CsPb_2Br_5$ at low temperatures. The identified emission processes, along with the confirmed electron-phonon coupling, shed light on the fundamental mechanisms underlying the optical properties of this material. These findings enhance our knowledge of the photoluminescence behavior of $CsPb_2Br_5$ and provide essential insights into its potential applications in optoelectronic devices, such as light-emitting diodes and photodetectors.

REFERENCES

ADAMS, S. Relationship between bond valence and bond softness of alkali halides and chalcogenides. *Acta Crystallographica Section: s*tructural science, v. 57, n. 3, p. 278–287, 1 jun. 2001.

AGBAOYE, R. O.; ADEBAMBO, P. O.; ADEBAYO, G. A. First principles comparative studies of thermoelectric and other properties in the cubic and hexagonal structure of $CsCdCl_3$ halide perovskites. *Computational Condensed Matter*, v. 21, p. e00388, 1 dez. 2019.

AHN, J.; LEE, E.; TAN, J.; YANG, W.; KIM, B.; MOON, J. A new class of chiral semiconductors: chiral-organic-molecule-incorporating organic–inorganic hybrid perovskites. *Materials Horizons*, v. 4, n. 5, p. 851–856, 1 set. 2017.

AKKERMAN, Q. A.; ABDELHADY, A. L.; MANNA, L. Zero-Dimensional Cesium Lead Halides: History, Properties, and Challenges. *The Journal of Physical Chemistry Letters*, v. 9, n. 9, p. 2326–2337, 3 maio 2018.

AKKERMAN, Q. A.; MANNA, L. What Defines a Halide Perovskite? *ACS Energy Letters*, v. 5, n. 2, p. 604–610, 14 fev. 2020.

AKKERMAN, Q. A.; MEGGIOLARO, D.; DANG, Z.; ANGELIS, F. DE; MANNA, L. Fluorescent Alloy CsPb x Mn 1– x I 3 Perovskite Nanocrystals with High Structural and Optical Stability. *ACS Energy Letters*, v. 2, n. 9, p. 2183–2186, 8 set. 2017.

ALAEI, A.; CIRCELLI, A.; YUAN, Y.; YANG, Y.; LEE, S. S. Polymorphism in metal halide perovskites. *Materials Advances*, v. 2, n. 1, p. 47–63, 2021.

ALTOMARE, A.; CUOCCI, C.; GIACOVAZZO, C.; MOLITERNI, A.; RIZZI, R.; CORRIERO, N.; FALCICCHIO, A. EXPO2013 : a kit of tools for phasing crystal structures from powder data. *Journal of Applied Crystallography*, v. 46, n. 4, p. 1231–1235, 1 ago. 2013.

ANNI, M.; CRETÍ, A.; GIORGI, M. L. DE; LOMASCOLO, M. Local Morphology Effects on the Photoluminescence Properties of Thin $CsPbBr_3$ Nanocrystal Films. *Nanomaterials*, v. 11, n. 6, p. 1470, 1 jun. 2021.

ARUNAN, E. et al. Defining the hydrogen bond: An account (IUPAC Technical Report). *Pure and Applied Chemistry*, v. 83, n. 8, p. 1619–1636, 2011.

ARUNAN, E.; MANI, D. Dynamics of the chemical bond: Inter- and intra-molecular hydrogen bond. *Faraday Discussions*, v. 177, p. 51–64, 1 abr. 2015.

BAILEY, C. G.; GILLAN, L. V.; LEE, M.; SLOANE, N.; LIU, X.; SOUFIANI, A. M.; HAO, X.; MCCAMEY, D. R. Influence of Organic Spacer Cation on Dark Excitons in 2D Perovskites. 23 maio 2023.

BAO, J.; HADJIEV, V. G. Origin of Luminescent Centers and Edge States in Low-Dimensional Lead Halide Perovskites: Controversies, Challenges and Instructive Approaches. *Nano-Micro Letters*, v. 11, n. 1, 2019.

BATI, A. S. R.; ZHONG, Y. L.; BURN, P. L.; NAZEERUDDIN, M. K.; SHAW, P. E.; BATMUNKH, M. Next-generation applications for integrated perovskite solar cells. *Communications Materials*, v. 4, n. 1, p. 2, 5 jan. 2023.

BATOR, G.; ZEEGERS-HUYSKENS, T.; JAKUBAS, R.; ZALESKI, J. Structure and phase transitions in guanidinium halogenobismuthates(III). *Journal of Molecular Structure*, v. 570, n. 1–3, p. 61–74, ago. 2001.

BEHERA, R. K.; ADHIKARI, S. DAS; DUTTA, S. K.; DUTTA, A.; PRADHAN, N. Blue-Emitting $CsPbCl_3$ Nanocrystals: Impact of Surface Passivation for Unprecedented Enhancement and Loss of Optical Emission. *The Journal of Physical Chemistry Letters*, v. 9, n. 23, p. 6884–6891, 6 dez. 2018.

BELLA, F.; GRIFFINI, G.; CORREA-BAENA, J.-P.; SARACCO, G.; GRÄTZEL, M.; HAGFELDT, A.; TURRI, S.; GERBALDI, C. Improving efficiency and stability of perovskite solar cells with photocurable fluoropolymers. *Science*, v. 354, n. 6309, p. 203–206, 14 out. 2016.

BHAT, A. A.; KHANDY, S. A.; ISLAM, I.; TOMAR, R. Optical, electrochemical and photocatalytic properties of cobalt doped $CsPbCl_3$ nanostructures: a one-pot synthesis approach. *Scientific Reports*, v. 11, n. 1, p. 16473, 13 ago. 2021.

BIRCH, F. Finite Elastic Strain of Cubic Crystals. *Physical Review*, v. 71, n. 11, p. 809–824, 1947.

BORDALLO, H. N.; KOLESOV, B. A.; BOLDYREVA, E. V.; JURANYI, F. Different dynamics of chiral and racemic (L- and DL-) serine crystals: Evidenced by incoherent inelastic neutron and Raman scattering. *Journal of the American Chemical Society*, v. 129, n. 36, p. 10984–10985, 12 set. 2007.

BOULTIF, A.; LOUËR, D. Powder pattern indexing with the dichotomy method. *Journal of Applied Crystallography*, v. 37, n. 5, p. 724–731, out. 2004.

BROADHURST, E. T.; WILSON, C. J. G.; ZISSIMOU, G. A.; PADRÓN GÓMEZ, M. A.; VASCONCELOS, D. M. L.; CONSTANTINIDES, C. P.; KOUTENTIS, P. A.; AYALA, A. P.; PARSONS, S. The Effect of High Pressure on Polymorphs of a Derivative of Blatter's Radical: Identification of the Structural Signatures of Subtle Phase Transitions. *Crystal Growth and Design*, v. 23, n. 3, p. 1915–1924, 1 mar. 2023.

BROWN, I. D. Recent Developments in the Methods and Applications of the Bond Valence Model. *Chemical Reviews*, v. 109, n. 12, p. 6858–6919, 9 dez. 2009.

BROWN, I. D.; ALTERMATT, D. Bond-valence parameters obtained from a systematic analysis of the Inorganic Crystal Structure Database. *Acta Crystallographica Section B:* structural science, v. 41, n. 4, p. 244–247, 1 ago. 1985.

BURGER, S.; GROVER, S.; BUTLER, K. T.; BOSTRÖM, H. L. B.; GRAU-CRESPO, R.; KIESLICH, G. Tilt and shift polymorphism in molecular perovskites. *Materials Horizons*, v. 8, n. 9, p. 2444–2450, 1 set. 2021.

CAICEDO-DÁVILA, S.; CAPRIOGLIO, P.; LEHMANN, F.; LEVCENCO, S.; STOLTERFOHT, M.; NEHER, D.; KRONIK, L.; ABOU-RAS, D. Effects of Quantum and Dielectric Confinement on the Emission of Cs-Pb-Br Composites. *Advanced Functional Materials*, v. 2305240, p. 1–9, 12 jul. 2023.

CAO, F.; LI, L. Progress of Lead-Free Halide Perovskites: From Material Synthesis to Photodetector Application. *Advanced Functional Materials*, v. 31, n. 11, p. 2008275, 28 mar. 2021.

CAO, M.; DAMJI, Y.; ZHANG, C.; WU, L.; ZHONG, Q.; LI, P.; YANG, D.; XU, Y.; ZHANG, Q. Low-Dimensional-Networked Cesium Lead Halide Perovskites: Properties, Fabrication, and Applications. *Small Methods*, n. 2000303, p. 1–33, 2020.

CASTRO FERREIRA, W.; ARAÚJO, B. S.; GÓMEZ, M. A. P.; MEDEIROS, F. E. O.; ARAUJO PASCHOAL, C. W. DE; SILVA, C. B. DA; FREIRE, P. T. C.; KANEKO, U. F.; ARDITO, F. M.; SOUZA-NETO, N. M.; AYALA, A. P. Pressure-Induced Structural and Optical Transitions in Luminescent Bulk Cs 4 PbBr 6. *The Journal of Physical Chemistry C*, v. 126, n. 1, p. 541–550, 13 jan. 2022.

CHAN, T. H.; TAYLOR, N. T.; SUNDARAM, S.; HEPPLESTONE, S. P. Phase Stability and Electronic Properties of Hybrid Organic–Inorganic Perovskite Solid Solution (CH(NH2)2) x (CH3NH3)1– x Pb(Bry I1– y) $_3$ as a Function of Composition. *The Journal of Physical Chemistry C*, v. 126, n. 32, p. 13640–13648, 18 ago. 2022.

CHATTERJEE, S.; PAL, A. J. Influence of metal substitution on hybrid halide perovskites: towards lead-free perovskite solar cells. *Journal of Materials Chemistry A*, v. 6, n. 9, p. 3793–3823, 2018.

CHAVES, J. M.; FLORÊNCIO, O.; SILVA, P. S.; MARQUES, P. W. B.; SCHNEIDER, S. G. Anelastic relaxation associated to phase transformations and interstitial atoms in the Ti–35Nb–7Zr alloy. *Journal of Alloys and Compounds*, v. 616, p. 420–425, 15 dez. 2014.

CHEN, B.; CHEN, R.; HUANG, B. Strong Electron–Phonon Coupling Induced Self-Trapped Excitons in Double Halide Perovskites. *Advanced Energy and Sustainability Research*, 25 mar. 2023.

CHEN, X.; HAN, D.; SU, Y.; ZENG, Q.; LIU, L.; SHEN, D. Structural and Electronic Properties of Inorganic Mixed Halide Perovskites. physica status solidi (RRL) – *Rapid Research Letters*, v. 12, n. 8, p. 1800193, 28 ago. 2018.

CHEN, Y.; MOLOKEEV, M. S.; ATUCHIN, V. V.; RESHAK, A. H.; AULUCK, S.; ALAHMED, Z. A.; XIA, Z. Synthesis, Crystal Structure, and Optical Gap of Two-Dimensional Halide Solid Solutions $CsPb_2(Cl_{1-x}Br_x)_5$. *Inorganic Chemistry*, v. 57, n. 15, p. 9531–9537, 6 ago. 2018.

CHO, S.; YUN, S. H. Structure and optical properties of perovskite-embedded dual-phase microcrystals synthesized by sonochemistry. *Communications Chemistry*, v. 3, n. 1, 2020.

CHOUHAN, L.; GHIMIRE, S.; SUBRAHMANYAM, C.; MIYASAKA, T.; BIJU, V. Synthesis, optoelectronic properties and applications of halide perovskites. *Chemical Society Reviews*, v. 49, n. 10, p. 2869–2885, 21 maio 2020.

DOLOMANOV, O. V.; BOURHIS, L. J.; GILDEA, R. J.; HOWARD, J. A. K.; PUSCHMANN, H. OLEX2 : a complete structure solution, refinement and analysis program. *Journal of Applied Crystallography*, v. 42, n. 2, p. 339–341, 1 abr. 2009.

DRUSHLIAK, V.; SZAFRAŃSKI, M. Thermodynamic Stability, Structure, and Optical Properties of Perovskite-Related $CsPb_2Br_5$ Single Crystals under Pressure. *Inorganic Chemistry*, v. 61, n. 36, p. 14389–14396, 12 set. 2022.

DURSUN, I. et al. $CsPb_2Br_5$ Single Crystals: Synthesis and Characterization. *ChemSusChem*, v. 10, n. 19, p. 3746–3749, 9 out. 2017.

EL-MELLOUHI, F.; MARZOUK, A.; BENTRIA, E. T.; RASHKEEV, S. N.; KAIS, S.; ALHARBI, F. H. Hydrogen Bonding and Stability of Hybrid Organic–Inorganic Perovskites. *ChemSusChem*, v. 9, n. 18, p. 2648–2655, 22 set. 2016.

FANG, Z.; SUN, J.; LIU, S. F.; DING, L. Defects in perovskite crystals Defects in perovskite crystals. v. 44, n. 8, 2023.

FU, J.; RAMESH, S.; MELVIN LIM, J. W.; SUM, T. C. Carriers, Quasi-particles, and Collective Excitations in Halide Perovskites. *Chemical Reviews*, 5 jun. 2023.

GAO, Y. et al. Molecular engineering of organic–inorganic hybrid perovskites quantum wells. *Nature Chemistry*, v. 11, n. 12, p. 1151–1157, 11 dez. 2019.

GARCÍA-FERNÁNDEZ, A.; BERMÚDEZ-GARCÍA, J. M.; CASTRO-GARCÍA, S.; LLAMAS-SAIZ, A. L.; ARTIAGA, R.; LÓPEZ-BECEIRO, J. J.; SÁNCHEZ-ANDÚJAR, M.; SEÑARÍS-RODRÍGUEZ, M. A. [(CH3)2 NH2]7 Pb4X15 (X = Cl – and Br –), 2D-Perovskite Related Hybrids with Dielectric Transitions and Broadband Photoluminiscent Emission. *Inorganic Chemistry*, v. 57, n. 6, p. 3215–3222, 19 mar. 2018.

GHAITHAN, H. M.; ALAHMED, Z. A.; LYRAS, A.; QAID, S. M. H.; ALDWAYYAN, A. S. Computational investigation of the folded and unfolded band structure and structural and optical properties of $CsPb(I1{-}xBrx)_3$ perovskites. *Crystals*, v. 10, n. 5, p. 2–15, 2020.

GOODWIN, A. L.; KEEN, D. A.; TUCKER, M. G. Large negative linear compressibility of $Ag_3[Co(CN)_6]$. *Proceedings of the National Academy of Sciences*, v. 105, n. 48, p. 18708–18713, 2 dez. 2008.

GRANCINI, G.; NAZEERUDDIN, M. K. Dimensional tailoring of hybrid perovskites for photovoltaics. *Nature Reviews Materials*, v. 4, n. 1, p. 4–22, 28 nov. 2018.

GRECHKO, M.; BRETSCHNEIDER, S. A.; VIETZE, L.; KIM, H.; BONN, M. Vibrational Coupling between Organic and Inorganic Sublattices of Hybrid Perovskites. *Angewandte Chemie*, v. 130, n. 41, p. 13845–13849, 8 out. 2018.

GUAN, X.; LEI, Z.; YU, X.; LIN, C.; HUANG, J.; HUANG, C.; HU, L.; LI, F.; VINU, A.; YI, J.; WU, T. Low-Dimensional Metal-Halide Perovskites as High-Performance Materials for Memory Applications. *Small*, v. 18, n. 38, p. 2203311, 21 set. 2022.

HADI, A. et al. Melt-Processed Halide Perovskite Thin Films from a Two-Dimensional Ruddlesden–Popper Phase Precursor. *The Journal of Physical Chemistry Letters*, v. 14, n. 22, p. 5194–5202, 8 jun. 2023.

HADJIEV, V. G.; WANG, C.; WANG, Y.; SU, X.; CALDERON, H. A.; ROBLES HERNANDEZ, F.; WANG, Z. M.; BAO, J. M. Phonon fingerprints of $CsPb_2Br_5$. *Journal of Physics:* condensed matter, v. 30, n. 40, p. 405703, 10 out. 2018.

HAN, J. H.; SAMANTA, T.; PARK, Y. M.; CHO, H. BIN; MIN, J. W.; HWANG, S. J.; JANG, S. W.; IM, W. BIN. Effect of self-trapped excitons in the optical properties of manganese-alloyed hexagonal-phased metal halide perovskite. *Chemical Engineering Journal*, v. 450, 15 dez. 2022.

HAN, L.; WANG, P.; WANG, Z.; LIU, Y.; ZHENG, Z.; CHENG, H.; HUANG, B. Zero-dimensional hydrazine iodobismuthate as a lead-free perovskite-like light absorber in a self-powered photodetector. *Journal of Alloys and Compounds*, v. 893, p. 162347, fev. 2022.

HAUGHEY, D. P.; BEVERIDGE, G. S. G. Structural properties of packed beds - A review. *The Canadian Journal of Chemical Engineering*, v. 47, n. 2, p. 130–140, abr. 1969.

HOWARD, C. J.; STOKES, H. T. Group-Theoretical Analysis of Octahedral Tilting in Perovskites. *Acta Crystallographica Section B:* structural science, v. 54, n. 6, p. 782–789, 1 dez. 1998.

HU, J.; XIONG, X.; GUAN, W.; XIAO, Z.; TAN, C.; LONG, H. Durability engineering in all-inorganic $CsPbX_3$ perovskite solar cells: strategies and challenges. *Materials Today Chemistry*, v. 24, p. 100792, 2022.

HU, T.; SMITH, M. D.; DOHNER, E. R.; SHER, M.-J.; WU, X.; TRINH, M. T.; FISHER, A.; CORBETT, J.; ZHU, X.-Y.; KARUNADASA, H. I.; LINDENBERG, A. M. Mechanism for Broadband White-Light Emission from Two-Dimensional (110) Hybrid Perovskites. *The Journal of Physical Chemistry Letters*, v. 7, n. 12, p. 2258–2263, 16 jun. 2016.

HUANG, J.; YUAN, Y.; SHAO, Y.; YAN, Y. Understanding the physical properties of hybrid perovskites for photovoltaic applications. *Nature Reviews Materials*, v. 2, 2017.

HUANG, Z.-P.; MA, B.; WANG, H.; LI, N.; LIU, R.-T.; ZHANG, Z.-Q.; ZHANG, X.-D.; ZHAO, J.-H.; ZHENG, P.-Z.; WANG, Q.; ZHANG, H.-L. In Situ Growth of 3D/2D

($CsPbBr_3$ /$CsPb_2Br_5$) Perovskite Heterojunctions toward Optoelectronic Devices. *The Journal of Physical Chemistry Letters*, v. 11, n. 15, p. 6007–6015, 6 ago. 2020.

IARU, C. M. et al. Fröhlich interaction dominated by a single phonon mode in $CsPbBr_3$. *Nature Communications*, v. 12, n. 1, p. 5844, 6 out. 2021.

IVANOVSKA, T.; QUARTI, C.; GRANCINI, G.; PETROZZA, A.; ANGELIS, F. DE; MILANI, A.; RUANI, G. Vibrational Response of Methylammonium Lead Iodide: From Cation Dynamics to Phonon–Phonon Interactions. *ChemSusChem*, v. 9, n. 20, p. 2994–3004, 20 out. 2016.

JENA, A. K.; KULKARNI, A.; MIYASAKA, T. Halide Perovskite Photovoltaics: Background, Status, and Future Prospects. *Chemical Reviews*, v. 119, n. 5, p. 3036–3103, 13 mar. 2019.

JIN, S. Can We Find the Perfect A-Cations for Halide Perovskites? *ACS Energy Letters*, v. 6, n. 9, p. 3386–3389, 10 set. 2021.

KATAN, C.; PEDESSEAU, L.; KEPENEKIAN, M.; ROLLAND, A.; EVEN, J. Interplay of spin–orbit coupling and lattice distortion in metal substituted 3D tri-chloride hybrid perovskites. *Journal of Materials Chemistry A*, v. 3, n. 17, p. 9232–9240, 2015.

KE, W.; KANATZIDIS, M. G. Prospects for low-toxicity lead-free perovskite solar cells. *Nature Communications*, v. 10, n. 1, p. 965, 27 fev. 2019.

KIM, B.; KIM, M.; KIM, H.; JEONG, S.; YANG, J.; JEONG, M. S. Improved Stability of $MAPbI_3$ Perovskite Solar Cells Using Two-Dimensional Transition-Metal Dichalcogenide Interlayers. *ACS Applied Materials & Interfaces*, v. 14, n. 31, p. 35726–35733, 10 ago. 2022.

KIM, H.; HAN, J. S.; CHOI, J.; KIM, S. Y.; JANG, H. W. Halide Perovskites for Applications beyond Photovoltaics. *Small Methods*, v. 2, n. 3, p. 1700310, mar. 2018.

KLEMENT, P.; DEHNHARDT, N.; DONG, C. D.; DOBENER, F.; BAYLIFF, S.; WINKLER, J.; HOFMANN, D. M.; KLAR, P. J.; SCHUMACHER, S.; CHATTERJEE, S.; HEINE, J. Atomically Thin Sheets of Lead-Free 1D Hybrid Perovskites Feature Tunable White-Light Emission from Self-Trapped Excitons. *Advanced Materials*, v. 33, n. 23, 1 jun. 2021.

KOSTOPOULOU, A.; KONIDAKIS, I.; STRATAKIS, E. Two-dimensional metal halide perovskites and their heterostructures: from synthesis to applications. *Nanophotonics*, v. 12, n. 9, p. 1643–1710, 28 abr. 2023.

KRAUSE, L.; HERBST-IRMER, R.; SHELDRICK, G. M.; STALKE, D. Comparison of silver and molybdenum microfocus X-ray sources for single-crystal structure determination. *Journal of Applied Crystallography*, v. 48, n. 1, p. 3–10, 1 fev. 2015.

KROUMOVA, E.; AROYO, M. L.; PEREZ-MATO, J. M.; KIROV, A.; CAPILLAS, C.; IVANTCHEV, S.; WONDRATSCHEK, H. Bilbao Crystallographic Server: Useful

databases and tools for phase-transition studies. *Phase Transitions*, v. 76, n. 1–2, p. 155–170, 1 jan. 2003.

LA FLOR, G. DE; OROBENGOA, D.; TASCI, E.; PEREZ-MATO, J. M.; AROYO, M. I. Comparison of structures applying the tools available at the Bilbao Crystallographic Server. *Journal of Applied Crystallography*, v. 49, p. 653–664, 2016.

LANGE, R. Z.; SYNNATSCHKE, K.; QI, H.; HUBER, N.; HOFER, G.; LIANG, B.; HUCK, C.; PUCCI, A.; KAISER, U.; BACKES, C.; SCHLÜTER, A. D. Enriching and Quantifying Porous Single Layer 2D Polymers by Exfoliation of Chemically Modified van der Waals Crystals. *Angewandte Chemie:* International Edition, v. 59, n. 14, p. 5683–5695, 2020.

LE, Q. VAN; LEE, J. W.; SOHN, W.; JANG, H. W.; KIM, J. K.; KIM, S. Y. Low Temperature Solution-Processable Cesium Lead Bromide Microcrystals for Light Conversion. *Crystal Growth and Design*, v. 18, n. 5, p. 3161–3166, 2018.

LEE, Y.; MITZI, D. B.; BARNES, P. W.; VOGT, T. Pressure-induced phase transitions and templating effect in three-dimensional organic-inorganic hybrid perovskites. *Physical Review B* - Condensed Matter and Materials Physics, v. 68, n. 2, 2003.

LEGUY, A. M. A. et al. Dynamic disorder, phonon lifetimes, and the assignment of modes to the vibrational spectra of methylammonium lead halide perovskites. *Physical Chemistry Chemical Physics*, v. 18, n. 39, p. 27051–27066, 2016.

LI, C.; WANG, HAILU; WANG, F.; LI, T.; XU, M.; WANG, HAO; WANG, Z.; ZHAN, X.; HU, W.; SHEN, L. Ultrafast and broadband photodetectors based on a perovskite/organic bulk heterojunction for large-dynamic-range imaging. *Light:* Science & Applications, v. 9, n. 1, p. 31, 3 mar. 2020.

LI, G.; WANG, H.; ZHU, Z.; CHANG, Y.; ZHANG, T.; SONG, Z.; JIANG, Y. Shape and phase evolution from $CsPbBr_3$ perovskite nanocubes to tetragonal $CsPb_2Br_5$ nanosheets with an indirect bandgap. *Chemical Communications*, v. 52, n. 75, p. 11296–11299, 2016.

LI, J.; LU, G.; XIE, H.; JIANG, X.; FANG, Z.; ZENG, Y.-J.; HE, H.; YE, Z. Effect of Electron–Phonon Coupling on the Color Purity of Two-Dimensional Ruddlesden–Popper Hybrid Lead Iodide Perovskites. *The Journal of Physical Chemistry C*, v. 127, n. 13, p. 6380–6388, 6 abr. 2023.

LI, J.; WANG, H.; LI, D. Self-trapped excitons in two-dimensional perovskites. *Frontiers of Optoelectronics*, v. 13, n. 3, p. 225–234, 27 set. 2020.

LI, J.; ZHANG, H.; WANG, S.; LONG, D.; LI, M.; GUO, Y.; ZHONG, Z.; WU, K.; WANG, D.; ZHANG, T. Synthesis of all-inorganic $CsPb_2Br_5$ perovskite and determination of its luminescence mechanism. *RSC Advances*, v. 7, n. 85, p. 54002–54007, 2017.

LI, M. et al. Perovskite $Cs_3Bi_2I_9$ Hexagonal Prisms with Ordered Geometry for Enhanced Photocatalytic Hydrogen Evolution. *ACS Energy Letters*, v. 7, n. 10, p. 3370–3377, 14 out. 2022.

LI, M. et al. Synthesis of Two-Dimensional $CsPb_2X_5$ (X = Br and I) with a Stable Structure and Tunable Bandgap by $CsPbX_3$ Phase Separation. *The Journal of Physical Chemistry Letters*, v. 13, n. 11, p. 2555–2562, 24 mar. 2022.

LI, M.; ZHANG, X.; DU, Y.; YANG, P. Colloidal $CsPbX_3$ (X = Br, I, Cl) NCs: Morphology controlling, composition evolution, and photoluminescence shift. *Journal of Luminescence*, v. 190, n. December 2016, p. 397–402, 2017.

LI, P.; CHENG, Y.; ZHOU, L.; YU, X.; JIANG, J.; HE, M.; LIANG, X.; XIANG, W. Photoluminescence properties and device application of $CsPb_2Br_5$ quantum dots in glasses. *Materials Research Bulletin*, v. 105, p. 63–67, set. 2018.

LI, P.; HU, C.; ZHOU, L.; JIANG, J.; CHENG, Y.; HE, M.; LIANG, X.; XIANG, W. Novel synthesis and optical characterization of $CsPb_2Br_5$ quantum dots in borosilicate glasses. *Materials Letters*, v. 209, p. 483–485, 2017.

LI, Q.; CHEN, Z.; YANG, B.; TAN, L.; XU, B.; HAN, J.; ZHAO, Y.; TANG, J.; QUAN, Z. Pressure-Induced Remarkable Enhancement of Self-Trapped Exciton Emission in One-Dimensional $CsCu_2I_3$ with Tetrahedral Units. *Journal of the American Chemical Society*, v. 142, n. 4, p. 1786–1791, 29 jan. 2020.

LI, S.; LUO, J.; LIU, J.; TANG, J. Self-Trapped Excitons in All-Inorganic Halide Perovskites: Fundamentals, Status, and Potential Applications. *The Journal of Physical Chemistry Letters*, v. 10, n. 8, p. 1999–2007, 18 abr. 2019.

LI, Z.; KLEIN, T. R.; KIM, D. H.; YANG, M.; BERRY, J. J.; HEST, M. F. A. M. VAN; ZHU, K. Scalable fabrication of perovskite solar cells. *Nature Reviews Materials*, v. 3, p. 1–20, 2018.

LIN, C.-F.; HUANG, K.-W.; CHEN, Y.-T.; HSUEH, S.-L.; LI, M.-H.; CHEN, P. Perovskite-Based X-ray Detectors. *Nanomaterials*, v. 13, n. 13, p. 2024, 7 jul. 2023.

LIN, H.; ZHOU, C.; TIAN, Y.; SIEGRIST, T.; MA, B. Low-Dimensional Organometal Halide Perovskites. *ACS Energy Letters*, v. 3, n. 1, p. 54–62, 2018.

LIN, M.; DHANABALAN, B.; BIFFI, G.; LENG, Y.; KUTKAN, S.; ARCINIEGAS, M. P.; TAN, P.; KRAHNE, R. Correlating Symmetries of Low-Frequency Vibrations and Self-Trapped Excitons in Layered Perovskites for Light Emission with Different Colors. *Small*, v. 18, n. 15, p. 2106759, 26 abr. 2022.

LINABURG, M. R.; MCCLURE, E. T.; MAJHER, J. D.; WOODWARD, P. M. $Cs_{1-x}Rb_xPbCl_3$ and $Cs_{1-x}Rb_xPbBr_3$ Solid Solutions: Understanding Octahedral Tilting in Lead Halide Perovskites. *Chemistry of Materials*, v. 29, n. 8, p. 3507–3514, 25 abr. 2017.

LIU, G.; KONG, L.; GONG, J.; YANG, W.; MAO, H. K.; HU, Q.; LIU, Z.; SCHALLER, R. D.; ZHANG, D.; XU, T. Pressure-Induced Bandgap Optimization in Lead-Based

Perovskites with Prolonged Carrier Lifetime and Ambient Retainability. *Advanced Functional Materials*, v. 27, n. 3, 19 jan. 2017.

LIU, J.; CHEN, K.; KHAN, S. A.; SHABBIR, B.; ZHANG, Y.; KHAN, Q.; BAO, Q. Synthesis and optical applications of low dimensional metal-halide perovskites. *Nanotechnology*, v. 31, n. 15, p. 152002, 10 abr. 2020.

LIU, S.; DU, Y. W.; TSO, C. Y.; LEE, H. H.; CHENG, R.; FENG, S. P.; YU, K. M. Organic Hybrid Perovskite (MAPbI3−xClx) for Thermochromic Smart Window with Strong Optical Regulation Ability, Low Transition Temperature, and Narrow Hysteresis Width. *Advanced Functional Materials*, v. 31, n. 26, 1 jun. 2021.

LIU, X.; GAO, X.; XIONG, L.; LI, S.; ZHANG, Y.; LI, Q.; JIANG, H.; XU, D. A-site coordinating cation engineering in zero-dimensional antimony halide perovskites for strong self-trapped exciton emission. *SmartMat*, 4 jul. 2023.

LIU, X.-K.; XU, W.; BAI, S.; JIN, Y.; WANG, J.; FRIEND, R. H.; GAO, F. Metal halide perovskites for light-emitting diodes. *Nature Materials*, v. 20, n. 1, p. 10–21, 14 jan. 2021.

LU, H. et al. Electronic Impurity Doping of a 2D Hybrid Lead Iodide Perovskite by PRX *Energy*, v. 2, n. 2, p. 023010, 8 jun. 2023.

LUFASO, M. W.; WOODWARD, P. M. Jahn-Teller distortions, cation ordering and octahedral tilting in perovskites. *Acta Crystallographica Section B:* structural science, v. 60, n. 1, p. 10–20, fev. 2004.

LUO, J. et al. Efficient and stable emission of warm-white light from lead-free halide double perovskites. *Nature*, v. 563, n. 7732, p. 541–545, 7 nov. 2018.

MA, Z.; LI, F.; QI, G.; WANG, L.; LIU, C.; WANG, K.; XIAO, G.; ZOU, B. Structural stability and optical properties of two-dimensional perovskite-like $CsPb_2Br_5$ microplates in response to pressure. *Nanoscale*, v. 11, n. 3, p. 820–825, 21 jan. 2019.

MACRAE, C. F.; SOVAGO, I.; COTTRELL, S. J.; GALEK, P. T. A.; MCCABE, P.; PIDCOCK, E.; PLATINGS, M.; SHIELDS, G. P.; STEVENS, J. S.; TOWLER, M.; WOOD, P. A. Mercury 4.0 : from visualization to analysis, design and prediction. *Journal of Applied Crystallography*, v. 53, n. 1, p. 226–235, 1 fev. 2020.

MAITY, G.; PRADHAN, S. K. Composition related structural transition between mechanosynthesized $CsPbBr_3$ and $CsPb_2Br_5$ perovskites and their optical properties. *Journal of Alloys and Compounds*, v. 816, p. 152612, mar. 2020.

MCCALL, K. M.; STOUMPOS, C. C.; KOSTINA, S. S.; KANATZIDIS, M. G.; WESSELS, B. W. Strong Electron-Phonon Coupling and Self-Trapped Excitons in the Defect Halide Perovskites $A_3M_2I_9$ (A = Cs, Rb; M = Bi, Sb). *Chemistry of Materials*, v. 29, n. 9, p. 4129–4145, 9 maio 2017.

MCCLURE, E. T.; BALL, M. R.; WINDL, W.; WOODWARD, P. M. Cs_2AgBiX_6 (X = Br, Cl): New Visible Light Absorbing, Lead-Free Halide Perovskite Semiconductors. *Chemistry of Materials*, v. 28, n. 5, p. 1348–1354, 8 mar. 2016.

MCGEHEE, M. D. Fast-track solar cells. *Nature*, v. 501, n. 7467, p. 323–325, 2013.

MENAHEM, M.; DAI, Z.; AHARON, S.; SHARMA, R.; ASHER, M.; DISKIN-POSNER, Y.; KOROBKO, R.; RAPPE, A. M.; YAFFE, O. Strongly Anharmonic Octahedral Tilting in Two-Dimensional Hybrid Halide Perovskites. *ACS Nano*, v. 15, n. 6, p. 10153–10162, 22 jun. 2021.

MENG, L.; YOU, J.; YANG, Y. Addressing the stability issue of perovskite solar cells for commercial applications. *Nature Communications*, v. 9, n. 1, p. 5265, 10 dez. 2018.

MOMMA, K.; IZUMI, F. VESTA 3 for three-dimensional visualization of crystal, volumetric and morphology data. *Journal of Applied Crystallography*, v. 44, n. 6, p. 1272–1276, 2011.

NIE, T.; FANG, Z.; REN, X.; DUAN, Y.; LIU, S. Recent Advances in Wide-Bandgap Organic–Inorganic Halide Perovskite Solar Cells and Tandem Application. *Nano-Micro Letters*, v. 15, n. 1, p. 70, 21 dez. 2023.

OCTAVIO DE ARAUJO, L.; RÊGO, C. R. C.; WENZEL, W.; SABINO, F. P.; GUEDES-SOBRINHO, D. Impact of the Polymorphism and Relativistic Effects on the Electronic Properties of Inorganic Metal Halide Perovskites. *The Journal of Physical Chemistry C*, v. 126, n. 4, p. 2131–2140, 3 fev. 2022.

PAN, F.; LI, J.; MA, X.; NIE, Y.; LIU, B.; YE, H. Free and self-trapped exciton emission in perovskite $CsPbBr_3$ microcrystals. *RSC Advances*, v. 12, n. 2, p. 1035–1042, 5 jan. 2022.

PARK, B.-W.; PHILIPPE, B.; ZHANG, X.; RENSMO, H.; BOSCHLOO, G.; JOHANSSON, E. M. J. Bismuth Based Hybrid Perovskites A_3BiI_9 (A: Methylammonium or Cesium) for Solar Cell Application. *Advanced Materials*, v. 27, n. 43, p. 6806–6813, 18 nov. 2015.

PETERS, J. A.; LIU, Z.; BULGIN, O.; HE, Y.; KLEPOV, V. V.; SIENA, M. C. DE; KANATZIDIS, M. G.; WESSELS, B. W. Excitons in $CsPbBr_3$ Halide Perovskite. *The Journal of Physical Chemistry Letters*, v. 12, n. 38, p. 9301–9307, 30 set. 2021.

PROTESESCU, L.; YAKUNIN, S.; BODNARCHUK, M. I.; KRIEG, F.; CAPUTO, R.; HENDON, C. H.; YANG, R. X.; WALSH, A.; KOVALENKO, M. V. Nanocrystals of Cesium Lead Halide Perovskites ($CsPbX_3$, X = Cl, Br, and I): Novel Optoelectronic Materials Showing Bright Emission with Wide Color Gamut. *Nano Letters*, v. 15, n. 6, p. 3692–3696, 2015.

QIN, C.; MATSUSHIMA, T.; SANDANAYAKA, A. S. D.; TSUCHIYA, Y.; ADACHI, C. Centrifugal-Coated Quasi-Two-Dimensional Perovskite $CsPb_2Br_5$ Films for Efficient

and Stable Light-Emitting Diodes. *Journal of Physical Chemistry Letters*, v. 8, n. 21, p. 5415–5421, 2017.

QIN, J.-P.; PAN, C.-Y. Synthesis, structure and optical properties of (H2DMAPA)$BiBr_5$, (H2DMAPA)BiBr2I_3, (H2DMAPA)2$AgBiBr_8$ and (H2EP)2$AgBiBr_8$ lead-free perovskites. *Journal of Solid State Chemistry*, v. 322, p. 123938, jun. 2023.

RAJPUT, P. K.; POONIA, A. K.; MUKHERJEE, S.; SHEIKH, T.; SHRIVASTAVA, M.; ADARSH, K. V.; NAG, A. Chiral Methylbenzylammonium Bismuth Iodide with Zero-Dimensional Perovskite Derivative Structure. *The Journal of Physical Chemistry C*, v. 126, n. 23, p. 9889–9897, 16 jun. 2022.

RAKITA, Y.; COHEN, S. R.; KEDEM, N. K.; HODES, G.; CAHEN, D. Mechanical properties of APbX3 (A = Cs or CH3NH3; X= I or Br) perovskite single crystals. *MRS Communications*, v. 5, n. 4, p. 623–629, 1 dez. 2015.

RODRÍGUEZ-HERNÁNDEZ, J. S.; MAYRA, M. A.; ABREU, D. S.; NONATO, A.; SILVA, R. X. DA; GARCÍA-FERNÁNDEZ, A.; SEÑARÍS-RODRÍGUEZ, M. A.; SÁNCHEZ-ANDÚJAR, M.; AYALA, A. P.; PASCHOAL, C. W. A. Uniaxial negative thermal expansion in the $[(CH_3)_2NH_2]PbBr_3$ hybrid perovskite. *Journal of Materials Chemistry C*, v. 10, n. 46, p. 17567–17576, 17 out. 2022.

RONG, Y.; HU, Y.; MEI, A.; TAN, H.; SAIDAMINOV, M. I.; SEOK, S. IL; MCGEHEE, M. D.; SARGENT, E. H.; HAN, H. Challenges for commercializing perovskite solar cells. *Science*, v. 361, n. 6408, 21 set. 2018.

ROUSSEAU, D. L.; BAUMAN, R. P.; PORTO, S. P. S. Normal Mode Determination in Crystals. *Journal of Raman Spectroscopy*, v. 10, p. 253–290, 1981.

ROY, A.; ULLAH, H.; GHOSH, A.; BAIG, H.; SUNDARAM, S.; TAHIR, A. A.; MALLICK, T. K. Understanding the Semi-Switchable Thermochromic Behavior of Mixed Halide Hybrid Perovskite Nanorods. *Journal of Physical Chemistry C*, v. 125, n. 32, p. 18058–18070, 19 ago. 2021.

RUAN, L.; SHEN, W.; WANG, A.; XIANG, A.; DENG, Z. Alkyl-Thiol Ligand-Induced Shape- and Crystalline Phase-Controlled Synthesis of Stable Perovskite-Related $CsPb_2Br_5$ Nanocrystals at Room Temperature. *The Journal of Physical Chemistry Letters*, v. 8, n. 16, p. 3853–3860, 17 ago. 2017.

SAHOO, A.; PAUL, T.; MAITI, S.; BANERJEE, R. Temperature-dependent Dielectric Properties of $CsPb_2Br_5$: A 2D Inorganic Halide Perovskite. *Nanotechnology*, v. 33, n. 195703, 2022.

SAMET, A.; BOUGHZALA, H.; KHEMAKHEM, H.; ABID, Y. Synthesis, characterization and non-linear optical properties of Tetrakis(dimethylammonium) Bromide Hexabromobismuthate: {[(CH3)2NH2]+}4·Br−·[BiBr6]3−. *Journal of Molecular Structure*, v. 984, n. 1–3, p. 23–29, 15 dez. 2010.

SATA, N.; SHEN, G.; RIVERS, M. L.; SUTTON, S. R. Pressure-volume equation of state of the high-pressure phase of NaCl. *Physical Review B*, v. 65, n. 10, p. 104114, 4 mar. 2002.

SCHMIDT-MENDE, L. et al. Roadmap on organic–inorganic hybrid perovskite semiconductors and devices. *APL Materials*, v. 9, n. 10, p. 109202, 1 out. 2021.

SCHRYVER, S.; LAMICHHANE, A. Temperature-driven structural phase transitions in CsPbBr. *Solid State Communications*, p. 115237, jun. 2023.

SHAMSI, J.; URBAN, A. S.; IMRAN, M.; TRIZIO, L. DE; MANNA, L. Metal Halide Perovskite Nanocrystals: Synthesis, Post-Synthesis Modifications, and Their Optical Properties. *Chemical Reviews*, v. 119, n. 5, p. 3296–3348, 2019.

SHELDRICK, G. M. A short history of SHELX. *Acta Crystallographica Section A*: foundations of crystallography, v. 64, n. 1, p. 112–122, 2008.

SHEN, G. et al. Toward an international practical pressure scale: A proposal for an IPPS ruby gauge (IPPS-Ruby2020). *High Pressure Research*, v. 40, n. 3, p. 299–314, 2 jul. 2020.

SHEN, Y.; YIN, J.; CAI, B.; WANG, Z.; DONG, Y.; XU, X.; ZENG, H. Lead-free, stable, high-efficiency (52%) blue luminescent $FA_3Bi_2Br_9$ perovskite quantum dots. *Nanoscale Horizons*, v. 5, n. 3, p. 580–585, 1 mar. 2020.

SHENG-ZHI, H. A New Approach to Bond Valence Parameters for Pb(II)—halide Bonds. *Acta Physico-Chimica Sinica*, v. 23, n. 05, p. 786–789, 2007.

SHI, Y.; ZHAO, W.; MA, Z.; XIAO, G.; ZOU, B. Self-trapped exciton emission and piezochromism in conventional 3D lead bromide perovskite nanocrystals under high pressure. *Chemical Science*, v. 12, n. 44, p. 14711–14717, 28 nov. 2021.

SHI, Z.; GUO, J.; CHEN, Y.; LI, Q.; PAN, Y.; ZHANG, H.; XIA, Y.; HUANG, W. Lead-Free Organic-Inorganic Hybrid Perovskites for Photovoltaic Applications: Recent Advances and Perspectives. *Advanced Materials*, v. 29, n. 16, p. 1605005, 25 abr. 2017.

SICHERT, J. A. et al. Quantum Size Effect in Organometal Halide Perovskite Nanoplatelets. *Nano Letters*, v. 15, n. 10, p. 6521–6527, 14 out. 2015.

SMITH, M. D.; KARUNADASA, H. I. White-Light Emission from Layered Halide Perovskites. *Accounts of Chemical Research*, v. 51, n. 3, p. 619–627, 20 mar. 2018.

SOLOZHENKO, V. L.; KURAKEVYCH, O. O.; SOLOZHENKO, E. G.; CHEN, J.; PARISE, J. B. Equation of state of graphite-like BC. *Solid State Communications*, v. 137, n. 5, p. 268–271, fev. 2006.

SONG, J.; LI, J.; LI, X.; XU, L.; DONG, Y.; ZENG, H. Quantum Dot Light-Emitting Diodes Based on Inorganic Perovskite Cesium Lead Halides ($CsPbX_3$). *Advanced Materials*, v. 27, n. 44, p. 7162–7167, 1 nov. 2015.

SONG, W.; QI, G.; LIU, B. Halide perovskite quantum dots for photocatalytic CO_2 reduction. *Journal of Materials Chemistry A*, v. 11, n. 24, p. 12482–12498, 2023.

STEELE, J. A.; LAI, M.; ZHANG, Y.; LIN, Z.; HOFKENS, J.; ROEFFAERS, M. B. J.; YANG, P. Phase Transitions and Anion Exchange in All-Inorganic Halide Perovskites. *Accounts of Materials Research*, v. 1, n. 1, p. 3–15, 23 out. 2020.

STEFANSKI, M.; PTAK, M.; SIERADZKI, A.; STREK, W. Optical characterization of Yb3+:$CsPbCl_3$ perovskite powder. *Chemical Engineering Journal*, v. 408, p. 127347, 15 mar. 2021.

STØLEN, S.; GRZECHNIK, A.; GRANDE, T.; MEZOUAR, M. Anisotropic compressibility and expansivity in layered $GeSe_2$. *Solid State Communications*, v. 115, n. 5, p. 249–252, jun. 2000.

STRANKS, S. D.; SNAITH, H. J. Metal-halide perovskites for photovoltaic and light-emitting devices. *Nature Nanotechnology*, v. 10, n. 5, p. 391–402, 7 maio 2015.

SUN, S.; FANG, Y.; KIESLICH, G.; WHITE, T. J.; CHEETHAM, A. K. Mechanical properties of organic–inorganic halide perovskites, $CH_3NH_3PbX_3$ (X = I, Br and Cl), by nanoindentation. *Journal of Materials Chemistry A*, v. 3, n. 36, p. 18450–18455, 5 ago. 2015.

SVANE, K. L.; FORSE, A. C.; GREY, C. P.; KIESLICH, G.; CHEETHAM, A. K.; WALSH, A.; BUTLER, K. T. How Strong Is the Hydrogen Bond in Hybrid Perovskites? *Journal of Physical Chemistry Letters*, v. 8, n. 24, p. 6154–6159, 21 dez. 2017.

SZAFRAŃSKI, M.; KATRUSIAK, A.; STÅHL, K. Time-dependent transformation routes of perovskites $CsPbBr_3$ and $CsPbCl_3$ under high pressure. *Journal of Materials Chemistry A*, v. 9, n. 17, p. 10769–10779, 7 maio 2021.

TAN, Y.; LI, R.; XU, H.; QIN, Y.; SONG, T.; SUN, B. Ultrastable and Reversible Fluorescent Perovskite Films Used for Flexible Instantaneous Display. *Advanced Functional Materials*, v. 29, n. 23, p. 1900730, jun. 2019.

TANG, X.; CHEN, M.; JIANG, L.; LI, M.; TANG, G.; LIU, H. Improvements in Efficiency and Stability of Perovskite Solar Cells Using a Cesium Chloride Additive. *ACS Applied Materials & Interfaces*, v. 14, n. 23, p. 26866–26872, 15 jun. 2022.

TANG, X.; HAN, S.; ZU, Z.; HU, W.; ZHOU, D.; DU, J.; HU, Z.; LI, S.; ZANG, Z. All-Inorganic Perovskite $CsPb_2Br_5$ Microsheets for Photodetector Application. *Frontiers in Physics*, v. 5, n. JAN, p. 1–7, 5 jan. 2018.

TEDESCO, C.; MALAVASI, L. Bismuth-Based Halide Perovskites for Photocatalytic H_2 Evolution Application. *Molecules*, v. 28, n. 1, p. 339, 1 jan. 2023.

TU, Q.; KIM, D.; SHYIKH, M.; KANATZIDIS, M. G. Mechanics-coupled stability of metal-halide perovskites. *Matter*, v. 4, n. 9, p. 2765–2809, 1 set. 2021.

TU, Q.; SPANOPOULOS, I.; HAO, S.; WOLVERTON, C.; KANATZIDIS, M. G.; SHEKHAWAT, G. S.; DRAVID, V. P. Out-of-Plane Mechanical Properties of 2D Hybrid Organic–Inorganic Perovskites by Nanoindentation. *ACS Applied Materials & Interfaces*, v. 10, n. 26, p. 22167–22173, 5 jul. 2018.

ULLAH, S.; WANG, J.; YANG, P.; LIU, L.; YANG, S.-E.; XIA, T.; GUO, H.; CHEN, Y. All-inorganic $CsPbBr_3$ perovskite: a promising choice for photovoltaics. *Materials Advances*, v. 2, n. 2, p. 646–683, 21 jan. 2021.

WANG, K.-H.; WU, L.; LI, L.; YAO, H.-B.; QIAN, H.-S.; YU, S.-H. Large-Scale Synthesis of Highly Luminescent Perovskite-Related $CsPb_2Br_5$ Nanoplatelets and Their Fast Anion Exchange. *Angewandte Chemie*, v. 128, n. 29, p. 8468–8472, 11 jul. 2016.

WANG, X.; ZHANG, T.; LOU, Y.; ZHAO, Y. All-inorganic lead-free perovskites for optoelectronic applications. *Materials Chemistry Frontiers*, v. 3, n. 3, p. 365–375, 1 mar. 2019.

WANG, Y. P.; LI, H. C.; HUANG, Y. C.; TAN, C. S. Synthesis and Applications of Halide Perovskite Nanocrystals in Optoelectronics. *Inorganics*, v. 11, n. 1, p. 39, 11 jan. 2023.

WANG, Y.; HE, C.; TAN, Q.; TANG, Z.; HUANG, L.; LIU, L.; YIN, J.; JIANG, Y.; WANG, X.; PAN, A. Exciton–phonon coupling in two-dimensional layered $(BA)_2$ PbI_4 perovskite microplates. *RSC Advances*, v. 13, n. 9, p. 5893–5899, 2023.

WANG, Y.; LI, D.; CHAO, L.; NIU, T.; CHEN, Y.; HUANG, W. Perovskite photodetectors for flexible electronics: Recent advances and perspectives. *Applied Materials Today*, v. 28, p. 101509, 1 ago. 2022.

WHALLEY, L. D.; GERWEN, P. VAN; FROST, J. M.; KIM, S.; HOOD, S. N.; WALSH, A. Giant Huang-Rhys Factor for Electron Capture by the Iodine Intersitial in Perovskite Solar Cells. *Journal of the American Chemical Society*, v. 143, n. 24, p. 9123–9128, 23 jun. 2021.

WOJDYR, M. Fityk : a general-purpose peak fitting program. *Journal of Applied Crystallography*, v. 43, n. 5, p. 1126–1128, 1 out. 2010.

WU, D.; ZHAO, X.; HUANG, Y.; LAI, J.; LI, H.; YANG, J.; TIAN, C.; HE, P.; HUANG, Q.; TANG, X. Lead-Free Perovskite Cs_2AgBiX_6 Nanocrystals with a Band Gap Funnel Structure for Photocatalytic CO_2 Reduction under Visible Light. *Chemistry of Materials*, v. 33, n. 13, p. 4971–4976, 13 jul. 2021.

WU, Y.; QIU, L.; LIU, J.; GUAN, M.; DAI, Z.; LI, G. Narrow Bandgap Metal Halide Perovskites: Synthesis, Characterization, and Optoelectronic Applications. *Advanced Optical Materials*, v. 10, n. 11, p. 2102661, 5 jun. 2022.

WU, Z.; TÜYSÜZ, H.; BESENBACHER, F.; DAI, Y.; XIONG, Y. Recent developments in lead-free bismuth-based halide perovskite nanomaterials for heterogeneous photocatalysis under visible light. *Nanoscale*, v. 15, n. 12, p. 5598–5622, 2023.

XIAO, Z.; SONG, Z.; YAN, Y. From Lead Halide Perovskites to Lead-Free Metal Halide Perovskites and Perovskite Derivatives. *Advanced Materials*, v. 31, n. 47, p. 1803792, 24 nov. 2019.

XU, H.; ZHANG, Z.; DONG, X.; HUANG, L.; ZENG, H.; LIN, Z.; ZOU, G. Corrugated 1D Hybrid Metal Halide $[C_6H_7ClN]CdCl_3$ Exhibiting Broadband White-Light Emission. *Inorganic Chemistry*, v. 61, n. 11, p. 4752–4759, 21 mar. 2022.

XU, K.-X.; LAI, J.-M.; GAO, Y.-F.; SONG, F.; SUN, Y.-J.; TAN, P.-H.; ZHANG, J. High-order Raman scattering mediated by self-trapped exciton in halide double perovskite. *Physical Review B*, v. 106, n. 8, p. 085205, 22 ago. 2022.

XU, Z.; JIANG, X.; CAI, H.; CHEN, K.; YAO, X.; FENG, Y. Toward a General Understanding of Exciton Self-Trapping in Metal Halide Perovskites. *The Journal of Physical Chemistry Letters*, v. 12, n. 43, p. 10472–10478, 4 nov. 2021.

YAKUNIN, S.; PROTESESCU, L.; KRIEG, F.; BODNARCHUK, M. I.; NEDELCU, G.; HUMER, M.; LUCA, G. DE; FIEBIG, M.; HEISS, W.; KOVALENKO, M. V. Low-threshold amplified spontaneous emission and lasing from colloidal nanocrystals of caesium lead halide perovskites. *Nature Communications*, v. 6, 2015.

YAN, J.; LI, H.; ALDAMASY, M. H.; FRASCA, C.; ABATE, A.; ZHAO, K.; HU, Y. Advances in the Synthesis of Halide Perovskite Single Crystals for Optoelectronic Applications. *Chemistry of Materials*, v. 35, n. 7, p. 2683–2712, 11 abr. 2023.

YANGUI, A. et al. Optical Investigation of Broadband White-Light Emission in Self-Assembled Organic-Inorganic Perovskite $(C_6H_{11}NH_3)_2PbBr_4$. *Journal of Physical Chemistry C*, 2015.

YAO, Q.; ZHANG, J.; WANG, K.; JING, L.; CHENG, X.; SHANG, C.; DING, J.; ZHANG, W.; SUN, H.; ZHOU, T. Broadband and massive Stokes shift luminescence in fully inorganic 2D-layered perovskite $CsPb_2Cl_5$: single crystal growth and self-trapped exciton emission. *Journal of Materials Chemistry C*, v. 9, n. 23, p. 7374–7383, 2021.

YASHIMA, M.; ALI, R. Structural phase transition and octahedral tilting in the calcium titanate perovskite $CaTiO_3$. *Solid State Ionics*, v. 180, n. 2–3, p. 120–126, 9 mar. 2009.

YIN, J.; MAITY, P.; BASTIANI, M. DE; DURSUN, I.; BAKR, O. M.; BRÉDAS, J. L.; MOHAMMED, O. F. Molecular behavior of zero-dimensional perovskites. *Science Advances*, v. 3, n. 12, p. 2–10, 2017.

YIN, J.; ZHANG, G.; TAO, X. A fractional crystallization technique towards pure mega-size $CsPb_2Br_5$ single crystal films. *CrystEngComm*, v. 21, n. 9, p. 1352–1357, 2019.

YIN, W.-J.; YANG, J.-H.; KANG, J.; YAN, Y.; WEI, S.-H. Halide perovskite materials for solar cells: a theoretical review. *Journal of Materials Chemistry A*, v. 3, n. 17, p. 8926–8942, 7 maio 2015.

YIN, Y.; LIU, Y.; CAO, G.; LV, Z.; ZONG, H.; CHENG, Y.; DONG, Q.; LIU, C.; LI, M.; ZHANG, B. Optical properties and mechanical induced phase transition of $CsPb_2Br_5$

and $CsPbBr_3$ nanocrystals. *Journal of Alloys and Compounds*, v. 947, p. 169439, jun. 2023.

YUAN, X.; JI, S.; SIENA, M. C. DE; FEI, L.; ZHAO, Z.; WANG, Y.; LI, H.; ZHAO, J.; GAMELIN, D. R. Photoluminescence Temperature Dependence, Dynamics, and Quantum Efficiencies in Mn2+-Doped $CsPbCl_3$ Perovskite Nanocrystals with Varied Dopant Concentration. *Chemistry of Materials*, v. 29, n. 18, p. 8003–8011, 2017.

ZHANG, B.; ZHANG, H.; LIN, J.; CHENG, X. A time-dependent density functional study on optical response in all-inorganic lead-halide perovskite nanostructures. *International Journal of Quantum Chemistry*, v. 120, n. 13, p. 1–11, 13 jul. 2020.

ZHANG, D.; EATON, S. W.; YU, Y.; DOU, L.; YANG, P. Solution-Phase Synthesis of Cesium Lead Halide Perovskite Nanowires. *Journal of the American Chemical Society*, v. 137, n. 29, p. 9230–9233, 29 jul. 2015.

ZHANG, H.; XU, Y.; SUN, Q.; DONG, J.; LU, Y.; ZHANG, B.; JIE, W. Lead free halide perovskite Cs_3Bi2I_9 bulk crystals grown by a low temperature solution method. *CrystEngComm*, v. 20, n. 34, p. 4935–4941, 2018.

ZHANG, J.; HODES, G.; JIN, Z.; LIU, S. (FRANK). All-Inorganic $CsPbX_3$ Perovskite Solar Cells: Progress and Prospects. *Angewandte Chemie*: International Edition, v. 58, n. 44, p. 15596–15618, 28 out. 2019.

ZHANG, L.; WANG, K.; ZOU, B. Bismuth Halide Perovskite-Like Materials: Current Opportunities and Challenges. *ChemSusChem*, v. 12, n. 8, p. 1612–1630, 23 abr. 2019.

ZHANG, L.; WANG, L.; WANG, K.; ZOU, B. Pressure-Induced Structural Evolution and Optical Properties of Metal-Halide Perovskite $CsPbCl_3$. *The Journal of Physical Chemistry C*, v. 122, n. 27, p. 15220–15225, 12 jul. 2018.

ZHANG, L.; ZENG, Q.; WANG, K. Pressure-Induced Structural and Optical Properties of Inorganic Halide Perovskite $CsPbBr_3$. *The Journal of Physical Chemistry Letters*, v. 8, n. 16, p. 3752–3758, 17 ago. 2017.

ZHANG, Q.; SHANG, Q.; SU, R.; DO, T. T. H.; XIONG, Q. Halide Perovskite Semiconductor Lasers: Materials, Cavity Design, and Low Threshold. *Nano Letters*, v. 21, n. 5, p. 1903–1914, 10 mar. 2021.

ZHANG, Q.; YIN, Y. All-Inorganic Metal Halide Perovskite Nanocrystals: Opportunities and Challenges. *ACS Central Science*, v. 4, n. 6, p. 668–679, 2018.

ZHANG, T.; CHEN, ZHIHUI; SHI, Y.; XU, Q. H. The photoluminescence mechanism of $CsPb_2Nr_5$ microplates revealed by spatially resolved single particle spectroscopy. *Nanoscale*, v. 11, n. 7, p. 3216–3221, 2019.

ZHANG, W.; EPERON, G. E.; SNAITH, H. J. Metal halide perovskites for energy applications. *Nature Energy*, v. 1, n. 6, p. 16048, 9 maio 2016.

ZHANG, Y.; LIU, X.; SUN, H.; ZHANG, J.; GAO, X.; YANG, C.; LI, Q.; JIANG, H.; WANG, J.; XU, D. Strong Self-Trapped Exciton Emissions in Two-Dimensional Na-In Halide Perovskites Triggered by Antimony Doping. *Angewandte Chemie:* International Edition, v. 60, n. 14, p. 7587–7592, 29 mar. 2021.

ZHANG, Z.; ZHU, Y.; WANG, W.; ZHENG, W.; LIN, R.; HUANG, F. Growth, characterization and optoelectronic applications of pure-phase large-area $CsPb_2Br_5$ flake single crystals. *Journal of Materials Chemistry C*, v. 6, n. 3, p. 446–451, 2018.

ZHAO, Y.; DUAN, J.; YUAN, H.; WANG, Y.; YANG, X.; HE, B.; TANG, Q. Using SnO_2 QDs and $CsMBr_3$ (M = Sn, Bi, Cu) QDs as Charge-Transporting Materials for 10.6%-Efficiency All-Inorganic $CsPbBr_3$ Perovskite Solar Cells with an Ultrahigh Open-Circuit Voltage of 1.610 V. *Solar RRL*, v. 3, n. 3, p. 1800284, 1 mar. 2019.

ZHOU, C.; LIN, H.; HE, Q.; XU, L.; WORKU, M.; CHAABAN, M.; LEE, S.; SHI, X.; DU, M.-H.; MA, B. Low dimensional metal halide perovskites and hybrids. *Materials Science and Engineering:* Reports, v. 137, p. 38–65, 1 jul. 2019.

ZHOU, J.; HUANG, J. Photodetectors Based on Organic-Inorganic Hybrid Lead Halide Perovskites. *Advanced Science*, v. 5, n. 1, p. 1700256, 1 jan. 2018.

ZHOU, L.; LIAO, J.; QIN, Y.; WANG, X.; WEI, J.; LI, M.; KUANG, D.; HE, R. Activation of Self-Trapped Emission in Stable Bismuth-Halide Perovskite by Suppressing Strong Exciton–Phonon Coupling. *Advanced Functional Materials*, v. 31, n. 31, p. 2102654, 10 ago. 2021.

ZHU, P.; ZHU, H.; ADHIKARI, G. C.; THAPA, S. Spectral optimization of white light from hybrid metal halide perovskites. *OSA Continuum*, v. 2, n. 6, p. 1880, 15 jun. 2019.

ZHU, P.; ZHU, J. Low-dimensional metal halide perovskites and related optoelectronic applications. *InfoMat*, v. 2, n. 2, p. 341–378, 6 mar. 2020.